Title
Development of experimental techniques for the execution and in situ monitoring of simultaneous irradiation-corrosion experiments

Author
Schmidt, Franziska

Publication Date
2022

Peer reviewed|Thesis/dissertation

Development of experimental techniques for the execution and in situ monitoring of simultaneous irradiation-corrosion experiments

By

Franziska Schmidt

A dissertation submitted in partial satisfaction of the

requirements for the degree of

Doctor of Philosophy

in

Engineering – Nuclear Engineering

in the

Graduate Division

of the

University of California, Berkeley

Committee in charge:

Professor Peter Hosemann, Chair
Professor Per Peterson
Professor Mary Scott

Fall 2022

Development of experimental techniques for the execution and in situ monitoring of simultaneous irradiation-corrosion experiments

Abstract

Development of experimental techniques for the execution and in situ monitoring of simultaneous irradiation-corrosion experiments

by

Franziska Schmidt

Doctor of Philosophy in Nuclear Engineering

University of California, Berkeley

Professor Peter Hosemann, Chair

The next generation of nuclear fission reactors is under development to lead to reactor designs that are more sustainable, more economical, safer, and more proliferation-resistant than current light water reactors (LWRs) (1). Each Gen-IV reactor design involves a unique heat transfer medium, which creates a host of novel nuclear materials challenges. One of these new reactor coolants is heavy liquid metal (HLM), i.e., pure Pb or Pb-Bi eutectic (LBE). HLM reactors are designed to operate in the fast neutron spectrum to reduce nuclear waste production compared to current LWRs. LBE specifically is an excellent HLM coolant candidate because of its low vapor pressure, low melting point (123.5 °C), and high boiling point (1670 °C), which allows for greater thermal efficiency in electricity production. However, steels in contact with LBE must withstand not only its corrosive nature but also the simultaneous exposure to radiation fields, high temperatures, and vibration.

The interaction of two of these environmental extremes – LBE corrosion and radiation damage – is investigated in a newly developed simultaneous proton irradiation-corrosion setup. It consists of a corrosion chamber, in which sample disks (50 µm thick or less) can be exposed to corrosion and radiation simultaneously. A defocused proton beam is used to create point defects in the sample up to the metal-coolant interface. Pure Fe serves as a model system instead of more complex structural materials, such as steels, in order to get a better understanding of the interaction between radiation damage in the metal / the metal oxide and its influence on corrosion.

The results show that the presence of the beam accelerates the degradation of the Fe-oxide layer formed on the sample, which allows LBE to penetrate sooner than in the absence of the beam. This penetration leads to the creation of pits underneath the oxide and a switch from the desirable oxide-forming regime to a dissolution-based corrosion mode, where the LBE dissolves the formerly metal-facing side of the oxide as well as the Fe sample itself. The resulting thinning of the samples was observed continuously during each irradiation-corrosion experiment with in-situ particle-induced x-ray emission spectroscopy (PIXE). PIXE also provides evidence for the accelerated corrosion in the beam spot being interrupted during extended periods of absence of the proton beam. This shows that corrosion is primarily accelerated in the simultaneous presence of radiation and corrosion.

Ex situ microscopy analysis provides evidence that the thinning of the samples is strongest in the beam spot, but that surrounding areas are also affected. Thermocouple measurements during the experiments show that there is a temperature difference of 10-20 °C across the corrosion

chamber when the beam is present. More work is needed to fully understand whether this temperature difference or the diffusion of radiation-induced defects are the primary cause of accelerated corrosion in and near the beam spot.

To accelerate the study of structural materials even further and to increase the statistical significance of the results, a reduced-volume irradiation-corrosion setup was developed. In these experiments, several smaller irradiation-corrosion "chambers" with thin-film samples (1 μm or less) are mounted on a heater stage and exposed to a rastered proton beam to ensure identical irradiation-corrosion conditions. Preliminary results show that radiation accelerates the dissolution of Fe thin-films in LBE even in the absence of beam heating and at very low displacements per atom.

For Science!

Table of contents

List of figures

List of tables

List of acronyms

ADS	**A**ccelerator-**D**riven **S**ystem
AISI	**A**merican **I**ron and **S**teel **I**nstitute
AL	**A**ction **L**imit
bcc	**b**ody-**c**entered **c**ubic
BPM	**B**eam **P**osition **M**onitor
BREST	fast reactor with inherent safety, transliterated
BREST-OD	fast reactor with inherent safety - experimental demonstration, transliterated
BWR	**B**oiling **W**ater **R**eactor
CF	**C**on**F**lat
CINT	**C**enter for **I**ntegrated **N**ano**T**echnologies
CLEAR	**C**hina **LEA**d-based **R**esearch reactor
DBTT	**D**uctile-to-**B**rittle **T**ransition **T**emperature
DEMETRA	**DE**velopment and assessment of structural materials and heavy liquid **ME**tal technologies for **TRA**nsmutation systems
DFR	**D**ual-**F**luid **R**eactor
dpa	**d**isplacement **p**er **a**tom
EAP80-XADS	**E**nergy-**A**mplifier **P**roject-e**X**perimental **A**ccelerator-**D**riven **S**ystem
EDS	**E**nergy **D**ispersive x-ray **S**pectroscopy
EFIT	**E**uropean **F**acility for **I**ndustrial **T**ransmutation of minor actinides
ELFR	**E**uropean **L**ead **F**ast **R**eactor
fcc	**f**ace-**c**entered **c**ubic
FIB	**F**ocused **I**on **B**eam
F/M	**F**erritic/**M**artensitic
FP	**F**ission **P**roduct
FPGA	**F**ield-**P**rogrammable **G**ate **A**rray
FWHM	**F**ull **W**idth at **H**alf **M**aximum
GB	**G**rain **B**oundary
GETMAT	**GE**neration IV and **T**ransmutation **MAT**erial
HLM	**H**eavy **L**iquid **M**etal
HPM	**H**yperion **P**ower **M**odule
HYPER	**HY**brid **P**ower **E**xtraction **R**eactor

IASCC	**I**rradiation-**A**ssisted **S**tress **C**orrosion **C**racking
IBML	**I**on **B**eam **M**aterials **L**aboratory
ICE	**I**rradiation-**C**orrosion **E**xperiment
JAEA	**J**apanese **A**tomic **E**nergy **A**gency
LANL	**L**os **A**lamos **N**ational **L**aboratory
LANSCE	**L**os **A**lamos **N**eutron **S**cience **CE**nter
LBE	**L**ead-**B**ismuth **E**utectic
LFR	**L**ead **F**ast **R**eactor
LFR-AS	**L**ead **F**ast **R**eactor-**A**mphora-**S**haped
LiSoR	**Li**quid metal – **So**lid metal **R**eaction
LM	**L**iquid **M**etal
LMC	**L**iquid **M**etal **C**orrosion
LME	**L**iquid **M**etal **E**mbrittlement
LWR	**L**ight **W**ater **R**eactor
MEGAPIE	**MEGA**watt **PI**lot **E**xperiment
MSRE	**M**olten **S**alt **R**eactor **E**xperiment
MST	**M**aterials **S**cience and **T**echnology division
MYRRHA	**M**ultipurpose h**Y**brid **R**esearch **R**eactor for **H**igh-tech **A**pplications
NEC	**N**ational **E**lectrostatics **C**orporation
NPT	**N**ational **P**ipe **T**hread
ODS	**O**xide-**D**ispersion **S**trengthened
OSHA	**O**ccupational **S**afety and **H**ealth **A**dministration
PALS	**P**ositron **A**nnihilation **L**ifetime **S**pectroscopy
PASCAR	**P**roliferation-resistant **A**ccident-tolerant **S**elf-supported **C**apsular and **A**ssured **R**eactor
PEL	**P**ermissible **E**xposure **L**imit
PFIB	**P**lasma **F**ocused **I**on **B**eam
PIGE	**P**article-**I**nduced **γ** **E**mission spectroscopy
PIXE	**P**article-**I**nduced **X**-ray **E**mission spectroscopy
PUREX	**P**lutonium **U**ranium **R**eduction **EX**traction
PVD	**P**hysical **V**apor **D**eposition
PWR	**P**ressurized **W**ater **R**eactor
RED	**R**adiation-**E**nhanced **D**iffusion

RIS	**R**adiation-**I**nduced **S**egregation
RT	**R**oom **T**emperature
SCC	**S**tress **C**orrosion **C**racking
SDD	**S**ilicon-**D**rift **D**etector
SEALER	**S**w**E**dish **A**dvanced **LE**ad **R**eactor
SEM	**S**canning **E**lectron **M**icroscope/y
SFR	**S**odium **F**ast **R**eactor
SNICS	**S**ource of **N**egative **I**ons by **C**esium **S**puttering
SSTAR	**S**mall **S**ecure **T**ransportable **A**utonomous **R**eactor
SVBR	lead-bismuth fast reactor, transliterated
STEM	**S**canning **T**ransmission **E**lectron **M**icroscope/y
TC	**T**hermo**C**ouple
TEM	**T**ransmission **E**lectron **M**icroscopy
TP	**T**ransmutation **P**roduct
UCB	**U**niversity of **C**alifornia, **B**erkeley
URANUS	**U**biquitous, **R**obust, **A**ccident-forgiving, **N**onproliferating and **U**ltra-lasting **S**ustainer
XADS	e**X**perimental **A**ccelerator-**D**riven **S**ystem
XT-ADS	e**X**perimental **T**ransmuter-**A**ccelerator-**D**riven **S**ystem

Acknowledgments

None of this would be possible without my advisor, Peter Hosemann. Thank you for taking a chance on me and for giving me the opportunity to work on this awesome project, present my work, and make connections for the future. I would also like to thank my committee members, Per Peterson and Mary Scott, for their guidance in preparing this manuscript.

For the past three years, I have had the opportunity to conduct research at Los Alamos National Laboratory (LANL). I would like to express gratitude to my mentors, Yong Wang, for introducing me to hands-on work with accelerators and risking not one but two of them for my experiments, and Blas Uberuaga, for giving me the opportunity to work with him and other experts on reviewing the literature and supporting me in my endeavors at LANL.

I would also like to thank my family – especially my parents, my brother, and my grandparents – for always supporting me from afar. In line with family tradition, I chose a somewhat nomadic life that would not have been possible without you. The same goes for my friends from the before-times at home and not so close to home. Thanks for sticking with me regardless of which continent I am on.

In Berkeley, a number of people have provided support over the past few years, moral and otherwise. Everyone in the Nuclear Materials group – AJ Gubser, Evan Still, Hi Vo, Jeff Bickel, Jeff Graham, Joey Kabel, Mehdi Balooch, Rasheed Auguste, Sarah Stevenson, and others –, thanks for good discussions, fun times in the office, and for making pre-Covid times great.

Outside of the group, I would like to thank Amanda Lewis, Eric Matthews, Joanna Szornel, Kristina Cheng, Mitch Negus, and countable others for making life in Berkeley fun. Special thanks to Justin Randolph Ellin for proof-reading this dissertation and motivating me throughout the program.

In Los Alamos, I would like to thank several colleagues and friends as well: Matt Chancey and Sim Kim for making the basement an enjoyable place to work; Marshall Maez for great advice on how to turn crazy ideas into real parts; Ben Derby, David Frazer, Hi Vo, Laura McGuinness, Mario Ortega, Carolin Zitzmann, Sam Frank, and many others for fun times outside of work, be it in the air, on the trail, or at the bar; and finally Scott and Katie Parker-Behrens, Kai Newhouse, and Li Jiaru for creating a great living atmosphere and for getting jacked together.

This work was supported as part of FUTURE (Fundamental Understanding of Transport Under Reactor Extremes), an Energy Frontier Research Center funded by the U.S. Department of Energy, Office of Science, Basic Energy Sciences.

This work was performed, in part, at the Center for Integrated Nanotechnologies, an Office of Science User Facility operated for the U.S. Department of Energy (DOE) Office of Science. Los Alamos National Laboratory, an affirmative action equal opportunity employer, is managed by Triad National Security, LLC for the U.S. Department of Energy's NNSA, under contract 89233218CNA000001.

1. Motivation

1.1. Gen-IV reactor development

In 2021, 437 nuclear power reactors (2) provided approximately 10% of the world's global electricity supply (3). Two thirds of the operational nuclear reactors, which also correspond to two thirds of the global net electrical capacity from nuclear power, are currently more than 30 years old (see Figure 1). They will have to be replaced over the coming decades to at least maintain nuclear energy production, if not increase it. 56 units are currently under construction, the majority of which are pressurized water reactors (PWRs), which make up the majority of the fleet of currently operating reactors (3). While water-cooled reactors are undoubtedly the workhorse of nuclear electricity production, several areas warrant further improvement, namely rare event safety management, proliferation resistance, fuel cycle enhancements, radioactive waste management, thermal efficiency, and economic competitiveness (4). In addition, current reactors predominantly use the fissile ^{235}U as their fuel source, which only accounts for 0.7% of the natural U resources on Earth and is expected to be consumed by the end of the century (5). Of the six designs that have been selected by the Generation IV International Forum, an international collaboration for the development of the next generation of nuclear reactors, only one is water-based (6).

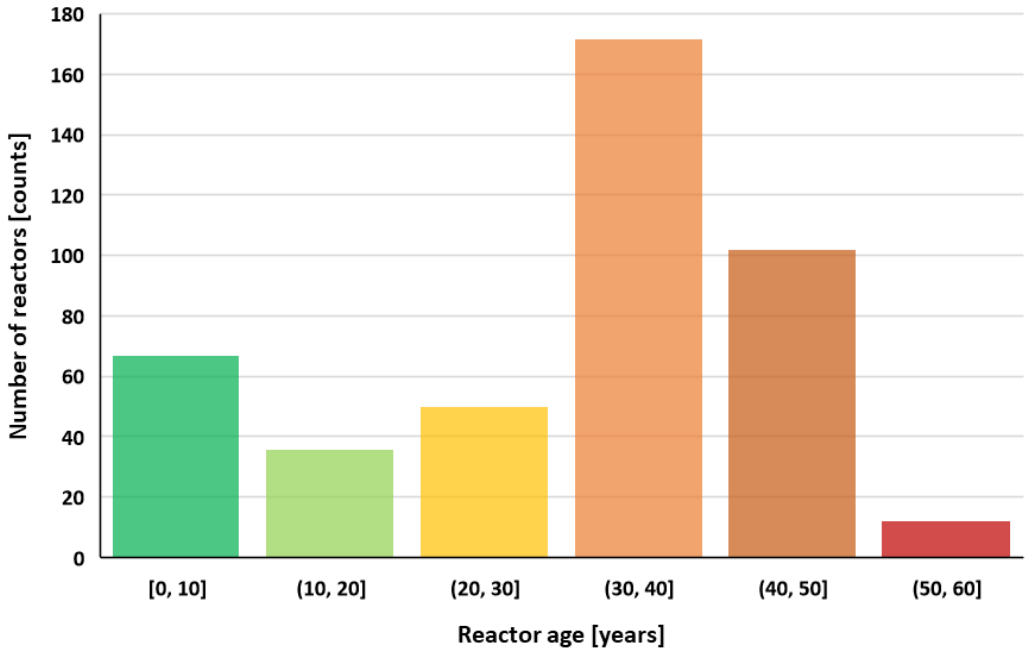

Figure 1 – Number of reactors worldwide and their age based on (7).

The new coolants include liquid metals (LMs: Na and heavy liquid metals (HLMs)), molten salts (chlorides and fluorides), supercritical water, and He gas. These coolants are supposed to enable reactor designs with more inherent and passive safety characteristics (1). Many of the new

reactor designs can operate in the fast neutron spectrum (> 0.1 MeV*) because their coolants moderate neutrons significantly less than water. Fast spectrum operation requires the use of materials that can withstand the exposure to larger quantities of fast neutrons compared to a thermal spectrum. On the plus side, this enables better fuel utilization because ^{239}Pu can be bred from ^{238}U (99.3% natural abundance) (5, 8), which drastically increases the efficiency of U sources.

Another benefit of a faster neutron spectrum is the ability to transmute long-lived isotopes produced in nuclear reactors into isotopes with shorter half-lives (5). Even if U and Pu isotopes are chemically separated from spent nuclear fuel, e.g., during PUREX (Pu U reduction extraction) reprocessing (9), and reused as fuel, a large number of radioactive transmutation products (TPs) and fission products (FPs) remains. Among the TPs, the actinides Am (up to several 10^5 years), Np (beyond 10^5 years), and Cm (after 10^4 years) are the main contributors to waste radiotoxicity (10). Of the long-lived FPs, ^{99}Tc, ^{126}Sn, and ^{79}Se contribute to the total radiotoxicity until 10^5 years and ^{129}I, ^{93}Zr, and ^{135}Cs contribute beyond this time frame (10). The potential for complete burnup of all TPs is highest for reactors operating in the fast neutron spectrum (11) because of the larger fission cross sections for fast neutrons compared to thermal neutrons.

The transmutation of long-lived FPs is more complex. For example, the two isotopes that dominate mid-term radiotoxicity (between 10 and ~10^3 years) – ^{137}Cs and ^{90}Sr – are generally considered non-transmutable in nuclear reactor environments because of their prohibitively small neutron capture cross sections, even for thermal neutrons (12). The transmutation of these and other FPs to shorter-lived radioactive isotopes may be possible with charged particle irradiation (see, e.g., (13)) or intense accelerator driven neutron spallation sources (14) whose high flux compensates for the small neutron capture cross sections. The establishment of such facilities is expensive but would substantially lower the radioactivity of spent nuclear fuel. Therefore, fast reactors that transmute their own waste with a closed fuel cycle and/or dedicated transmutation facilities, such as accelerator driven systems (ADSs), are key to solving the problem of long-term radiotoxicity resulting from current open fuel cycles, which hampers the development and spread of nuclear reactor technology.

LM-cooled reactors are not new, even though they are considered part of the "new" generation of nuclear reactors. 400 reactor-years of operation from 22 fast test reactors have been accumulated around the world (15, 16). This corresponds to ~2% of the total number of reactor-years of operation for all nuclear power reactors in existence (19,416 reactor-years from 438 nuclear reactors (17)). HLMs, such as Pb and Pb-Bi eutectic (LBE, 55.5 wt% Bi, 44.5 wt% Pb) are prominent candidates for the primary coolant loop of large-scale fast reactors (lead fast reactor (LFR)) and spallation targets for ADSs (18–20). Due to their high atomic number, Pb and LBE exhibit limited neutron moderation, unlike Na, which moderates neutrons to a greater extent. They also have small neutron absorption cross sections (21), which leads to fast neutron spectra, and good heat transfer capabilities. Both of these HLMs have high boiling points (Pb: 1737 °C, LBE: 1670 °C) and low vapor pressure (see Figure 46 in Appendix 8.1), which allows operation at ambient pressure, and do not react strongly with air or water (21). The latter is an inherent safety characteristic that prevents hazardous conditions that may be encountered in liquid Na-cooled fast reactors (SFRs) when Na comes into contact with air during an accident.

In addition to the historical LBE-cooled Soviet submarine reactors (22) there are numerous new Pb/LBE-cooled reactor designs, such as the SVBR (lead-bismuth fast reactor, transliterated),

* 0.1 MeV is used as the definition of a "fast" neutron in the fast reactor community, rather than the typical 1 MeV used in the context of thermal reactors, to reflect the softer mean energies of metal-fueled (0.8 MeV) and oxide-fueled (0.45-0.55 MeV) fast reactors (see, e.g., (45)).

SSTAR (Small Secure Transportable Autonomous Reactor), and PASCAR (Proliferation-resistant Accident-tolerant Self-supported Capsular and Assured Reactor) (23–25), as well as ADS designs, e.g., MYRRHA (Multipurpose hYbrid Research Reactor for High-tech Applications) (5). More information on some of the LFR designs can be found in Section 3.1.1, while ADSs will be covered in Section 3.1.2. The main takeaway here is that HLM-cooled systems are an active field of research with a not insignificant history that has demonstrated their successful operation.

The materials exposed to these environments face many novel challenges that involve intense radiation fields, high temperatures, temperature gradients, and mechanical stresses. Each of these factors – both separately and together – can contribute to damage of structural materials. Corrosion is only one of many degradation processes resulting from this list, but it is an important factor for the longevity of critical components, such as cladding tubes and the reactor vessel. The progression of corrosion needs to be controlled regardless of its synergies with other factors, such as irradiation, to ensure safe operation of a nuclear energy system.

1.2. Corrosion challenges in nuclear environments

In LWRs, the main corrosion mechanisms of concern for stainless steels are pitting corrosion, intergranular corrosion, and stress-corrosion cracking (SCC) in the form of intergranular SCC and irradiation-assisted SCC (IASCC). Corrosion often occurs in tight spaces where the local water chemistry becomes more aggressive compared to the bulk. New Gen-IV reactors will expose materials to new coolants and, in some cases, higher temperatures for improved energy conversion efficiency. This inevitably introduces new mechanical and corrosion challenges for reactor materials. A good understanding of the corrosive properties of the coolant is required to select suitable structural materials.

Radiation is known to affect corrosion processes in materials, typically in a negative way. This is relevant in those parts of a reactor, where significant radiation fields and a corrosive coolant are present simultaneously, e.g., in and near the reactor core. Therefore, radiation-induced damage and corrosion of materials must be understood both independently and synergistically. While the use of ion beam analysis for the study of neutron-induced damage has greatly improved our understanding of radiation-induced processes and accelerated the discovery and testing of new materials, setups featuring simultaneous irradiation and corrosion of materials are still relatively scarce (26).

This dissertation will discuss the effects of simultaneous irradiation and corrosion on pure metals, specifically the response of pure Fe to an oxide-forming LBE environment under simultaneous proton irradiation. In the following chapters, an experimental setup for the simultaneous exposure of metals to HLM corrosion and proton irradiation will be described and a new method to monitor the corrosion process in situ with particle-induced x-ray emission spectroscopy (PIXE) will be introduced. For the first time, the irradiation-corrosion behavior of pure Fe in LBE has been monitored continuously for experiments lasting tens of hours. The predictions of the sample's thickness produced by PIXE were validated with microscopy, making time-resolved PIXE a useful technique for future irradiation-corrosion experiments.

2. Research objectives

With the advent of new nuclear reactor coolant candidates, the link between the various extremes that materials are exposed to, such as corrosion at high temperatures, radiation fields, and stresses, needs to be reestablished for new coolant-materials pairs. Therefore, a substantial amount of experimental data is needed to deepen the theoretical understanding of the synergistic effects of these extreme environments and to enable accelerated materials discovery and performance prediction for Gen-IV nuclear reactors. The goal of this work is to establish experimental capabilities for the study of materials simultaneously exposed to corrosion and irradiation, and to contribute to the understanding of the interactions between these two extreme environments.

2.1. Hypothesis

Even though there are a few examples to the contrary (see Section 3.5), radiation is generally thought to exacerbate corrosion. High energy ionizing radiation induces large numbers of point defects in solids. Although many of these defects recombine athermally as the collision cascade unfolds (27), many of them survive and contribute to the formation of higher-dimensional defect structures that can ultimately alter materials properties. Ionizing radiation also disrupts the electronic structure of oxide lattices in oxide-forming corrosion environments, which mobilizes electrons and increases the reactivity of the species in the oxide. The kinetics of corrosion processes are strongly dependent on the diffusion of participating species and their reactivity. Therefore, the introduction of radiation-induced nonequilibrium point defects likely alters the diffusion kinetics in solids and their corrosion layers. Corrosion experiments with pre-irradiated samples only capture effects related to those defects that survive the cascade. The hypothesis presented here is 1) that the corrosion of model alloys, such as pure Fe, in HLMs is accelerated while under simultaneous irradiation by a proton beam, and 2) that this acceleration is greater under simultaneous irradiation-corrosion conditions than when irradiation and corrosion are decoupled due to the large number of short-lived radiation-induced defects.

2.2. Dissertation outline

This dissertation describes the development of a simultaneous irradiation-corrosion experiment. The setup is intended to be compatible with HLMs, but also with molten salts. Thin samples (50 μm or less) can be exposed to the heated corrosive medium and a high-energy proton beam ($\leq$ 4 MeV) simultaneously. Furthermore, the aim is to establish a capability for in-situ corrosion rate monitoring to prevent premature experiment failure and to obtain quantitative corrosion rate information. This feature is added in the form of PIXE, which provides a powerful continuous corrosion monitoring tool by measuring the x-ray signal in the beam spot over the course of the experiment.

Chapter 3 provides background on the nuclear environments where HLMs may be used, specifically LFRs and ADSs (Section 3.1). Section 3.2 describes the degradation of metals, primarily steels, in contact with LBE and strategies for corrosion mitigation. Then, an overview of irradiation effects in nuclear environments is given in Section 3.3. Section 3.4 discusses the materials candidates for HLM environments. Finally, an introduction to known irradiation-

corrosion processes in nuclear environments in general is given in Section 3.5 and methods for their experimental study are briefly discussed in Section 3.6.

Chapter 4 describes the experimental components of this project. Section 4.1 shows the evaluation of a sample produced by the Irradiation-Corrosion Experiment (ICE) II, the predecessor of the current iteration, ICE III, which was developed during this work (see Section 4.2). Section 4.3 describes the PIXE setup and some in-situ corrosion monitoring alternatives that could be selected in addition or instead. Experimental results using ICE III with PIXE are shown in Section 4.4. Section 4.5 describes extensions of the ICE III setup, such as the slightly modified chamber for rare molten salts and a high-throughput approach for thin-film studies exposed to LBE and lower energy protons (a few hundred keV).

In Chapter 5, the implications of the experimental results are discussed. First, the conditions in the regular ICE III chamber and the resulting corrosion behavior are compared to the literature in Section 5.1. An attempt at a mechanistic explanation for the impact of radiation damage and beam heating is made in Section 5.2. Section 5.3 provides some discussion on the different ICE III experiments and their features.

Finally, Chapter 6 provides a summary of the presented work and outlines future work.

3. Background

3.1. Heavy liquid metals (HLMs) in nuclear environments

3.1.1. Lead fast reactors (LFRs)

LFRs use either pure Pb or LBE as the primary loop coolant. Compared to SFRs, international operating experience is much more limited, although the Russian nuclear submarine program alone has 80 years of operational experience from 12 reactors (15), such as the OK-550 and the BM-40A submarine reactors (Alfa class / Project 705 Lira), which were cooled with LBE (28). The new Pb-cooled BREST-OD-300 reactor (fast reactor with inherent safety – experimental demonstration reactor, transliterated) and the BREST-1200 reactor are based on these designs (15). Outside of Russia, there are several efforts to develop Pb- and LBE-cooled reactors as well, both with smaller and larger power outputs (see Table 1).

The main contributors to the international experience with LM-cooled reactors, however, are several SFRs (29). In SFRs, materials-Na interactions are limited, as long as the coolant is kept relatively free of impurities, such as As, Sb, and Bi, which are responsible for liquid metal embrittlement (LME) (15), as well as O and C, which degrade mechanical and corrosion properties (15, 30). However, Na has strong exothermic reactions with water or air, which has led to Na fires in SFRs (see, e.g., (31, 32)). By contrast, HLMs are less reactive when in contact with water or air. However, exposure to significant amounts of O may cause the formation of solid PbO, which can lead to a drastic decrease of heat removal from the core (see, e.g., (22)). An inert cover gas, typically Ar, is used to prevent PbO formation, but also to accommodate the thermal expansion of the liquid.

HLMs do not significantly moderate neutrons and can therefore maintain a fast spectrum, have reasonably low melting points (Pb: 327.5 °C, LBE: 123.5 °C (see Table 2 for comparison of other properties)), low vapor pressure, high Z for good γ-shielding, and small neutron absorption cross sections (6, 21, 33, 34). However, HLMs are known to interact with structural alloys, primarily via LME and liquid metal corrosion (LMC). In addition, their high density compared to other Gen-IV coolants leads to high hydrostatic pressures and positive buoyancy of core internals. Consequently, fuel assemblies must be held submerged in the HLM and passive safety mechanisms for reactivity control must be designed to insert control rods from the bottom of the core assembly to make use of the positive buoyancy.

The addition of Bi to Pb has several advantages and disadvantages. The main advantage is the lower melting point, which reduces the risk of solidification of the coolant due to a loss of power, which could render the reactor inoperable. However, many Pb-cooled designs are pool-type reactors, in which the large amount of Pb does not easily freeze due to its high volumetric heat capacity. Another advantage is that the volume change of LBE upon melting is close to zero (21), which is an important property in case of coolant solidification. Disadvantages include the high price of Bi as well as the production of ^{210}Po under neutron irradiation. ^{210}Po is a parasitic neutron absorber, and also an α-emitter that has the potential to escape the primary coolant loop due to its high volatility (35).

Fast reactors require high burnup of the enriched fuel to make them economically feasible, which is less of a concern in non-commercial scenarios. However, high burnup requires radiation-tolerant core structural materials, specifically for cladding tubes and wrapper tubes, that can withstand ≥ 20 at% burnup without failure. This is approximately twice the currently achievable burnup for austenitic stainless steels (15). Note that cladding performance is expressed in terms of

Table 1 – List of Pb- and LBE-cooled fast reactor designs in alphabetical order.

Acronym	Country	MWe	Coolant	Full name	Refs.
BREST-OD-300	Russia	300	Pb	fast reactor with inherent safety - experimental demonstration, transliterated	(36)
BREST-1200	Russia	1200	Pb	fast reactor with inherent safety, transliterated	(37)
CLEAR-1	China	10 (MW_{th})	LBE	China LEAd-based Research reactor	(36, 37)
DFR300*	Germany	300	Pb	Dual-Fluid Reactor	(38)
DFR1500*	Germany	1500	Pb	Dual-Fluid Reactor	(38)
ELFR	European Union	600	Pb	European LFR	(36, 37, 39)
Hydromine LFR-AS-200	United Kingdom / Italy	200	Pb	LFR-Amphora-Shaped	(36)
HPM	United States	25	LBE	Hyperion Power Module	(40)
SEALER	Sweden	55	Pb	SwEdish Advanced LEad Reactor	(36, 41)
SSTAR	United States	10-100	Pb	Small Secure Transportable Autonomous Reactor	(36)
SVBR-100	Russia	100	LBE	lead-bismuth fast reactor, transliterated	(23)
URANUS-40	South Korea	40	LBE	Ubiquitous, Robust, Accident-forgiving, Nonproliferating and Ultra-lasting Sustainer	(42, 43)
Westinghouse LFR	United States	450	Pb	-	(37)

Table 2 – Comparison of Pb and LBE properties based on (21) and Table 2 in (44).

Property	Pb	LBE
T_{melt} [°C]	327.5	123.5
T_{boil} [°C]	1737	1670
Density @RT [g/cm^3]	11.35	10.5
Density @450 °C [g/cm^3]	10.5	10.2
Relative moderation (density-corrected)	1	0.82
Neutron absorption cross section (1 MeV) [mb]	6.001	1.492
Averaged neutron scattering cross section [b]	6.4	6.9
Volume change upon solidification [%]	3.32	0
Thermal conductivity @450 °C [W/m-K]	17	13.5

* These designs are not traditional LFR designs with solid fuel like those described in this section but rather liquid fuel designs with fuel dissolved in molten chloride.

burnup rather than dpa (displacements per atom, see Section 3.3) here to include other effects, such as fission gas release and fuel-cladding interactions, that may contribute to cladding failure in addition to the radiation dose. While other factors, such as FP accumulation and fuel restructuring also play a role in the lifetime of a fuel assembly, the most important factor is the potential failure of the cladding, which would result in the release of fuel and FPs into the coolant (15).

The use of fast neutrons ($\geq$ 0.1 MeV neutron energy) allows for the breeding and burning of fuel, which allows for the implementation of a closed fuel cycle in many LFR designs. To maintain a chain reaction, the fuel must have a high concentration of isotopes with high fast neutron fission cross sections, such as ^{235}U or ^{239}Pu. The overall neutron spectrum varies depending on the fuel type used (metal (0.8 MeV) or ceramic (0.45-0.55 MeV) (45), in which the low-Z non-metallic species increase neutron moderation), the coolant, and the presence of other neutron-moderating species. There are also local variations due to the relative amounts of fuel, coolant, and structural material as well as due to the position of a component in the reactor. The buildup of FPs and TPs may also modulate the neutron spectrum over time.

The operating temperature window is theoretically governed by the melting point of the coolant as the lower bound and the boiling point or the vapor pressure of the HLM as the higher bound although the latter is generally relatively low, even at high temperatures. In practice, however, a buffer of at least 100 °C above the melting point is necessary to avoid plugging due to local coolant solidification. The upper limit is lower than theoretically achievable because the mechanical properties of currently available structural materials prohibit operation at extremely high temperatures. This limits LFR operation to a window between ~300 to 700 °C (15) for LBE and ~400 to 700 °C for pure Pb.

3.1.2. Accelerator-driven systems (ADSs)

Due to its good spallation neutron yield, LBE is also considered for ADSs and liquid spallation neutron sources (46). ADSs are intended to lower the high-level nuclear waste burden produced by current nuclear reactors by transmuting select isotopes while also producing electricity. They consist of a high-energy proton accelerator (hundreds of MV) that produces neutrons in a heavy metal spallation target and a subcritical core whose reactivity is controlled by spallation neutrons. Since the core is subcritical, a loss of power to the facility that shuts down the accelerator also shuts down the reactor, which is an inherent safety feature. (46) provides a detailed overview of the technology and the various international efforts to develop these systems (see Table 3).

Most of the designs listed in Table 3 use LBE as their coolant, although some also consider Na or He as alternatives. Therefore, the materials in the spallation target and the subcritical core are exposed to HLMs. The most significant irradiation-corrosion interactions will occur in the proton beam window unless the design is windowless (see, e.g., MYRRHA and XT-ADS). In ADSs, lower operating temperatures are possible compared to LFRs, which makes corrosion less significant. However, this may be unnecessary as the life-limiting factor for an ADS is LME, especially of the beam window if present, rather than LMC (47). In addition, lower temperatures do not fully eliminate the production of corrosion products and have no impact on spallation products and TPs, so some buildup of impurities in the coolant will occur regardless.

Table 3 – List of ADS projects in alphabetical order based on (46).

Acronym	Country	MWth	E(H^+) [MeV]	Full name	Add'l. refs.
EAP80-XADS	Italy	80	600	Energy-Amplifier Project-eXperimental ADS	(48)
EFIT	European Union	~400	800	European Facility for Industrial Transmutation of minor actinides	
Gas-cooled XADS	France	80	600	-	
HYPER	South Korea	1000	1000	HYbrid Power Extraction Reactor	
JAEA Experimental ADS	Japan		1500	Japanese Atomic Energy Agency Experimental ADS	
JAEA Industrial scale ADS	Japan	800	1500	-	
MYRRHA	Belgium	50	350	Multi-purpose hYbrid Research Reactor for High-tech Applications	(49)
XT-ADS	European Union	50-100	600	eXperimental Transmuter-ADS	(49)

3.2. Degradation of steels in contact with LBE

The compatibility of materials with HLMs is one of the key factors to consider for LFRs (23, 50). Several degradation mechanisms are active when metals are exposed to a HLM environment, namely LME, LMC, as well as erosion corrosion and fretting when flow is present. (15) provides an excellent overview of these processes, and even more detail about each of these topics can be found in (51). The two primary candidate classes for LBE-facing components are ferritic/martensitic (F/M) steels and austenitic stainless steels, which will be discussed in more detail in Section 3.4, but will also be mentioned in this and the following sections where appropriate.

Brittle fracture due to LME is of concern for practically all structural materials in contact with the coolant (52). In LME, the wetting of the material's surface causes the adsorption of Pb and Bi atoms to the tips of cracks upon nucleation under stress. As a result, crack propagation is greatly accelerated, which leads to significant embrittlement, faster fatigue, and degraded creep properties (53). The primary requirements for this process are a wetted metal surface under tensile stress and plastic deformation (15). Several factors can increase LME occurrence and severity, including, but not limited to, the temperature of the system, the chemical composition and microstructure of the steel, HLM chemistry (specifically, dissolved O), the strain rate applied to the component, and any form of pre-exposure, e.g., to radiation, the metal has experienced. LME can become a life-limiting factor for structural components, in particular in conjunction with neutron irradiation, which may lower the fracture toughness of metals via radiation hardening (54) or by inducing precipitate formation and/or a coarsening of existing precipitates (55). F/M alloys are particularly vulnerable to LME because they have a ductility trough between 150 and 400 °C (56), while austenitic stainless steels are not susceptible. They do, however, show the local penetration of grain boundaries by HLMs, which leads to the leaching of Ni and an austenitic-to-ferritic phase transformation (57).

LMC includes two primary mechanisms: dissolution and oxide-formation. Dissolution typically involves the selective leaching of higher solubility elements from the steel (58). In general, dissolution corrosion should be avoided by supplying enough dissolved O to the LBE to promote the formation of thin adherent oxides on the steel (see Section 3.2.2). In addition to the dissolved O content, both dissolution and oxide formation are dependent on temperature, flow velocity, steel composition and microstructure, as well as pre-exposure (radiation) and surface preparation (roughness, weldments). Both processes will be discussed in more detail in Section 3.2.1. While LMC could cause system failure in the long run, it is important to note that the processes are slower and significantly more gradual than in LME. The goal for LMC mitigation is therefore to decelerate the process beyond a reactor's lifetime, rather than to completely prevent it.

Erosion corrosion and fretting wear are sometimes also considered part of LMC. Erosion tends to be a consequence of two-phase flow where fast-flowing LBE carries solid particles, such as oxides, that act as abrasives for adherent protective oxide layers or dissolution-affected areas. Fresh unprotected metal is exposed to LBE wherever these existing layers are eroded away, which greatly accelerates corrosion rates. Its severity is primarily dictated by flow velocities and debris content of the HLM. Fretting typically occurs on tightly spaced components that are nominally in static contact. Microscopic sliding of the surfaces against each other, e.g., due to vibration or thermal cycling, may locally create cracks and expose fresh metal to dissolution-dominated crevice corrosion conditions (59). The main factors affecting fretting wear are the frequency and the magnitude of the motion between the affected surfaces.

3.2.1. Liquid metal corrosion (LMC)

To set the stage for the main topic of this dissertation – irradiation-corrosion interactions in materials – this section will discuss the two primary LMC mechanisms in HLMs: dissolution and oxide formation. Substantial detail on these mechanisms can be found in (34, 51, 60). As mentioned in previous sections, while LMC by itself is typically not the life-limiting factor of an LFR component, it does play a role in constraining the elemental compositions of structural alloys as well as in affecting critical processes like embrittlement via the local depletion of alloying elements and oxide formation.

3.2.1.1. Dissolution

Common steel alloying elements, such as Ni and Cr, have rather high solubilities in pure Pb and LBE. The solubility can be expressed as

$$\log(S[wt\%]) = A - \frac{B}{T[K]} ,$$

where S is the solubility in wt%, T is the temperature in K, and A and B are coefficients listed in Appendix 8.2 in Table 9 (21). With the suggested solubility laws, the solubility curves shown in Figure 2 are obtained, which show that Ni is extremely soluble in both Pb and LBE at LFR-relevant temperatures (approximately 600 – 1000 K).

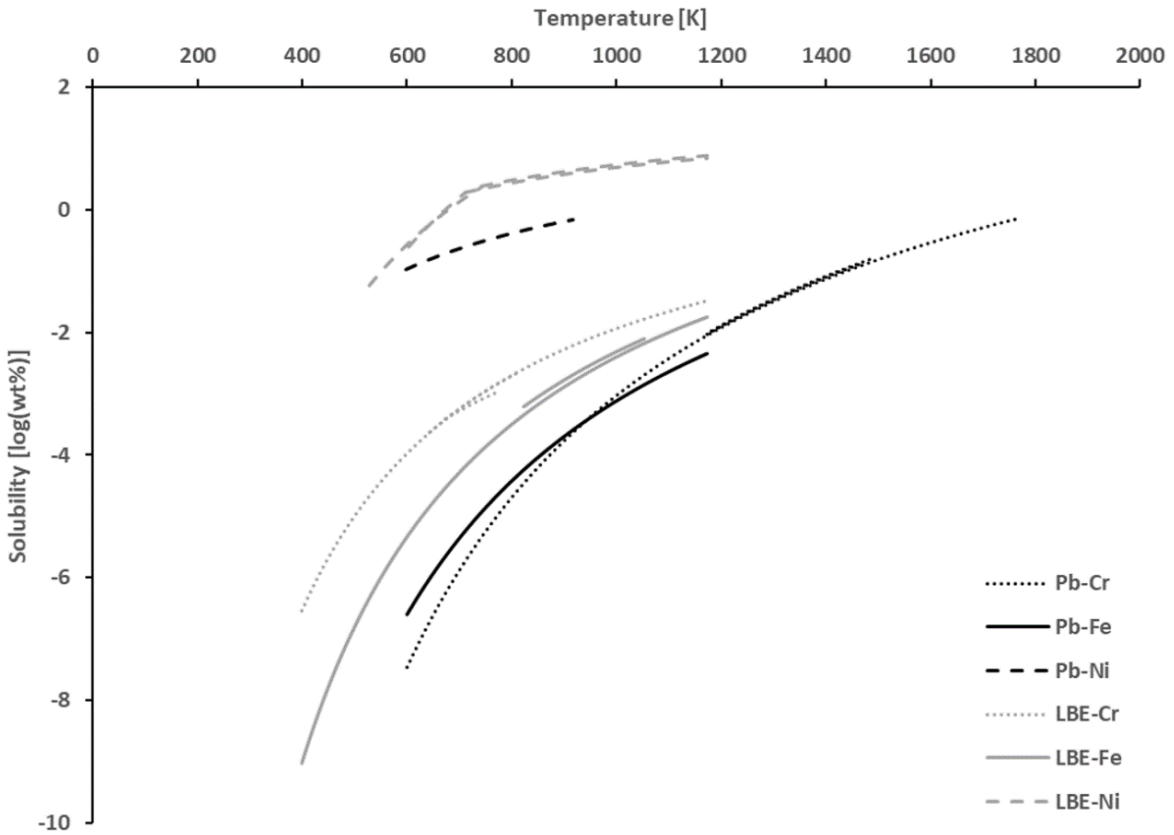

Figure 2 – Solubilities of Cr, Fe, and Ni in Pb and LBE with temperature based on recommendations in (21) (see Appendix 8.2).

The selective loss of highly soluble elements is typical for many alloys, but depending on the chemical composition of the steel, dissolution may also occur uniformly (58, 61, 62). Even in O-rich oxide-forming environments (see Section 3.2.1.2), dissolution can be enhanced locally and take place as pitting corrosion where dissolution pits form underneath an oxide layer (63, 64).

In a static system, the concentration of dissolved species in the HLM would eventually reach equilibrium and prevent further dissolution. In non-isothermal flow loops, temperature differences provide a thermodynamic driver for the continuous transport of metal from the hot leg to the cold leg. Another driver for continued dissolution corrosion is the formation of intermetallic phases in the liquid, which continuously removes dissolved species from solution.

Large mass transfer rates can lead to wall thinning of components in some regions of the reactor, which increases the risk for pipe bursts and cladding failure. In those areas where deposition occurs, coolant flow can be constricted, which could ultimately interrupt flow back to the reactor core (see, e.g., plugging in the CICLAD loop (21)). For steels in HLM flow loops, the dissolution rate in the hot leg and the precipitation rate in the cold leg are generally negatively correlated with the dissolved O concentration in the flowing HLM, and positively correlated with the Fe diffusion coefficient (65, 66). Ultimately, the achievable ΔT across the reactor is the main driver for mass transfer between the hot and the cold leg and is therefore limited by dissolution and plugging (21). Therefore, controlling mass transfer by decreasing metal dissolution is extremely important for the longevity of an LFR.

As an aside, dissolution resistance of the cladding to acid is also relevant for fuel reprocessing, where U and Pu are extracted for recycling. Fast dissolution of the cladding is undesirable because its species enter solution alongside the desired compounds (15). In this context, the dissolution of

austenitic stainless steels is generally acceptable, while ferritic alloys dissolve much more rapidly (15).

3.2.1.2. Oxide formation

With sufficient dissolved O present, steels in HLM environments may form protective multilayered oxides. Figure 3 shows the thermodynamic stabilities of different metal oxides in LBE. The formation of initially fast-growing, thin, dense, and adherent oxides is desirable to protect the metal from further corrosion while preventing oxide spalling. Especially for components whose primary purpose is heat transfer, such as the cladding and heat exchanger tubes, the reduction of their heat transfer coefficient by oxides must be limited. Oxides that follow a logarithmic growth behavior are ideal for these applications although slow linear growth is also acceptable.

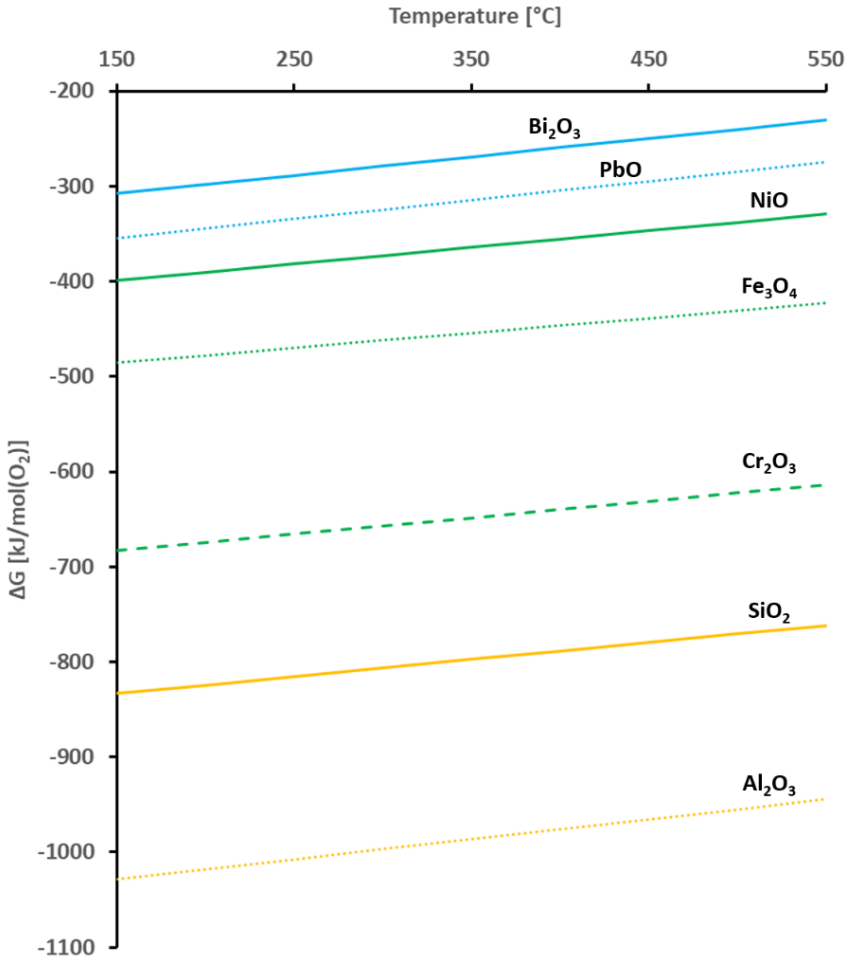

Figure 3 – Ellingham diagram for Pb and Bi oxides (blue), major alloying elements in steels (green) and select corrosion resistant alloying elements (yellow) based on data in Table 4.2.2 in (21).

If the dissolved O content is too high, the HLM itself will be oxidized, which can lead to plugging. The formation of PbO therefore typically constitutes the upper boundary for the acceptable dissolved O concentration in a HLM system, while the minimum concentration is defined by the stability of Fe_3O_4 (see blue curves in Figure 4). As the HLM circulates through the

reactor and experiences temperature changes, the dissolved O concentration must remain below the PbO formation limit and above the Fe_3O_4 stability limit to maintain oxide layers on metals while preventing plugging. The convergence of the red curves in Figure 4 indicates the stoichiometric line for the solubility product of Fe_3O_4, above which an exclusively oxide-forming environment (empty triangles) is typically maintainable (67). This indicates that at a typical LFR operating temperature of ~500 °C, a concentration of ~10^{-6} wt% dissolved O is desirable. Below the stoichiometric line, but above the magnetite stability limit, experiments have shown the occurrence of dissolution corrosion, even in the simultaneous presence of an oxide. Such a mixed oxide formation / dissolution corrosion mode will also be seen in some of the results of this work (see Section 4.4). Above a certain temperature threshold, however, dissolution may be present regardless of the dissolved O concentration, as indicated by the two black circles above 550 °C, which are located well above the stoichiometric line. The exact temperature threshold is dependent on the material and the dissolved O concentration, and may be extremely high, such as in the case of AISI 304L (68).

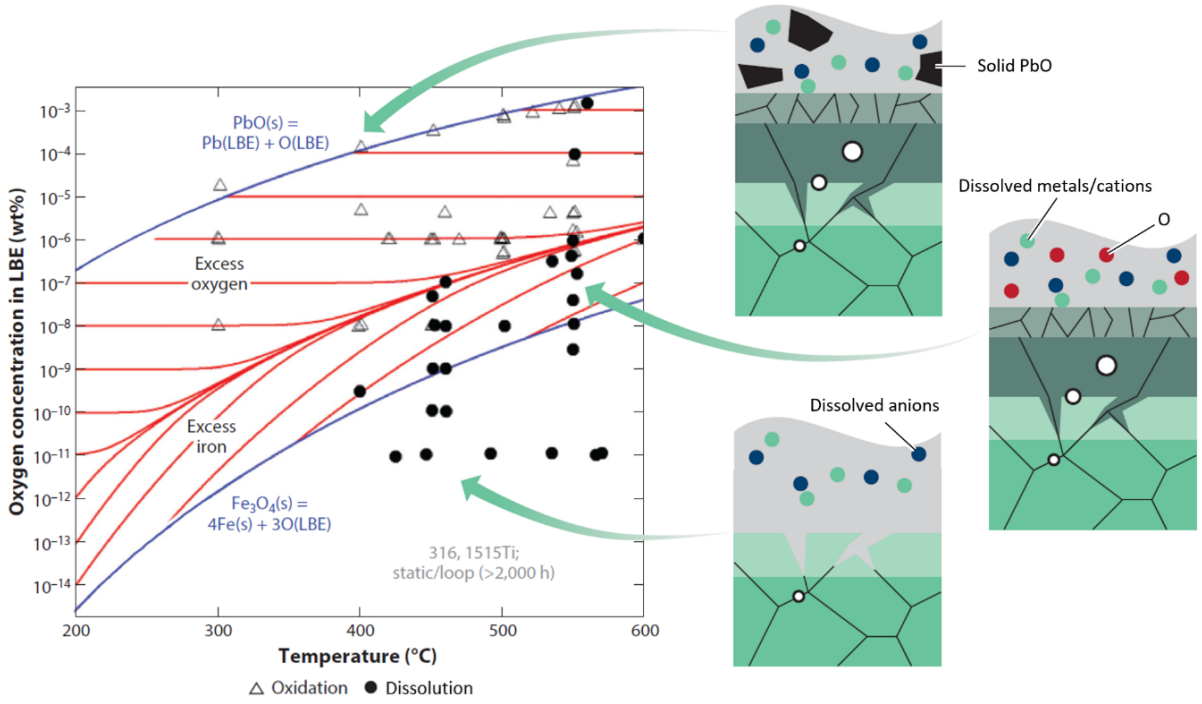

Figure 4 – Left: dissolved O content in LBE with temperature, showing the useful range of O to control corrosion rates in LFRs. Blue lines indicate the upper limit (PbO formation, illustration top right) and the lower limit (magnetite stability limit, illustration bottom right). In between is the operational regime, where protective oxides should form theoretically (illustration center right). Open triangles show the formation of oxide layers in various corrosion experiments; Filled circles show the occurrence of dissolution, with or without the presence of a simultaneous oxide. Figure adapted from (26) which adapted the plot on the left from (67).

In F/M steels, the oxide typically has a duplex structure with an outer magnetite layer and an inner Fe-Cr spinel layer (34). Austenitic stainless steels can form more complex oxides with a three-layer structure (69, 70). The exact nature and the structure of the oxide layers produced in HLMs tend to be temperature-dependent (71). Sublayers are often observed in the main oxide layers. For example, the outer magnetite layer on F/M steel is two-layered with an outer, more columnar layer (perpendicular to the steel surface), which allows for ingress of LBE along grain boundaries, and an inner, more equiaxed layer (72). (69) found that there is a Ni-depleted region

in the inner layer and that other areas of the inner oxide showed interconnected porous channels, especially along grain boundaries.

F/M oxide-dispersion strengthened (ODS) steels behave similarly to F/M steels in general, although the smaller grain sizes appear to be detrimental for initial dissolution resistance, but beneficial for corrosion resistance in the long-term (15). The addition of certain additives, such as Si and Al, can lead to the growth of an oxide rich in these elements, which can be very stable (see Figure 3) and passivating (73). This motivates the use of Al-rich alloys, such as Fe-Cr-Al alloys, or surface treatments of steels, e.g., with an Al-rich weld overlay (74).

Once the oxide is formed, corrosion rates are governed by diffusion through the oxide layer. O diffusion is very fast due to the presence of nanochannels in the oxide (75, 76). Steel alloying elements with higher solubility in HLMs are subject to a stronger driving force for diffusion through the oxide. (76) demonstrated that for the corrosion of Fe9Cr1Mo in LBE, Fe diffusion through the oxide is rate-limiting for its growth. This is further corroborated by the observation that the corrosion rates of pure Fe and F/M steels tend to be the same, at least within the time frame of the reported corrosion experiments (see, e.g., the oxide growth rates of pure Fe (77) compared to T91 (78) in flowing O-rich LBE at 450 °C or the dissolution rate of pure Fe and T91 in O-poor (10^{-8} wt% or lower) flowing LBE at 450-540 °C (79)).

The diffusion of species from the base metal to the oxide / HLM interface creates pores at the base metal / oxide interface (80). The presence of these pores decreases the contact area between the base metal and the oxide, which reduces the overall diffusion rate of base metal species and therefore decreases the oxide growth rate. If the pores continue to grow, the adhesiveness of the oxide with the base metal decreases. Pore growth may be mitigated by diffusion of species from the base metal towards the interface or by oxide growth. In general, outer oxides grown in HLM environments are thought to grow at the oxide/HLM interface via cation diffusion from the base metal to the HLM, while inner oxides are though to grow via O diffusion through the oxide towards the metal/oxide interface. There, the space left behind by cations diffusing towards the HLM is required to accommodate oxide growth at the interface with the base metal, which is a concept known as the “available space model” (see, e.g., (76)). The interface between the two oxides is typically thought to be the original metal/HLM interface.

The HLM is often found at the interfaces between multilayered oxides (see e.g., (77, 81)) and between the oxide and the base metal (see, e.g., (82) and this work). Its presence combined with the stresses developing in the growing oxide promote oxide buckling and detachment. The protectiveness of the oxide therefore depends on its resistance to HLM penetration, its growth rate, as well as its ability to maintain sufficient contact with the base metal, which is dependent on the oxide’s ductility as well as the diffusion of oxide-forming species through the base metal and the oxide.

3.2.2. Corrosion mitigation

There are two main ways of mitigating corrosion in a liquid metal system: 1) increasing the corrosion resistance of the material, and 2) decreasing the corrosivity of the corrosive medium. In the case of HLMs, additives such as Al and Si may increase the corrosion resistance of steels. However, the addition of alloying elements for corrosion resistance may have undesirable side effects with respect to other properties, such as mechanical properties or radiation response. In addition, manufacturing, machining, and welding of such alloys can be quite challenging. Finally, many currently available alloys already show rather high corrosion resistance in HLMs. Other

areas, such as resistance to LME and high temperature mechanical properties drive the continued development of alloys, and corrosion resistance serves mainly as a boundary condition.

This shifts the focus to the other corrosion mitigation option, which is to lower the corrosiveness of the HLM. This could be achieved by making changes to the reactor design, for example by lowering the operating temperature to reduce LMC or by reducing flow velocities through the core and flow pattern instabilities to limit erosion corrosion (51). However, the former option limits the efficiency of the reactor and therefore makes it less economically viable. Alternatively, the HLM dissolved O content can be controlled to maintain an environment where passivating oxides can be formed (see Figure 4) to limit the severity of corrosion (83, 84). This is generally considered the main strategy to mitigate corrosion in LFRs.

3.3. Irradiation effects in nuclear environments

Ionizing radiation interacts with the electrons and/or the nuclei of target atoms, depending on the mass and charge of the projectile. This is schematically shown in Figure 5. In nuclear reactors, the primary radiation types of note are neutron and γ radiation resulting from nuclear fission. Generally speaking, neutrons are responsible for producing radiation damage in reactor materials, while γ radiation generates heat. The radiation damage created by neutrons is of two types: transmutation (predominantly at lower energies) and displacement damage (high neutron energies).

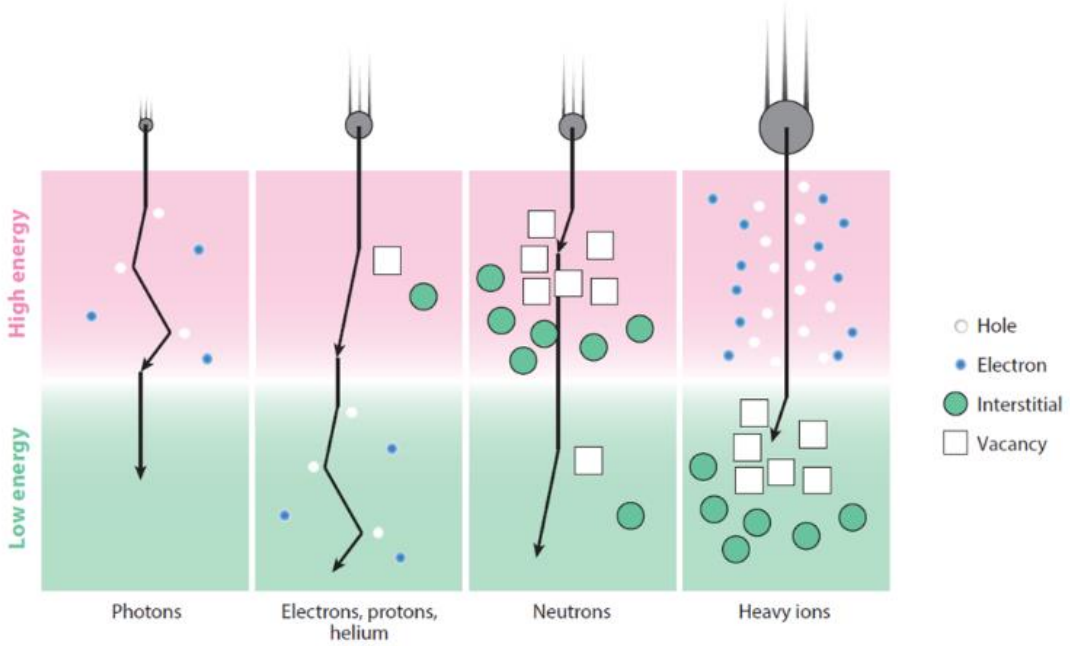

Figure 5 – Illustration showing how different energetic particles interact with matter. Interactions depend on the particle's charge state (uncharged photons and neutrons vs. charged electrons and ions) mass, and energy. Adapted from (26).

Displacement damage is measured in displacements per atom (dpa), which is the average number of times every atom in the lattice has been displaced hypothetically due to radiation damage. This number can be used to compare a material's exposure to different particle energies and ionizing radiation types. It does not, however, capture the number of defects surviving the collision cascade, which is determined by the material-specific recombination rate.

The displacement of atoms creates Frenkel pairs, i.e., vacancy-interstitial pairs, and other point defects in the crystal lattice. These 1D nonequilibrium defects are mobile but migrate through the solid at different rates (vacancies more slowly, interstitials faster). If they do not annihilate, they can form or feed into larger-scale defects, such as dislocation loops and precipitates, which may cause radiation hardening, and voids, which act as obstacles to dislocation motion (see Figure 6). They can lead to processes that affect the material's chemistry, e.g., via radiation-enhanced diffusion (RED) or radiation-induced segregation (RIS). Point defect migration may also change a metal's long-scale grain structure, either coarsening it due to enhanced kinetics, or refining it, e.g., as seen in the creation of the rim structure in nuclear fuels (85). Finally, radiation-induced defects can interact with other materials degradation mechanisms, such as radiation embrittlement, and lead to complex effects like IASCC if stresses are present (86).

All these processes are highly temperature-dependent because the annihilation rate of point defects increases with temperature. Another important parameter is the damage rate, which is weakly coupled with the density of the damage cascade. The more defects are created in the same region, the higher the likelihood of recombination, which means that the increase in the number of surviving defects is not proportional to the increase in damage rate / cascade density.

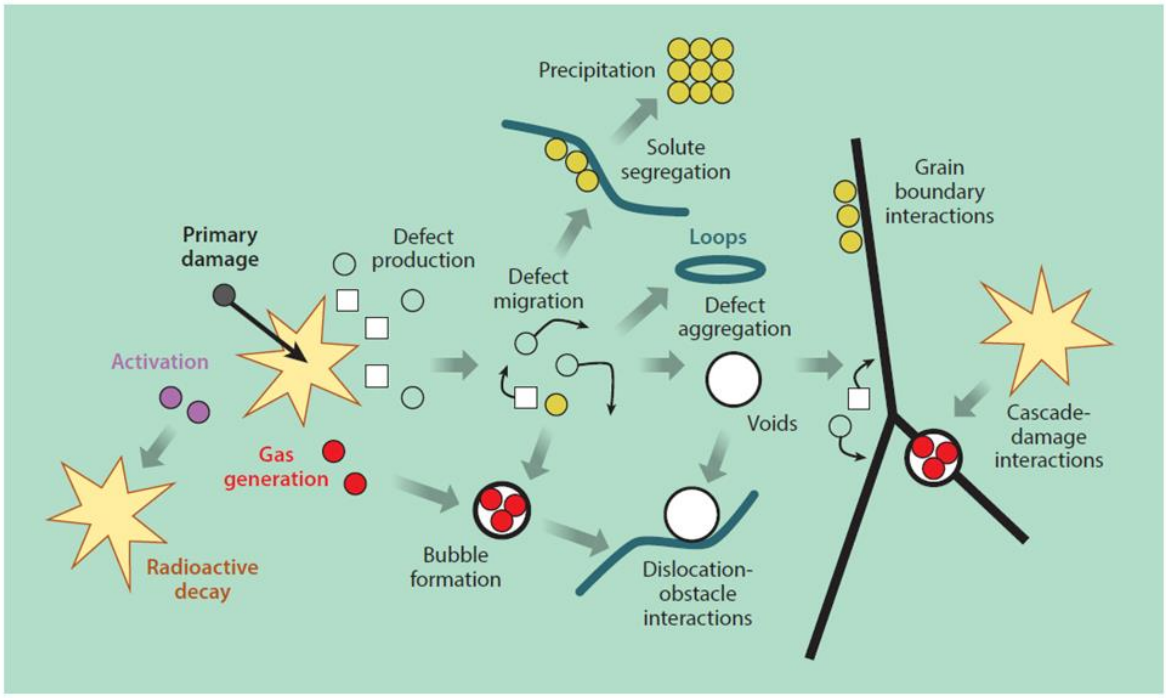

Figure 6 – Illustration of the various fates of radiation-induced point defects in a solid. Adapted from (26).

In LFRs, 95% of the displacement damage in materials located in and near the core is created by neutrons with a negligible contribution from charged particles and photons (15). Compared to LWRs, the total dpa is significantly higher due to the necessarily higher neutron flux. Because LMs, especially HLMs with their high Z, do not substantially moderate neutrons, the neutron spectrum contains practically no thermalized neutrons. While this enhances Pu breeding from ^{238}U by decreasing parasitic neutron capture, it also reduces the integrated fission cross section of ^{235}U by a factor of ~400 (15). This implies that the neutron flux needs to be increased by approximately two orders of magnitude to maintain a given power density, which can be achieved by increasing

fuel enrichment by roughly an order of magnitude. However, this also results in a factor of 100 times more neutron exposure of the fuel cladding in a fast reactor compared to an LWR (15). Radiation-induced effects described in this section that occur at lower and sometimes negligible rates in LWR cladding materials may therefore be greatly accelerated in LFRs (see review in (45)). The focus here is on those mechanisms that may have an impact on corrosion in structural materials. More detail can be found in recent reviews (87–89).

3.3.1. Irradiated microstructure

The microstructure of materials in reactor environments changes drastically with temperature and dose. Below ~300 °C, it is dominated by dislocation loops. The loop number density and loop size in stainless steels are dose-dependent, with the former saturating around 2 dpa and the latter around 5-7 dpa under LWR conditions (see Figure 5 in (90)). Above 300 °C, the nucleation of voids begins and becomes increasingly more important at higher temperatures (see, e.g., (91)). The microstructure evolution under irradiation is influenced by several factors. The presence of dopants, for example, may impact dislocation motion and void / He bubble nucleation. When dislocation motion is impeded, e.g., by radiation-induced defect clusters or other dislocations, the material hardens. The continued growth of cavities will eventually lead to macroscopic swelling and radiation embrittlement. Since both dislocations and voids are point defect sinks, their density, distribution, and size are highly relevant to the progression of corrosion under irradiation.

3.3.2. Radiation-enhanced diffusion (RED) and radiation-induced segregation (RIS)

RED and RIS are strongly influenced by the defects that escape the collision cascade and migrate before recombining or annihilating at a defect sink. A preferential attachment of alloying species to a defect flux, either interstitials or vacancies, leads to segregation via defect migration. For example, the migration of vacancies towards sinks leads to a segregation of the slowest diffusing species of those migrating via vacancy exchange, which is known as the inverse Kirkendall effect. In an FeCrNi system, for example, the difference in diffusion coefficients ($D_{Cr} > D_{Fe} > D_{Ni}$) leads to the formation of Ni-rich zones around vacancy sinks (92). Another process that primarily appears to affect small elements is solute drag, where a defect-solute complex forms that allows the solute to follow the defect concentration gradient (93, 94). For example, phases rich in Si and Ni may form as a result of the combination of the inverse Kirkendall effect and the migration of interstitial-Si complexes (45).

RIS can drive equilibrium phases toward instability and locally lead to the formation of non-equilibrium phases (typically 5-10 nm from a sink, such as a grain boundary (GB) (95)), which may render these regions more or less prone to corrosion. This process generally occurs at intermediate temperatures, i.e., 30-50% of T_{melt}, which corresponds to the higher end of the LFR operating temperature range for common steels.

3.3.3. Transmutation products (TPs) and fission products (FPs)

Radioactive isotopes, such as ^{54}Mn, ^{51}Cr, ^{59}Ni, ^{58}Co, ^{60}Co, and ^{110m}Ag, are released from the fuel or the fuel cladding under normal operating conditions in an LFR and accumulate in the coolant over time (see Table 4.3.1 in (21)). In the case of off-normal cladding failure, other contaminants, such as ^{239}Pu, ^{235}U, ^{85}Kr, minor actinides, and Cs, I, Kr, and Xe nuclides may be

released in addition (21). In ADSs, coolant activation is dominated by ^{210}Po (21), which is also produced in LFRs if LBE is used as the coolant, where it acts as a neutron poison:

$$^{209}Bi + n \rightarrow \quad ^{210}Bi \xrightarrow[\beta^-,\ t_{1/2}=5\ days]{} \quad ^{210}Po \xrightarrow[\alpha,\ t_{1/2}=138.4\ days]{} \quad ^{206}Pb\ .$$

Many nuclear reactions produce He, which is known to affect the microstructural evolution of materials (96). The primary early He sources in fast reactor structural materials are (n,α) reactions of fast neutrons with Ni (45). For many steels, the Ni concentration is almost perfectly proportional to He production under irradiation (see Figure 6-4 in (45)). Some He is also produced by (n,α) reactions of low energy neutrons with B impurities in steels as in thermal reactors, but due to the fast neutron spectrum this effect is relatively small compared to He production by Ni. Several reactions also produce H, which is very mobile in steels and therefore has a lesser impact on the microstructure because it does not readily form bubbles like He.

FPs and TPs can negatively affect structural materials in the system. While this is not a significant issue for current reactor temperatures and fuel burnups, it may become extremely important with higher burnup (15). Transmutation in austenitic and especially ferritic steels in fast reactors is generally limited, at least for the first 100 dpa (15), but it may become relevant during prolonged exposure.

3.3.4. Radiolysis

In water and ionic liquids, radiation is known to be able to break chemical bonds in the fluid, which leads to the formation of highly reactive radicals and an increase in electrical conductivity. Radiolysis of H_2O creates H^+ and OH^- and a host of species that consequently form locally, such as H_2O_2, which can change the oxidizing power of water (97). Radiolysis has a significant impact on corrosion in LWRs, specifically by radiolysis products contributing to IASCC, and the increase in electrical conductivity promoting galvanic processes, such as shadow corrosion and nodular corrosion in boiling water reactors (BWRs). However, in LMs, radiolysis cannot occur and therefore cannot contribute to corrosion in LFRs.

3.4. Materials candidates

The main materials challenge in fast reactors is to find cladding and wrapper tube materials that allow the doubling of currently achievable burnups of 10-12 at% to make fast reactors economically feasible (15). This requires materials that resist void swelling, excessive radiation embrittlement, and loss of high temperature strength over the 2-4 years of residence time in the core. While interactions with the coolant are relatively limited in SFRs, materials exposed to HLM-coolants have to resist LMC and LME (see Section 3.2) in addition to radiation-induced damage, stresses, as well as TPs and FPs, which are all present simultaneously. (15, 51) provide excellent and more in-depth overviews of the various materials considered for HLM environments than the summary that will be presented here. The compositions of materials mentioned in this section are shown in Appendix 8.3.

3.4.1. Austenitic stainless steels

Austenitic stainless steels have a face-centered cubic (fcc) crystal structure and have been used as reactor pressure vessel liners and core-support structures in LWRs. In particular 316 LN (L: low C, N: low N) and 304 LN are often chosen because the limited amount of C reduces sensitization during welding and the upper limit of 0.08 wt% N also improves weldability and minimizes scatter in mechanical properties (15). They have also been used as fuel cladding in SFRs, where they show good performance under typical SFR temperatures (350 – 475 °C) (15), which are substantially lower than desired LFR temperatures. However, these alloys can also show significant void swelling under irradiation (98), which causes severe embrittlement and hardening. Void swelling can be reduced by increasing the ratio of Ni to Cr up to 35-40% Ni when swelling again increases with Ni content (99). However, high Ni levels in HLM environments are generally undesirable because the Ni will be leached out, especially at temperatures > 550 °C, and can form intermetallics in the coolant. In addition, it is also expensive, has a tendency for radiation-induced phase instability, and generates He from parasitic neutron capture (15). A reduction of Cr concentrations would also reduce void swelling, but Cr is necessary for corrosion resistance (100, 101).

Void swelling is generally reduced by increasing point defect sink density, e.g., by cold-working the material, which is known to delay the onset of void swelling (15), or by increasing vacancy mobility, which can be achieved by small additions of Si (0.8 wt% (15)) and P (93, 100, 102), for example. The strongest swelling reduction is achieved by P, then Si, and then Ni on a per atom basis (100). However, RIS tends to remove these elements from the matrix and to bind them in precipitates. The presence of carbide-forming elements, such as Ti, Zr, Nb, and Hf, is supposed to delay this removal from the matrix, which leads to the 316Ti grade, the 15-15Ti grade (15Ni-15Cr), and similar alloys, which can show significant void swelling suppression, even beyond 210 dpa (15). The addition of Nb, V, Zr, and Ta increases phase stability, while the addition of Mo improves high-temperature strength (51). Finally, alloys for in-reactor service are generally cold-worked up to 20% to improve mechanical properties as well as swelling and corrosion resistance (15).

3.4.2. Ferritic / Martensitic (F/M) steels

Of the body-centered cubic (bcc) ferritic and F/M steels, particularly those with 9-12 wt% Cr and up to 0.1-0.2 wt% C are often considered for LFR service due to a combination of good mechanical properties, even at elevated temperatures up to ~600 °C, low thermal expansion, and high resistance to radiation embrittlement and void swelling (33, 103, 104). However, F/M steels have unsatisfactory long-term creep resistance above 600 °C, which limits the operating temperature of the reactor significantly. Below 400-450 °C, radiation embrittlement becomes a concern (105, 106), which drastically limits the operating temperature range. 9 wt% Cr is preferable because 9Cr F/M steels, such as T91 or HT-9, show the lowest ductile-to-brittle transition temperature (DBTT) after neutron irradiation (103, 107). However, 12 wt% Cr alloys have been shown to swell significantly less (15), and a higher Cr content increases corrosion resistance. Excessive amounts of Cr may lower the steel's ductility and fracture toughness, which is exacerbated by radiation (108). A significant downside to F/M steels is that they are quite susceptible to LME starting at 200 °C (52), while austenitic stainless steels are less so (109).

Additions of small amounts of alloying elements can produce F/M alloys that show negligible swelling, even at high doses, and a small DBTT shift, such as EM10 (9Cr-1Mo), which was used as the wrapper tube material in the Phénix and Superphénix SFRs. However, its low strength and

thermal creep deformation at high temperatures limits its use to the wrapper tubes where temperatures do not exceed 550 °C (15). Addition of Al (73) and Si can also significantly increase corrosion resistance in F/M steels, such as EP823 with 1.5 wt% Si (110). F/M steels with 5.5 wt % Si have been shown to have no sign of corrosion attack (111). Some international programs have shifted their attention to the production of oxide-dispersion strengthened (ODS) ferritic alloys, which are supposed to withstand up to 250 dpa at temperatures as high as 700 °C (112). Common additions are Mo, V, W, Nb, and B, all of which show promise based on available data (15).

The introduction of new alloy classes is not just dependent on their predicted performance based on laboratory experiments, but also on the ability to manufacture them in bulk, their machinability, and their weldability. In the case of F/M ODS alloys, production on a small batch scale (~10 kg) or pilot plant scale (~1 metric ton) has been demonstrated, potentially making them viable for in-reactor deployment (15).

3.5. Known irradiation-corrosion processes

3.5.1. Evidence of effects of irradiation on corrosion in nuclear reactor environments

Radiation damage spans length and time scales from electrons and femtoseconds to human-scale parts that evolve over decades or longer. Equilibrium and radiation-induced defects have a number of effects like those described in Section 3.3 that alter a material's mechanical properties by affecting the base metal, the corrosion layer, and the corrosive medium. Therefore, it seems sensible that they should affect corrosion resistance as well.

A historical example for how the understanding of irradiation-corrosion interactions evolves over time is the observation of enhanced corrosion of Zircaloy in LWR environments. Providing experimental proof for the existence of such effects and explaining the underlying mechanisms took decades of research (113). Some studies suggested that radiation only has a minor impact on Zircaloy corrosion rates (114, 115), with others showing drastic rate increases (116–118). Eventually, evidence mounted that the primary culprit is radiolysis, with other contemporary studies suggesting that radiation may also impact the base metal and/or the oxide layer (119). While radiolysis is known to play a role in IASCC (120), the majority of irradiation-corrosion effects in Zircaloy has since been explained with the radiation-induced redistribution of Fe from precipitates to the matrix (113).

This example shows the importance of accelerated laboratory experiments that will be discussed further in Section 3.6.2. The aim of this section is to set the stage by discussing the various ways in which irradiation may affect corrosion in the absence of applied stress. It is largely based on (26), where the current state of knowledge regarding materials response to simultaneous exposure to radiation and corrosion by water, HLMs, and molten salts was reviewed in more detail than will be presented here. First, a few factors that have been found to affect irradiation-corrosion processes, such as dissolved O and temperature, will be discussed, followed by an overview of where in the system – the base metal, the corrosion layer, or the liquid phase – irradiation is likely to have an impact on corrosion. Most examples are based on Zircaloy corrosion in aqueous environments because it is the most well-studied pair of material and coupled irradiation-corrosion environment. Known irradiation-corrosion processes in HLM environments are summarized at the end of this section (see Section 3.5.1.8).

3.5.1.1. Dissolved O concentration

The dissolved O concentration of the corrosive medium plays a crucial role in any oxide-forming system. In the Zircaloy-water system, oxide layer growth rates are thought to be limited by O-diffusion. For Zircaloy-2 and Zr-2.5%Nb, a strong enhancement of radiation-induced corrosion was observed for increasing dissolved O concentrations in water (118). In fact, high amounts of dissolved O and radiation must be present simultaneously to increase corrosion rates (121). Dissolved O concentrations have also been found to be a relevant factor for shadow corrosion in Zircaloy (113, 122). For HLMs, the situation may be a bit different since O is generally thought to be available at the metal-oxide interface ((75, 76), see Section 3.2.1.2). However, the radiation-induced increase in electrical conductivity of the oxide that is partially responsible for the accelerated corrosion of Zircaloy may also change the response to different dissolved O concentrations in HLMs.

3.5.1.2. Temperature effects

Temperature can affect both corrosion kinetics and radiation-induced defect recombination, so it should influence their interaction as well. Since the annihilation rate of radiation-induced defects increases with temperature, their impact on corrosion should decrease at high temperatures (123). For Zircaloy in aqueous environments, one study found radiation-enhanced corrosion at lower temperatures (250-350 °C), but not at 400 °C or above (118). Temperature changes of ~100 °C have also been found to induce a long-term (~1000 days) hysteresis effect in the oxide growth rate, such that a Zircaloy-4 sample initially irradiated at 360 °C and then shifted to a lower temperature (275 °C) exhibits the corrosion rates typical of an unirradiated sample compared to one continuously irradiated at the lower temperature (124). Temperature has also been found to impact the type of corrosion that occurs, e.g., in fuel rods that operate at lower temperature due to lower heat flux and are more susceptible to nodular corrosion as a result (125).

In steels, the primary focus of irradiation-corrosion interactions is on IASCC. Other effects, where stress does not play a significant role, are generally less well-studied in aqueous environments. Nevertheless, one study showed that grain boundary attack in proton-pre-irradiated AISI 304 was higher for high-temperature irradiation conditions (773 K) than low temperature conditions (573 K, 673 K), which the authors ascribe to RIS outcompeting defect recombination at higher temperatures (126).

3.5.1.3. Dose rate effects

The oxidation rate of Zircaloy in water has been observed to vary with fast neutron flux, such that a higher flux leads to higher corrosion rates (127). Previously, however, corrosion rates were found to saturate above a certain flux, which was unfortunately not quantified (117). The dose rate can also create a flux-dependent hysteresis effect similar to the temperature-induced effect described in the previous section (124).

3.5.1.4. Effects on the base metal

In aqueous environments, radiation-enhanced corrosion is heavily dominated by processes related to radiolysis, and so, little attention has been paid to how radiation-induced defects in the solid affect corrosion. One important example to the contrary is radiation-enhanced corrosion in Zircaloy. After decades of research, this was eventually explained with the redistribution of alloying elements, specifically Fe, from precipitates to the matrix (113, 128). Corrosion resistance

of Zircaloy-2 and Zircaloy-4 is known to be strongly dependent on precipitate size, composition, and distribution (129). Studies have shown that these precipitates can be dissolved by fast neutron irradiation, which leads to the release of Fe, Cr, and Ni to the matrix (130, 131), and an increase of corrosion under irradiation. The hysteresis effect mentioned in Section 3.5.1.2 also hints at defects in either the metal or the oxide layer having a lasting impact on corrosion, but it is not clear where exactly the defects are created.

3.5.1.5. Effects on the corrosion layer

Oxides are normally electrical insulators, but under irradiation their electrical conductivity can be increased (see, e.g., (132)), which potentially increases the reactivity of species at interfaces and changes electron transport, which may accelerate corrosion. In Zircaloy, the aforementioned redistribution of Fe may cause it to be enriched along c-loop dislocations, which could lead to the formation of Fe-oxide grains that serve as local high-conductivity paths (113, 133). In BWRs, a mechanism for oxide dissolution induced by high energy photons has been proposed (134), which may explain observations that γ flux can have an impact on Zircaloy-4 corrosion (128). Interestingly, in-reactor radiation does not appear to have a significant effect until the Zr-oxide reaches 5-6 µm thickness (113).

3.5.1.6. Effects on the liquid – radiolysis and impurities

The changes in water chemistry due to radiolysis are known to affect corrosion of stainless steels (97, 135). In combination with stress, radiolysis contributes to one of the primary failure mechanisms in LWRs: IASCC (136). This is a heavily studied and reviewed (see, e.g., (86, 87, 120)) mechanism in aqueous environments and will not be discussed further here because it requires the additional presence of stress. In contrast, little attention has been paid to radiolysis-induced effects that are not cracking-related. An example to the contrary are ion-irradiation studies on AISI 316L that have shown that the presence of radiolysis products may promote Cr depletion in the oxide in nearby areas outside the beam spot, while T91 did not show this depletion (137). Similar studies on AISI 316L showed that the inner and outer oxides formed in the beam spot and nearby were similar in appearance, which was attributed to the presence of radiolysis products in and near the beam spot (138, 139). A comparison with a pre-grown oxide showed porosity and Cr-depletion only in the beam spot, however, which indicates that radiolysis is not the only active process.

The metallic bonds in HLMs prevent the occurrence of radiolysis effects in a manner analogous to water. Therefore, the impact of radiation on the liquid phase is limited to the production of impurities, either directly (TPs) or indirectly (FP release). Volatile FPs, such as Cs and I, can interact with the inside of the cladding tube and lead to corrosion and grain boundary attack (15). In rare cases, the presence of FPs may result in less corrosion, as observed in the Molten Salt Reactor Experiment (MSRE), where the deposition of noble metal FPs possibly lead to passivation (140). In the context of ADSs, lanthanides have been found to deposit on free metal surfaces, but their impact on the corrosion process was not explicitly studied (141).

3.5.1.7. Radiation-decelerated corrosion

In addition to the noble metal deposition in the MSRE mentioned in the previous paragraph, there are a few other cases where irradiation has been observed to decelerate corrosion. In Zr-2.5Nb in water, there is evidence that corrosion can be decelerated by irradiation in the pre-

transition phase (118), even though radiation is generally thought to only affect the post-transition phase. More recently, molten salt corrosion was observed to be decelerated in some cases by both simultaneous proton irradiation (Ni-20Cr in FLiNaK) (142) and neutron irradiation (316L and Hasteloy N in NaCl-$MgCl_2$) (143). A decrease in intergranular oxide penetration due to proton irradiation was also found for 316L in high temperature water (144).

3.5.1.8. Irradiation-corrosion effects in heavy liquid metals

In HLMs, irradiation-corrosion interactions should be less complex than in aqueous environments for several reasons: 1) the impact of γ radiation on parts that are outside of the core should be significantly reduced or non-existent because of the high density of HLMs; 2) radiolysis cannot occur; and 3) LFRs are designed to operate at higher temperatures than LWRs, which increases the recombination rate of point defects. In addition, TP production in an LFR is not thought to be a significant factor and neither are the associated potential effects on corrosion, at least during the first half of the reactor's life (15). In ADSs, however, the intense proton and neutron fluxes will likely make transmutation a bigger issue than in LFR environments.

Experiments with steels, such as T91, MANET II (a 12Cr-1Mo-NbV steel), and AISI 316L under simultaneous proton irradiation (72 MeV) and exposure to flowing LBE have shown that oxides are thicker in the beam spot for long experiment durations (> 200 hours (145, 146)) or that the beam spot is the only location where an oxide is present for irradiation times too short for oxides to form elsewhere (147). Similar inhomogeneities in oxide thickness were observed in HT-9 exposed to 5.5 MeV protons and static LBE (420 °C) for 58 hours (148) and 11Cr1W1Si F/M steel exposed to 5 MeV protons and static LBE (400 °C) for 17 hours (40 hours total corrosion time, (149)). Heavy ion irradiation with 247 MeV Ar of SIMP steel (a martensitic steel with 10.8 wt% Cr) under simultaneous corrosion by flowing LBE (350 °C) also showed increased corrosion layer thicknesses in the beam spot (150, 151). AISI 316L and T91 samples exposed to LBE (350 °C) and neutron-irradiated up to 9.1 dpa in the BOR-60 reactor showed a sub-μm oxide layer, but no evidence of large-scale corrosion attack (152). Differences exist in the interpretation of whether radiation-induced defects are responsible for accelerated corrosion (148–150) or simply beam-induced temperature differences (145–147), and as of yet, there is no conclusive proof for which is the dominant cause.

3.6. Studying irradiation-corrosion interactions

3.6.1. Validity of ion irradiation studies in a nuclear reactor context

Since most of the displacement damage in materials is caused by neutrons, using a reactor to study their effects under realistic fluxes would be ideal. However, such experiments are rather costly and time-consuming since a commercial reactor only produces a few dpa per year (up to 10 dpa in a high-flux reactor). If the goal is to study the behavior of a material after long-term exposure, e.g., towards the end of life of the reactor, suitable ways to conduct accelerated aging studies must be found. This is especially true for studies targeting advanced reactors, where materials may experience hundreds of dpa over their lifetime and where access to research reactors is limited at best. In addition, neutron irradiation produces many TPs in a material, which makes the samples highly radioactive and difficult to handle.

All these factors make ion irradiations very attractive as surrogates for neutron irradiation. This is reflected in the approximate number of irradiation-corrosion studies employing each

radiation type shown in Figure 7. Note that there is a large number of in-reactor studies, but that many of them are significantly older than those published using ions. However, there are some fundamental differences between damage induced by neutrons and by ions. Unlike neutrons, ions have an inhomogeneous damage profile. A flat damage region that becomes larger as the ion energy increases is followed by the Bragg peak, where substantial damage is created in a small region. Shortly thereafter, the ion comes to rest in the material, leaving behind an injected atom. The length of the ion track is quite limited compared to that of a neutron of comparable energy, which limits the depth in the material that can be studied. Like neutrons, light ions can produce a variety of TPs at relatively low ion energies, while heavy ions do not. The species produced from ion irradiation are different, which implies that the impact of TPs on the sample cannot be directly compared to those created by neutrons. However, their number is smaller due to smaller reaction cross sections compared to neutrons, which renders the material less activated. Ion beams can induce up to several dpa per day (depending on the ion and the flux), which accelerates the study of high-dose radiation effects, and has been shown to be a useful surrogate for neutron damage if dose rate and other effects are interpreted carefully (153). Light ions are useful because they have much greater penetration depths than heavy ions. Consequently, the flat damage profile of a proton with a few MeV of energy can extend 10s of μm deep into a material. An in-depth discussion of neutron damage effects that can be emulated by ion irradiation in various ways is given in (123).

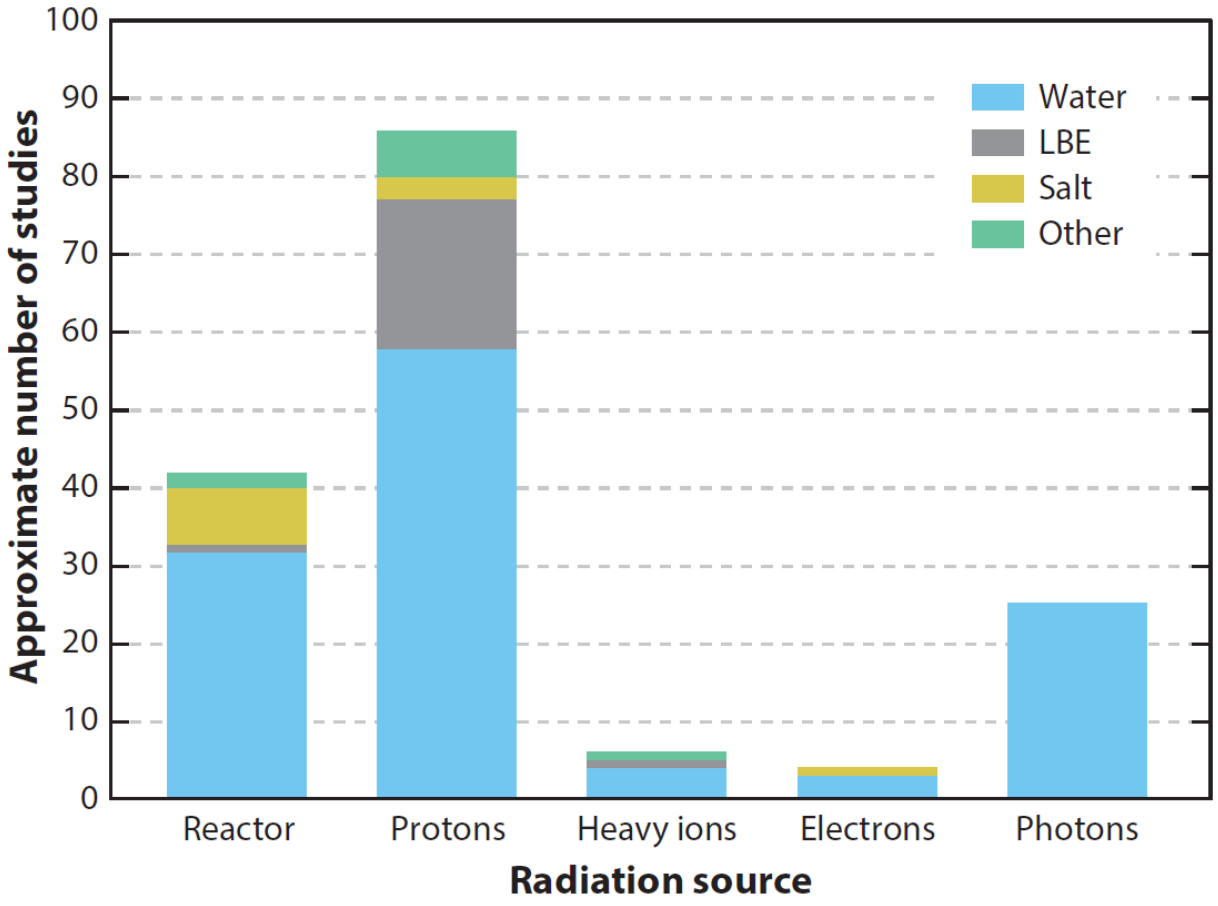

Figure 7 – Approximate number of simultaneous irradiation-corrosion studies reported in the literature as of 2021, adapted from (26). Note that the list of studies counted here is not exhaustive and is merely intended to give an overview of the field of simultaneous irradiation and corrosion.

3.6.2. Importance of laboratory-scale irradiation-corrosion experiments

In many cases of undesirable materials degradation, a set of very specific conditions is responsible for increases in the susceptibility of the alloy. Determining these conditions in materials exposed to simultaneous irradiation and corrosion is the main purpose of laboratory-scale irradiation-corrosion experiments. Another purpose of these experiments is to predict the end-of-life of components, even in ideal conditions. One example is determining when the cladding reaches a certain oxide thickness above which heat transfer deteriorates to an unacceptable level. In some cases, there is doubt that a short-term experiment can reproduce the often-long-term responses of materials to certain conditions. Therefore, such experiments must accelerate irradiation and corrosion processes in a material equally or at least in a representative manner if any useful information about their simultaneous occurrence is to be gained. Even though laboratory experiments are generally easier to control, care must be taken to keep track of the various environmental parameters. For example, the presence of impurities in the system can make results of irradiation-corrosion experiments difficult to interpret (see, e.g., (154)).

Certain in-reactor phenomena, such as BWR nodular corrosion and shadow corrosion in Zircaloy-2, are difficult to simulate outside of a reactor, although shadow corrosion has recently been reproduced in a laboratory setting (155). Their likely galvanic nature requires simultaneous irradiation of the material, which leads to increased electrical conductivity of the oxide layer, and sufficient dissolved O in the water to change the electrochemical potentials of the surrounding metals for these processes to occur (113, 122). Therefore, while much can be learned from irradiation experiments with pre-oxidized samples, certain processes require simultaneous irradiation and corrosion.

For LFRs, where corrosion is currently not considered to be life-limiting, the relevance in understanding irradiation-corrosion interactions lies in preventing 1) the acceleration of corrosion processes to the extent that they become life-limiting for a component, and in preventing 2) the synergistic acceleration of the redistribution of alloying elements in such a way that LME or void swelling (in components where it is critical) are enhanced locally.

3.6.3. Setups for simultaneous irradiation-corrosion experiments with lead-bismuth eutectic (LBE) reported in the literature

This section mainly describes experiments that use ion beams as their source of radiation damage rather than neutrons. An in-depth report of the work that has been done in HLM environments can be found in (21). This section only describes the experimental designs. Results are briefly discussed in Section 3.5.1.8.

The original experiment in the ICE series, ICE I, is described in (156) and served as a demonstration experiment. The second version, ICE II, is described in (157) and produced an HT-9 sample (a F/M steel, 12Cr-1MoVW), which was corroded in LBE (420 °C) and simultaneously irradiated with 5.5 MeV protons for 58 hours (148), and whose evaluation will be described in Section 4.1. ICE II was a quasi-static corrosion chamber setup, where the LBE could be drained from the chamber and replenished periodically. The purpose of this was to enable dissolved O control in the chamber-external LBE reservoir and the exchange of LBE in the chamber to maintain an oxide-forming environment. The chamber was connected to a 3 MV National Electrostatics Corporation (NEC) Tandem accelerator at the Ion Beam Materials Laboratory (IBML) at Los Alamos National Laboratory (LANL).

The sample itself was used as the beam window, and therefore had to withstand high-vacuum conditions (as low as 1e-6 Pa). High-energy protons were supposed to fully penetrate the sample

to then be stopped in the LBE behind it. This creates a zone on the backside of the sample where irradiation and corrosion occur simultaneously. The ~5 cm diameter sample was dimpled to achieve a variety of thicknesses between 77 µm in the center and 110 µm at the edge of the dimple. The original intent was to create different zones with different dpa levels, depending on which part of the Bragg curve the solid-liquid interface would coincide with (157).

A static irradiation-corrosion setup, which is conceptually similar to the static corrosion cells described in (142) and in this work, was established at a 3 MV tandetron accelerator at Sichuan University (149). The limitations relevant to sample thickness are similar to those relevant to the setup presented here and discussed in Section 4.2.1 although a higher proton energy of 5 MeV and therefore a higher sample thickness of 70 µm was selected in (149). The setup also features a thermal camera that measures the sample temperature on the vacuum side.

Several experiments with higher proton energies have been designed to study irradiation-corrosion effects in LBE for ADS applications. The spallation targets for these systems will be bombarded with protons with several hundred MeV of energy and have been studied as part of the MEGAwatt PIlot Experiment (MEGAPIE) (158, 159), the Development and assessment of structural materials and heavy liquid Metal technologies for TRAnsmutation (DEMETRA) systems (160), and the GEneration IV and Transmutation MATerial (GETMAT) (161) programs. The goal of MEGAPIE was to develop an LBE spallation target with T91 as the beam window material (162, 163). To this end, stressed steel specimens were exposed to 72 MeV protons and flowing LBE in the Liquid metal – Solid metal Reaction (LiSoR) loop (see (164)) up to less than 1 dpa.

Few facilities work with heavy ions because of the higher energies that are needed to achieve the same penetration in the samples as with light ions. One such example is the Heavy Liquid Metal and Irradiation Facility (HLMIF), where 247 MeV Ar ions are used to study interactions between LBE corrosion and heavy ion irradiation (150). The isothermal flow loop can circulate LBE at flow velocities of up to 3 m/s at different temperatures (200-600 °C) and with a dissolved O concentration that is assumed to be at saturation (150). The ion energy limits sample thicknesses to 30 µm or lower.

A major drawback of the setups described in this section is that results can only be obtained by analyzing the samples "post mortem". One attempt to study the irradiation-corrosion response of pre-oxidized HT-9 irradiated with 800 MeV protons and exposed to static LBE (200 °C) in situ was made with a method similar to electrical impedance spectroscopy at the Los Alamos Neutron Science CEnter (LANSCE) (165). As expected from observations in aqueous environments, the oxide's impedance immediately decreased with beam on the sample, but fluctuated wildly once the beam was turned off, which reflects difficulties with repassivation (165). The addition of an in-situ monitoring capability for corrosion under irradiation is one of the goals of the ICE III presented in this dissertation and will be discussed in Section 4.3.

3.6.4. Need for understanding of model materials

While the ultimate goal is to develop better structural materials for nuclear environments, understanding the intricacies of materials degradation in a complex alloy is typically extremely complicated. To reduce the parameter space, it is often helpful to simplify the composition and study pure, binary, or ternary model alloys. If the correct alloying species are chosen, it is possible to achieve a good approximation of the commercial alloy's behavior. There have been several successful realizations of this approach in irradiation effects studies. For example, the influence of Ni content on neutron-induced void swelling in model and commercial alloys has been found to

be similar in both reactor and ion beam studies (166). Other studies have shown that simple FeCr binary alloys exhibit similar void swelling behavior as FeCrNi alloys (167, 168). Fe15Cr45Ni doped with ^{59}Ni shows levels of He production at low dpa that are typically only observable after some delay due to the required buildup of ^{59}Ni (169). This information directly led to a better understanding of which (n,α) reactions dominate He production in a fast reactor environment. The same logic should apply to using model materials in irradiation-corrosion experiments.

4. Irradiation-corrosion experiments

ICE III, which is described in Section 4.2, is the third installment in a series of experiments targeting the effects of radiation on simultaneous corrosion processes in LBE. Its predecessor, ICE II, which is described in Section 3.6.3, produced an HT-9 sample, the analysis of which will be discussed in Section 4.1. ICE III is not only simpler than the previous iterations in its overall design, but it also features a new in situ sample surveillance technique in the form of PIXE, which is normally used for the elemental analysis of thin samples. This feature is described in Section 4.3 and in situ as well as ex situ results obtained in the pure Fe-LBE model system are described in Section 4.4. In Section 4.5, some preliminary results from using ICE III with molten salt (MS-ICE) and attempting to introduce thin-films grown with physical vapor deposition (PVD) into an ICE-like design (Tiny-ICE) are shown. Finally, a discussion of the implications of the different experimental observations is discussed in the context of the literature in Section 5. Table 4 summarizes the different combinations of sample materials, corrosive environments, and proton energies discussed in this section.

Table 4 – Summary of experiments discussed in this section.

	Sample material	**Corrosive medium**	**Temperature [°C]**	**H^+ energy [MeV]**
ICE II	HT-9	LBE	450	5.5
ICE III	Fe	LBE	450	4
MS-ICE	AISI 304	NaCl-$MgCl_2$	450	2.75
Tiny-ICE	Fe	LBE	450	0.2

4.1. HT-9 sample evaluation from the irradiation-corrosion experiment II

As mentioned in Section 3.5.1.8, an inhomogeneous oxide had previously been observed on this sample (148). However, this was based solely on the analysis of the sample surface. The goal of the work presented in this section was to study the cross section to find evidence of radiation-induced changes to the oxide layer, specifically its overall thickness. The expectation was to find a thicker oxide layer in the beam spot as had been observed in other irradiation-corrosion studies (see Section 3.5.1.8).

4.1.1. Procedure

This work was performed in 2019 at the University of California, Berkeley (UCB), seven years after the ICE II run in 2012. The sample was still slightly activated and contaminated with LBE (see Figure 8b)). It was cut near the beam spot on a slow-speed saw, which was supposed to prevent excessive damage to the oxide layer. The sample was then cast in epoxy to further stabilize it, especially in the center, which had developed a leak during the experiment and was already reinforced with Crystalbond (Ted Pella). Polishing was done on a portable polisher to prevent contamination of shared polishers. Ethanol was used as lubricant to prevent any water-based corrosion of the oxide during polishing. The sample was polished to 2000 grit. The thickness of the remaining uncorroded steel as well as the adherent oxide layer were then measured in a scanning electron microscope (SEM, FEI QUANTA 3D dual beam SEM/FIB (focused ion beam, UCB)).

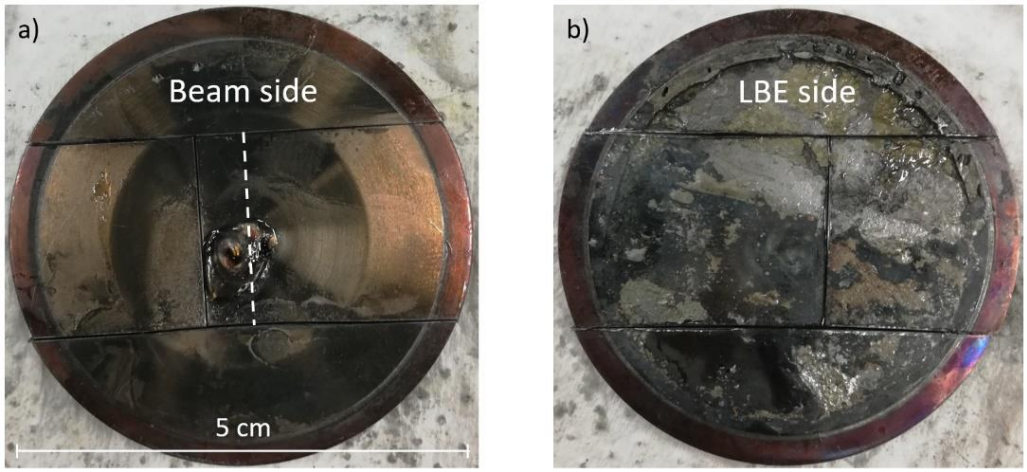

Figure 8 – ICE II sample after cutting. The white line in a) roughly indicates the depth to which the sample was polished.

4.1.2. Results

An SEM image was taken every 500 µm and every 250 µm near the center and the thicknesses of the base metal and the observed oxide were measured (see Figure 9). For these measurements, the oxide layer thickness is a single number, even though in some areas, the oxide shows the characteristic multilayer structure expected for a F/M steel in LBE (see Figure 10). It is immediately apparent that the center of the sample is thicker (~83 µm) than it was supposed to be (77 µm, (157)). It is also obvious that the remaining oxide layer is thickest in a region away from the center. The outlier close to the middle of the oxide thickness peak is due to the oxide being partially spalled off in this location. It could be corrected upward by adding the observed thickness of the outer missing oxide in neighboring locations (see Figure 10 b)), but this was not done for this figure because of the high variability observed in outer oxide thicknesses.

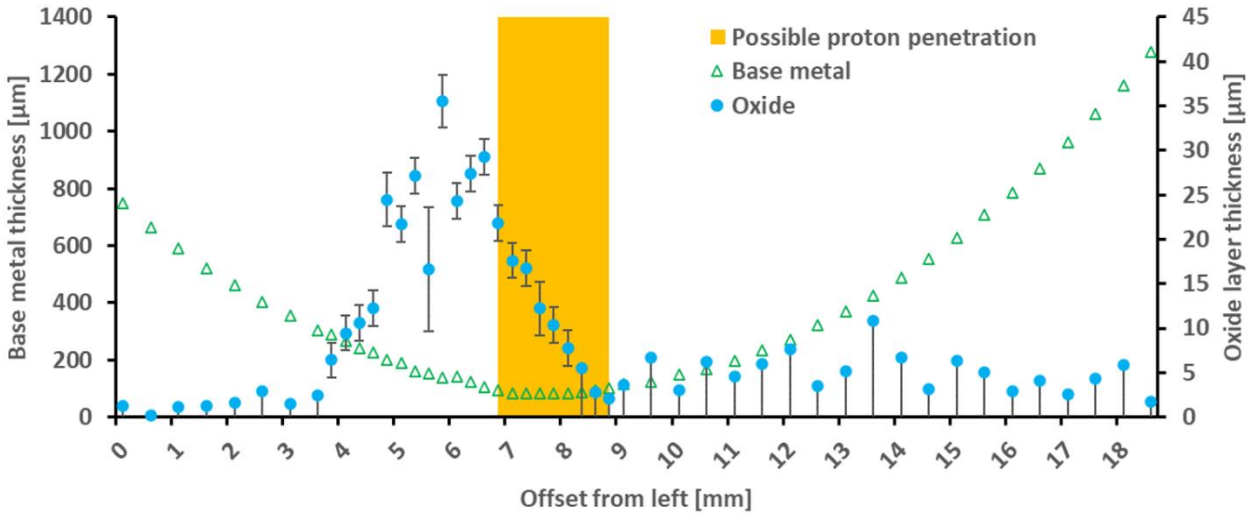

Figure 9 – ICE II sample cross section measurements.

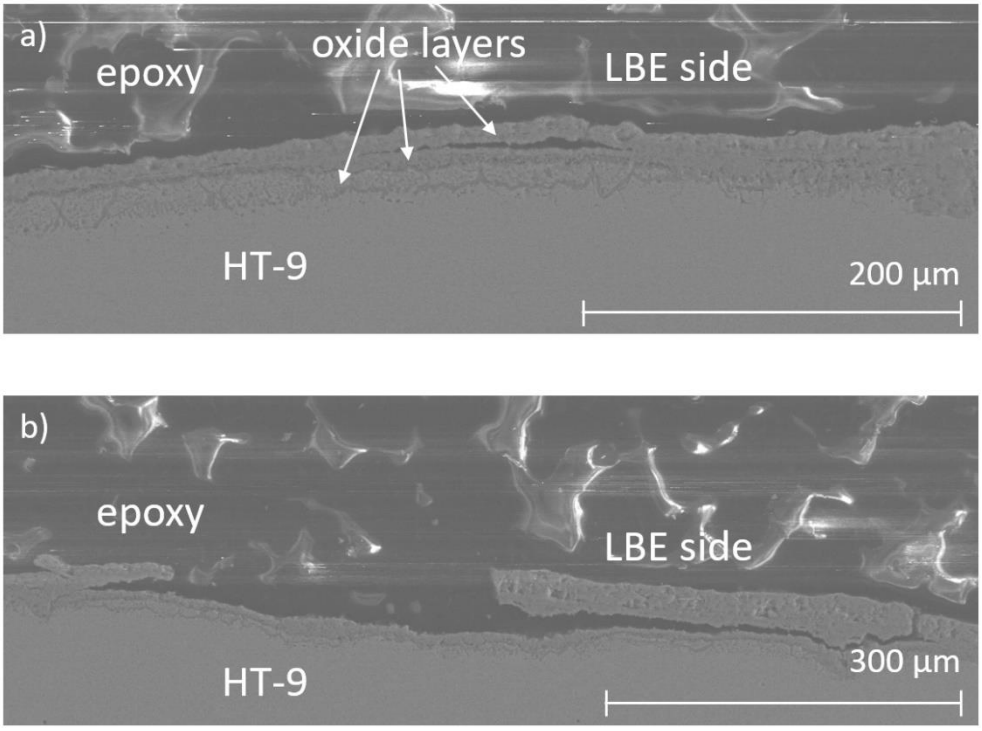

Figure 10 –Multilayer structure of oxides that formed on the ICE II sample and partially spalled off.

4.1.3. Discussion

As noted in Section 3.6.3, the ICE II sample was dimpled, which led to a range of thicknesses between 77 µm in the center and 110 µm at the edge (157). For the 5.5 MeV proton energy that was selected for the experiment, this means that the center of the dimple would be part of the flat region of the Bragg curve, while the peak occurs around 98 µm and the curve ends at approximately 105 µm (see SRIM calculations in (157) and Figure 11). Therefore, 5.5 MeV protons cannot fully penetrate the outer edge of the dimple.

The base metal was measured to be ~83 µm at its thinnest in this work, which either implies that the sample was not 77 µm thick to begin with, which is difficult to control during machining, or that this cross section is slightly off-center. However, in either case, it is interesting to note that the oxide is thickest far away (~1.5 mm) from the center. More importantly, its thickness peak is located well outside the region of possible proton penetration, which is shown in yellow in Figure 9. This region corresponds to the area of the sample where the base metal is currently 105 µm thick or less. However, the HT-9 metal thickness has decreased over the course of the experiment due to the growth of the oxide layer, which means that the region the beam could penetrate was even narrower at the start of the experiment.

The beam spot size during the experiment was reported to be 3x3 mm^2 (157). If the beam was centered on the sample, the oxide thickness peak barely overlaps with the beam spot. It is possible that the beam was slightly off center and coincides with the oxide thickness peak, especially for an experiment that lasted almost 60 hours. However, in this case, the beam spot would have been in an area where the protons cannot fully penetrate the metal, and therefore cannot produce defects at the metal-liquid interface or the oxide-liquid interface directly to accelerate corrosion as hypothesized.

This leaves several possible explanations for the observed oxide thickness peak:

1) It is possible that the oxide in the center of the sample spalled off. The stresses that occur in thick oxides eventually cause spalling, and it is conceivable that radiation-accelerated corrosion led to an accelerated thickening of the oxide in the center, such that it broke off, while the oxide in other areas of the sample is still intact. However, it is not clear why only the oxide on one side of the beam spot and in one highly localized area would have survived and why there is a clear peaking of oxide thicknesses.
2) A beam of 5.5 MeV H^+ at the reported average 2.7 µA deposits ~15 W in the beam spot. As will be seen in Section 4.4, this leads to substantial heating in the beam spot (10s of °C), even with a coolant as efficient as LBE. It is possible that beam heating contributed to the observed accelerated oxide growth.
3) It is also possible that radiation-induced defects have traveled a significant distance through the sample to contribute to accelerated corrosion at the solid-liquid interface. This requires their migration through several tens of µm of material – likely primarily along GBs – which is not inconceivable.

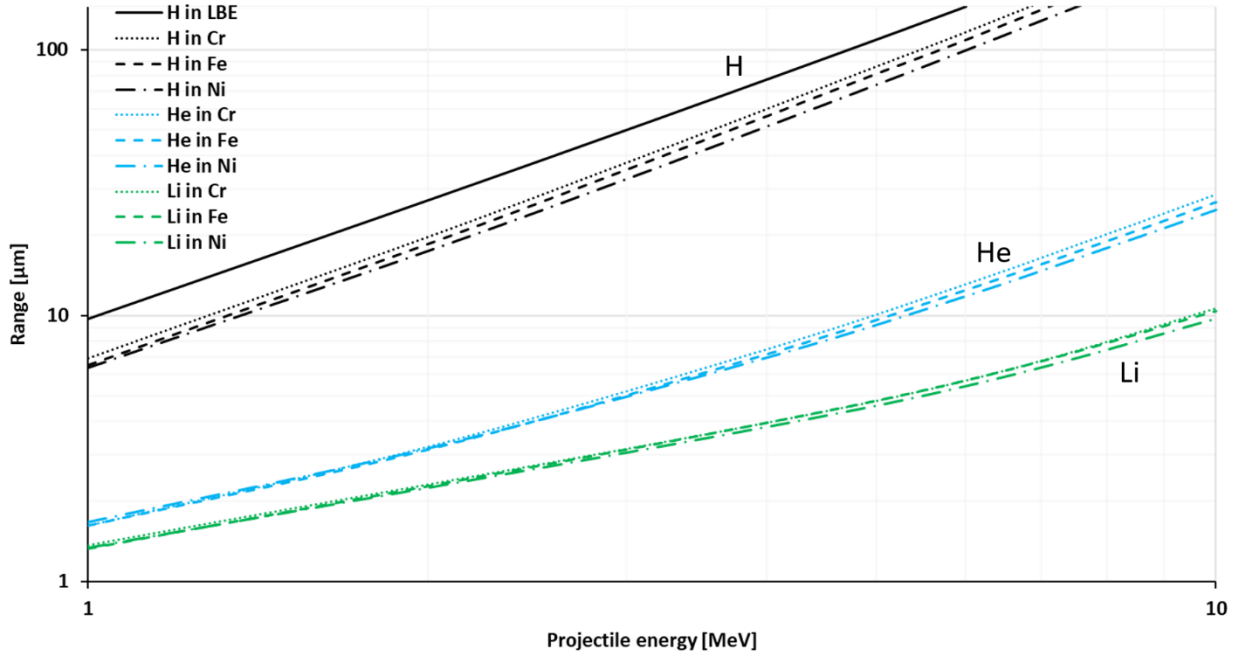

Figure 11 – Log-log plot of estimated ion ranges for H, He, and Li in Cr, Fe, and Ni, as well as for H in LBE. The curves were obtained with SRIM (170) Quick Calculations with effective displacement thresholds from (171) and lattice displacement thresholds set to 0 eV, according to (172).

4.2. Development of the simultaneous Irradiation-Corrosion Experiment (ICE) III

ICE III differs from its predecessor, ICE II, in several ways that will be outlined in this section. The two primary differences are that ICE III uses thinner samples (≤ 50 µm), which reduces sample activation because lower-energy protons (≤ 4 MeV) can be used, and that it is a static corrosion chamber, i.e., no corrosive medium can be added or removed during the experiment, which greatly simplifies the design. In addition, it features an in-situ corrosion monitoring technique in the form of PIXE, which will be described in Section 4.3.

4.2.1. Chamber design

4.2.1.1. Design requirements

Several design goals had to be fulfilled with ICE III:

1) Simplicity: The new design should be simple and, ideally, only use off-the-shelf parts.
2) Experiment duration: ICE III samples are supposed to last up to 200 hours under irradiation-corrosion conditions, which requires that the corrosive liquid maintain its corrosivity for the same duration.
3) Fast turnaround: While being thick enough to last for up to 200 hours, the samples should also be thin enough for the proton beam to pass through (see next paragraph). The thinner the samples, the lower the proton energy, which reduces activation and the production of radioactive isotopes.
4) Space for attachments: ICE III is intended to have access ports for multiple thermocouples (TCs) as well as electrodes.
5) Compatibility / adaptability: ICE III is intended for use with any liquid corrosive medium, i.e., its fundamental design should be compatible with or easily adaptable for other corrosive media beyond LBE, such as molten salts.

Design goal 3) is only relevant if the sample itself is the beam window. Since ICE III is designed for use with a relatively low-energy proton beam (< 10 MeV), the only options for an irradiation-corrosion experiment are a) to use the sample as the beam window and have the protons be stopped in the corrosive medium or, alternatively, b) to have the protons pass through a window and the liquid to then be stopped in the sample. The latter requires an extremely thin window, which is also likely to be corroded, but, more importantly, an extremely thin layer of liquid as well. The penetration depth for protons of different energies is shown in Figure 11. The maximum proton energy the 3 MV NEC Tandem Accelerator – used during ICE II as well as ICE III – can produce is 6 MeV, according to

$$E_{ion} = (q + 1) * \Delta U \, ,$$

where q is the charge state of the ion (+1 for protons) and ΔU is the accelerating voltage. 6 MeV protons can penetrate approximately 150 µm of LBE. This means that the corrosive medium volume would be extremely small and could saturate quickly with corrosion products during the experiment, at which point the corrosion process ends. Another issue specific to LBE is that the protons would pass through it at high energies, which could lead to the production of Po. For these reasons, while setups for option b) exist (see, e.g., a chamber that can be used in electron microscopes (173)), for our purposes, the sample must be the beam window and the irradiation-corrosion region is on the backside of the foil, where the corrosive medium is located.

4.2.1.2. Sample requirements

As the beam window, the sample must be able to make a vacuum-tight seal and withstand the pressure difference between the corrosion chamber and the vacuum. Metals are good sample candidates due to their ductility, while brittle materials, such as ceramics, are more difficult to mount on the chamber and would likely break if too much pressure is applied to create a vacuum seal. Another requirement is that the sample should not react rapidly with the chamber materials it is in contact with or with the corrosive medium. In the case of LBE, this means avoiding samples

that primarily consist of highly soluble elements (see Section 3.2.1). The pure sample materials of interest for the study of structural steels are Fe, Cr, and Ni. Since Ni and Cr have relatively high solubility in LBE, pure Fe was selected.

In addition to the range of protons, Figure 11 also shows the penetration depths of He and Li ions in Fe, Cr, and Ni. It is immediately obvious that ions heavier than protons have very shallow ranges in these materials (9 MeV He^{2+} ions stop after less than 25 μm), which makes them unsuitable. It is also important to note that the sample should be substantially thinner than the ion range, so that the interface between the sample and the corrosive medium does not coincide with the Bragg peak. As the interface moves during the corrosion process, the applied dose rate should ideally stay the same. Therefore, it is desirable to set the sample thickness such that it only overlaps with the flat region of the stopping power curve. Considering all these factors, the maximum proton energy for ICE III was set to 4 MeV, which allows the use of samples up to 50 μm thick.

4.2.1.3. Early iterations

Different options for the design of ICE III and its components were discussed with Peter Hosemann and others. High-vacuum-compatible DN16CF flanges (Duniway and MDC) were selected as the building blocks of ICE III. Larger flanges can hold more liquid, but with the reduction of the sample thickness to 50 μm, there were concerns that the sample might rupture during the experiment like the HT-9 sample in ICE II, especially if it is made of less corrosion-resistant pure Fe. A DN16CF flange allows for a sample diameter of ~2 cm, which makes the sample more stable than a larger size. However, the reduced diameter leads to concerns about premature saturation of the LBE with corrosion products or a decline in dissolved O concentration over the course of the experiment. Therefore, a thick version (~1.3 cm wide compared to the usual 0.7 cm, Norcal) of the DN16CF was used to contain the corrosive medium.

TCs (1/16" OD sheathed K-type, Omega) were added to the chambers by feeding them through a Swagelok adapter from a 1/16" to a 1/16" male NPT (National Pipe Thread) connector (AISI 316, from Stainless Steel Fittings). AJ Gubser (UCB) drilled and tapped the necessary NPT holes on the central flange. A typical chamber has two NPT fittings, so that two TCs – one in the beam spot, one outside – can be added. Initially, the threads were going to be welded shut to prevent LBE from escaping the chamber. However, due to its very low vapor pressure this proved to be unnecessary as there has been no evidence of Pb or Bi vapor leaving the chamber. An attempt to seal the threads with high-temperature compatible liquid Copaltite sealant (up to 815 °C, Copaltite) was made, but the LBE interacted with it and its use was discontinued to prevent LBE contamination.

Originally, the chamber was going to feature a window on the backend of the chamber, through which the corrosive medium could be studied, for example with Raman spectroscopy. This would be especially useful for transparent corrosive media, where it might be possible to study the backside of the sample during the corrosion process. Early tests with LiCl-KCl eutectic (58.8–41.2 mol%, T_{melt} 352 °C, synthesized by Jie Qiu (UCB)) showed some promise, as the sample could be viewed through a sapphire window (Larson Electronic Glass) while the salt was molten (see Figure 12 d)) although some opaque corrosion products also deposited on the window. Since this was a mechanical test, no particular care was taken to keep the salt clean. After synthesis, the solid salt block had to be ground into a powder to be filled into the test chamber. Grinding was done in a Spex Shatterbox® with the help of John Grimsich and Tim Teague (UCB). The grinding and filling of the salt into the chamber was done outside of a glovebox, which is likely how impurities were introduced. There may also be a minor contribution from interactions of the salt

with the native oxide on the chamber parts. Exclusively handling the salt in an inert atmosphere, e.g., in a glove box, and more rigorous chamber preparation, e.g., by flushing it several times with clean salt, could probably avoid these depositions on the window. However, no further attempts were made because the sapphire window is Ag-brazed to the flange, which limits its use to 200 °C (174). During testing, it stayed intact at temperatures up to 400 °C for 40 hours, but since the experimental duration for ICE III was intended to be much longer (up to 200 hours) and at higher temperatures (up to 700 °C), especially for molten salts, it was removed from the chamber. For LBE, a Ag-brazed window is not suitable to begin with because Ag has very high solubility in LBE.

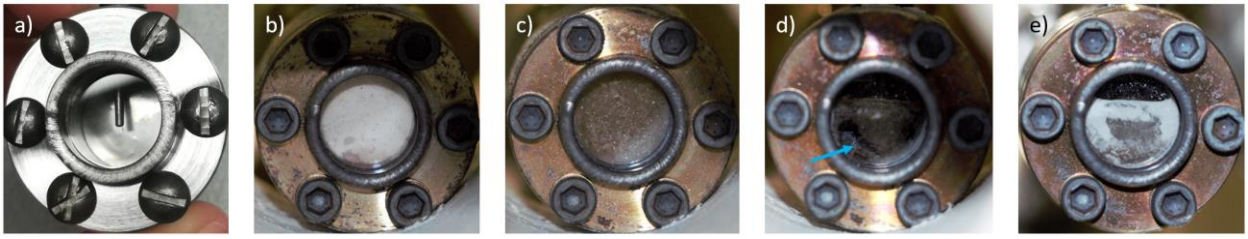

Figure 12 – Test of the sapphire window with LiCl-KCl (40 hrs at 400 °C) and a AISI 304 sample (Maudlin Products). a) shows the empty chamber through the window where the TC is visible; b) is the chamber filled with salt powder; c) and d) show the salt partially and fully molten; respectively. The blue arrow points to an area where the backside of the sample is visible through the salt, while the rest is covered with opaque corrosion products; e) shows the chamber after the experiment, where the deposit is clearly visible. Note that the salt volume has decreased due to the powder's low packing fraction.

Initially, it was not clear how to mount the sample to create a vacuum-tight seal. Different options were explored, such as pressing the sample directly against the knife edge of the corrosion chamber with a gasket, sandwiching the sample between two gaskets, and welded solutions. In the case of LBE, traditional gasket materials, such as Cu and Ni, must not be exposed to the LBE because of the high solubility of these elements. Therefore, any kind of sample sandwich would require an LBE-compatible material, such as graphite. Having the sample between the gasket and the knife edge allows for the use of traditional metal gaskets, but there were concerns that the sample would be cut through, which might allow LBE to get in contact with the gasket. Several "dry" tests, where samples were mounted and inspected, as well as long-term corrosion tests (up to 200 hours) showed that this was not the case for 50 μm thick steel and Fe foils, so this method ended up being selected.

This also meant that a second sample could be used on the backside of the chamber to protect the gasket and to obtain a comparison between the irradiation-corrosion sample and this new corrosion-only sample. Had this mounting method not worked, the alternative strategy would have been to use a disk of soft graphite instead. However, attempts at making a Cu-sample-graphite sandwich generally resulted in the graphite being compressed too much and small amounts of LBE leaking into neighboring flanges. The graphite sheet was also difficult to work with due to its softness, which may have been alleviated by replacing it with steel-reinforced graphite sheet.

Finally, a welding solution would have required a weldable surface of some kind, which would have led to more modifications to the chamber flanges. One possible option for molten salts was explored, where a pure Ni sample was held between two Ni gaskets that were then welded together on the outside. This work was performed by Adi Ben Artzy (UCB) and Rasheed Auguste (UCB). Since pressing the sample against the knife edge was sufficient and Ni is not compatible with LBE, this beam window was never used, but was a valuable proof of concept for potential molten salt designs.

4.2.1.4. Current design

The various choices described in the previous section led to the current design shown in Figure 13. All flanges are made from AISI 304 and available off-the-shelf. Drilling and tapping of holes for the Swagelok adapters (AISI 316) is the only modification necessary. Since all experiments discussed here are conducted at relatively low temperatures (450 °C), Cu gaskets are used to hold the samples in place even though they are known to diffusion-bond to other metals around that temperature. Ni gaskets are available for higher-temperature experiments. Sample A is the beam-facing irradiation-corrosion sample, while Sample B is the corrosion-only sample on the backside of the chamber. Two K-type TCs (positive lead: Ni-Cr, negative lead: Ni-Al; sheath: AISI 304L) are bent towards the two samples, so that TC A records temperatures near the beam spot and TC B records temperatures near the backside of the chamber. The assembly is mounted on a DN40CF-to-DN16CF adapter flange, which is mounted on one of the beamline end stations of the 3 MV NEC Tandem accelerator at the IBML at LANL.

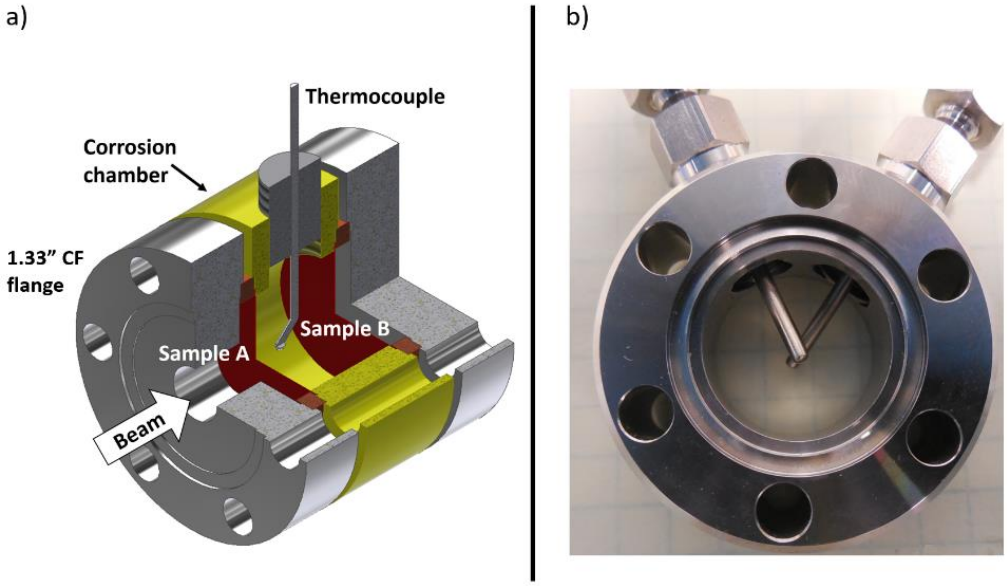

Figure 13 – a) shows the layout of the ICE chamber with two samples (irradiation-corrosion (Sample A) and corrosion-only (Sample B); red areas) and one TC in the corrosion chamber (yellow center flange). b) shows a photo of an empty ICE chamber with two TCs, which are bent away from each other to be closer to the sample surfaces.

4.2.2. Samples

Testing of the ICE III chambers was done with 50 µm of AISI 316 (Maudlin Products) or 99.5% pure Fe (Goodfellow), while 99.99% pure Fe (Goodfellow) was used for the actual experiments. 99.8% pure Fe (Goodfellow) was used for the PIXE calibration curve measurements (see Section 4.3.3). Table 5 shows the impurity contents according to data sheets provided by the manufacturer (175). Note that the absence of values for a particular impurity concentration does not necessarily imply that it is below the detection limit, but rather that it likely was not measured, especially in the case of 99.5% pure Fe. Samples were used in as-rolled condition, i.e., there were no polishing or annealing steps, which could be added if desired. After cutting, the samples were cleaned with isopropanol and mounted in the chamber.

Table 5 – Impurity content of pure Fe from Goodfellow in ppm.

	Mn	Cu	Ni	Al	Si	In	Ag	Ca	Co	Mg	Cr	P	S
99.5%	3000	-	-	-	1000	-	-	-	-	-	-	<400	<500
99.8%	5	400	400	10	8	8	15	40	400	8	-	-	-
99.99%	1	2	1	2	3	-	1	3	-	2	1	-	-

4.2.2.1. Sample cutting

Since the samples are rather thin, they can be cut with scissors if a simple circular shape is sufficient. Early test samples were cut this way and were found to work well. However, there were a few exceptions that led to small leaks during testing, which was typically because the sample OD was slightly too large. Consequently, the gasket could not create a proper seal with the knife edge. In order to avoid this and reduce potential stresses introduced by hand-cutting, more reproducible machine-based cutting methods were sought, such as water jet cutting, wire electrical discharge machining, or laser cutting.

Attempts with water jet cutting were made at the Jacobs Hall Makerspace (UCB) under the guidance of Cody Glen (UCB). Several pieces of 99.5% Fe foil were stacked and sandwiched between two thin Al pieces. The stack was clamped together, stabilized with glue, and cut on an Omax water jet using garnet as the abrasive. Unfortunately, the water jet produced very jagged edges on the samples (see Figure 14), presumably due to vibrations during the cutting process. This also allowed water to penetrate in between samples and oxidize them because pure Fe promptly reacts with water.

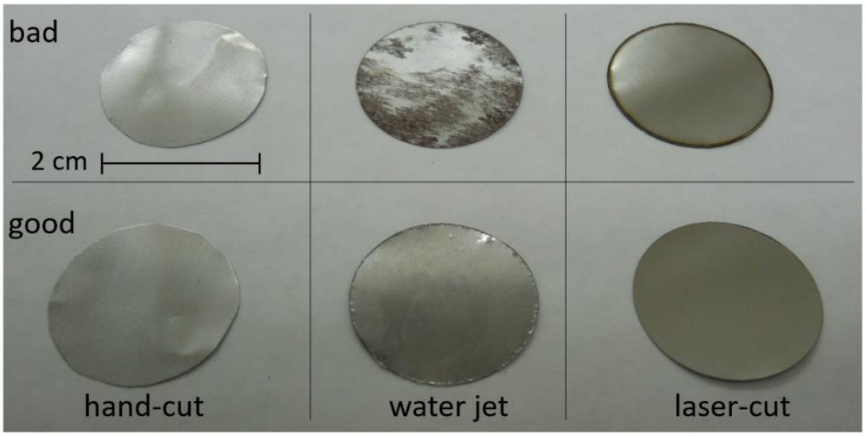

Figure 14 – Comparison of good and bad examples samples cut by hand, with a water jet, and with a femtosecond laser.

Of the machine-based cutting methods mentioned above, laser cutting is the only one without a potentially corrosive cutting fluid. It also allows for the cutting of more complicated shapes, such as the one shown in Figure 15, unlike hand cutting. This sample type was cut with the femtosecond laser at the Center for Integrated NanoTechnologies (CINT, LANL) with the help of Quinn McCulloch (LANL), who, together with Jonathan Gigax (LANL), also provided training on the femtosecond laser. The bolt hole cutouts can keep the sample in place if it is sandwiched between two gaskets, as described in Section 4.2.1.3. However, since a single gasket turned out to be sufficient, these samples were never used. Instead, simple circles were cut, as shown in Figure 14. Laser cutting produces the cleanest and most consistent samples. The dark rim of the bad example was produced by too much laser power. When used properly, this technique puts little stress on

the sample and has a small heat-affected zone, which means that the LBE-facing area inside the knife edge should be unaffected by the cutting process.

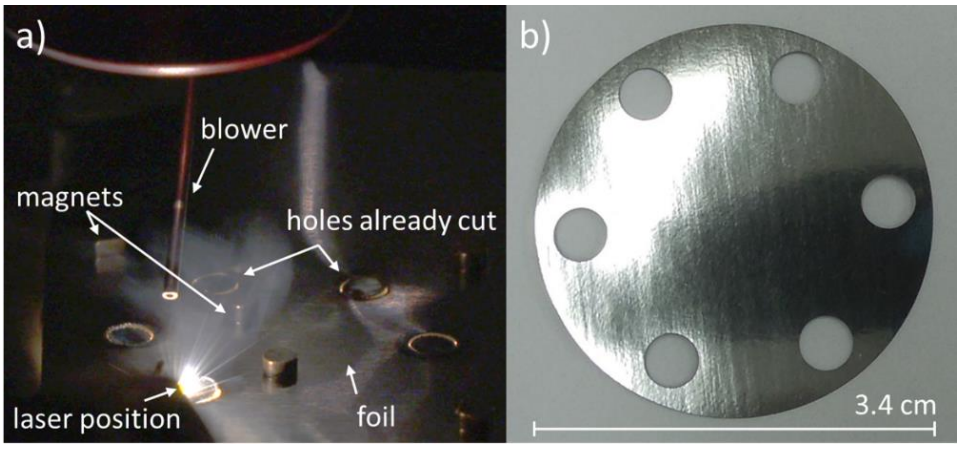

Figure 15 – a) A 99.99% Fe foil (Goodfellow) is being cut at the fs-laser at CINT (photo courtesy of Howard Coe (LANL)). Magnets hold the foil in place as the XYZ-stage moves the foil underneath the laser. A blower directed at the laser spot removes debris during the cut. b) A finished Fe foil with bolt holes cut out.

4.2.2.2. Thin-films

An attempt was made to grow thin-films on AISI 316 and pure Fe substrate. Unlike a regular 50 μm thick sample, a thin-film can only be used for a short-term corrosion experiment. However, if thin-films could be incorporated in ICE III, then a variety of different sample compositions could be tested easily. The goal was to determine if Fe or steel foils could be used as a mechanically stable beam window, so that other, possibly less stable alloy compositions could simply be grown on top and used in ICE III. In preparation, 50 μm thick AISI 316 and pure Fe foils (2 cm OD) were electropolished with 5 vol% perchloric acid in methanol by Ramon Martinez (LANL) and Hyosim Kim (LANL) based on a recipe provided by Calvin Lear (LANL). 1 μm thick Fe thin-films were then PVD-deposited (room temperature, 10 W bias) by Ben Derby (LANL). Unfortunately, these samples were never used in ICE III because clamping them between a gasket and the knife edge immediately introduced cracks in the films (see Figure 16). Such cracks would likely allow the LBE to penetrate underneath the thin-film immediately and would probably cause the film to be lifted off the substrate very quickly.

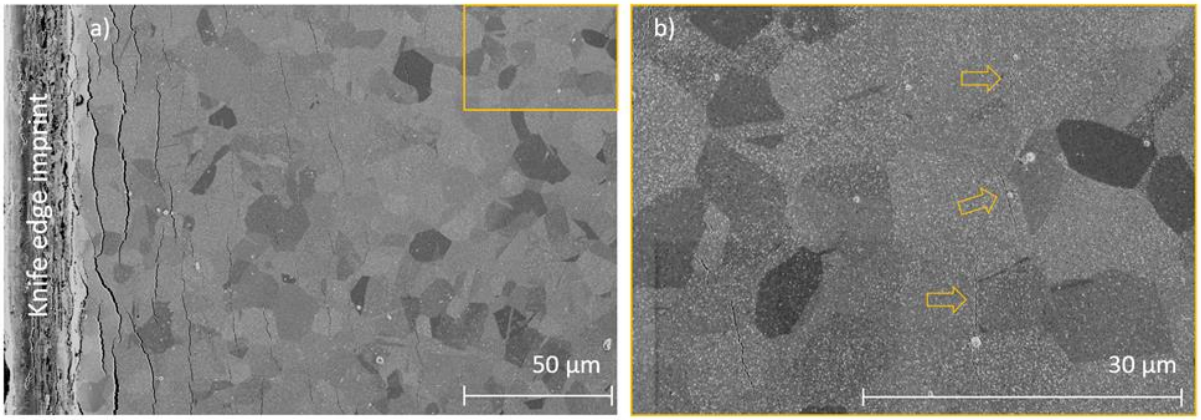

Figure 16 – a) shows cracks parallel to the knife edge that are visible at very low magnification. The cracks become finer the further they are from the knife edge, as shown in the magnified cutaway in b).

It is unclear if adhesiveness of the film can be improved or if growing a film only in the center of the sample would alleviate this issue without the outer rim of the thin-film experiencing accelerated attack.

4.2.3. Chamber filling

4.2.3.1. Pb safety

Filling of the corrosion chambers requires hands-on work with LBE, which is ~45% Pb, an element known to be toxic. Safe handling procedures were developed in the context of an integrated work document for experiments involving LBE at the IBML at LANL. A key part of these procedures is to limit all handling of LBE and potentially LBE-contaminated parts to a Pb area, which was established in a fumehood. Only filled and sealed corrosion chambers are taken to other areas of the laboratory, such as the beamline for irradiation.

Pb is easily spread as dust, e.g., during machining operations. As a liquid, however, it has very low vapor pressure in its pure form as well as a low partial pressure when mixed with Bi (see Figure 46 and Figure 47 in Appendix 8.1). Therefore, the safest way to fill the chambers is by filling them with liquid LBE rather than LBE in powder form. Casting of LBE into a shape that would fit inside of the ICE chamber, so that it could be loaded with a solid block of LBE, was also considered but ruled impractical because of the presence of the TCs.

4.2.3.2. Filling process

LBE was available in the shape of ingots (leftover stock from ICE II experiments, ~4x5x11.5 cm^3) that were hot-knifed by Scott Parker (LANL). LBE pieces are heated to ~200 °C in a raised electric melting pot (McMaster-Carr). The spout at the bottom allows draining of relatively precise quantities of molten LBE down to one droplet at a time, while slag rises to the top. The chamber can be filled in two different ways described in the next paragraph. Matt Chancey (LANL) filled the first several chambers at LANL. No Matts were harmed in this process.

Filling is done in air, either through one of the sides of the flange or through a Swagelok adapter hole. For the first option, the chamber is fully assembled without the samples. A sacrificial steel foil serves as a base, so that filling can be done through the opening on the other side of the flange. Care must be taken to cover the knife edge, which was done with a 200x200 mesh AISI 304 wire cloth disc (McMaster-Carr). A holder to prevent the chamber from tipping over (primarily for the version with the sapphire window because it extends beyond the bolt heads) was machined by Jeff Bickel (UCB). After the chamber is filled, a second steel foil is added, and the chamber is reheated on a hot plate (provided by Carl Cady (LANL)) to redistribute the LBE. This is necessary because the LBE's high surface tension prevents filling of the chamber "to the brim" of the knife edge, which leaves a rather large air gap between the LBE and the sample that can lead to pre-oxidation of the sample at the beginning of an experiment. This method is the easier of the two, but always slightly underfills the chamber and makes contaminating the knife edge with LBE a possibility.

The other option is to fill the chamber through one of the TC holes. This requires assembling the chamber, including the TCs, which are bent towards their respective samples. Then, one of the TC Swagelok adapters is marked to ensure the correct orientation of the adapter and the TC is known. With the adapter removed, the chamber is closed on both sides with steel foils and heated. For filling, the threads can be covered to protect them, but this was found to be unnecessary because the LBE simply flows down into the chamber along the threads. While still hot, the

removed TC adapter and the TC are mounted on the chamber. Once frozen, the steel foils are then replaced with the samples. This method produces much fuller chambers but is slightly more complicated as the adapter must be mounted while the chamber is between 150 and 200 °C to ensure that the TC can rotate freely in the liquid LBE. Figure 17 illustrates why this extra effort was made: a) shows the fill level of a severely underfilled chamber and the significant amount of PbO production as a result of it. By contrast, no LBE oxidation is observed when chambers are filled properly as in Figure 17 b) and c).

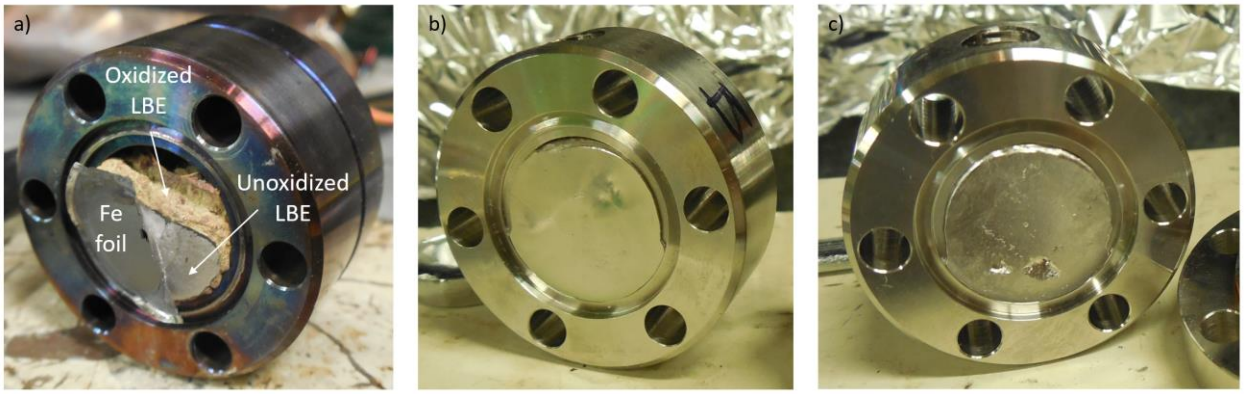

Figure 17 – a) Underfilled ICE III chamber after corrosion test. The presence of excessive amounts of air produced substantial amounts of PbO (yellow). LBE only remained metallic in the center where it was in good contact with the sample and air could not penetrate. b) and c) show properly filled chambers. Sometimes, air inclusions remain, but they should rise to the top once the LBE is molten again and have no impact on the experiment.

4.2.4. Sample removal

Removing the samples after the experiment is non-trivial. It is possible to cut the chamber in half, but then they cannot be reused. This would also require the use of a saw where Pb-cutting is allowed and has the potential to damage the sample during in process, e.g., by corroding it if cutting fluid is used, or overheating it in the absence of coolant. In some cases, especially after very short (up to 10 hours) experiments where the LBE has possibly not yet fully wetted the samples, they can easily be pulled off the frozen LBE with tweezers, but there is still a significant risk of damaging the samples by bending them.

The most practical approach appears to be to heat up the chamber on a hot plate until the LBE is liquid again, so that Sample B can be removed as the LBE flows out of the chamber and Sample A can be gently removed with light pressure from the LBE-facing side. The tweezers inserted under Sample B (outside of the knife edge) lead to slight bending of the sample near the edge. In the worst case, Sample B may be irrecoverable. For Sample A, however, there may be a small mark on its outer edge, but the damage typically does not extend to the center where the beam spot is located. An attempt to make removal easier by leaving a tab on the samples that the tweezers can grab failed due to the imperfect sealing mentioned in Section 4.2.2.1.

Heating of thechamber after the experiment may theoretically damage the samples, e.g., if they are heated to high enough temperatures and for long enough to oxidize significantly in air. However, since the melting point of LBE is low (123.5 °C), the chamber does not need to be heated much beyond that and the process is relatively quick (20-30 minutes), especially compared to the cool-down after the experiment (a few hours). No significant changes to the sample condition, e.g., due to annealing, are expected to occur.

4.2.5. Sample evaluation

Obtaining proper cross sections of the samples after the experiment is quite difficult. When the samples are removed, some LBE is still stuck to the backside, which means that they would have to be cut by a coolant-free slow-speed saw where Pb-work is allowed. This was not readily available, but even if, sample polishing afterwards is still a challenge. Attempts were made to polish cross sections of uncorroded Fe foils in various configurations (cast in epoxy standalone, backed with Crystalbond (Ted Pella), sandwiched between steel shim), but the foils either tore if they were not backed by metal, or had heavily scratched surfaces because they were softer than the backing. Softer backing metals may prevent scratching but were not used in this work.

An alternative is to cut the sample with a laser where Pb-work is allowed, which was attempted by Chai Peddeti (UCB). Unfortunately, the cutting parameters were not set properly, and the femtosecond laser vaporized the sample locally and redeposited a mix of the vaporized species on the sample surface. With properly set parameters, this technique should produce clean cuts in the sample, but given the limited availability of samples and the number of tunable parameters, this approach was not explored further.

Ultimately, the most accessible solution was cutting with a plasma focused ion beam (PFIB, Helios Xe PFIB) in the Electron Microscope Laboratory (EML, LANL). Xe was used to mill samples, which produced rather well-polished surfaces at 1 μA current or lower over large areas. Cutting at the maximum available beam current of 2.5 μA appears to sputter the atoms in the cutting area so quickly that they cannot migrate away and are instead re-implanted into the sample. Cutting occurs at the standard FIB tilt angle of 52° and the created cross sections can then be analyzed in the SEM (FEI Apreo 1 SEM (EML, LANL)).

However, all samples have a slight curvature to them, so they are not perfectly flat. Depending on the local curvature of the sample and the orientation of the FIB cut relative to it, the angle between the surface and the cross section, which is supposed to be 90°, is slightly different. As a result, tilt-corrected measurements, which assume a flat surface, do not give reliable values for the foil thickness. Therefore, three tilt angles of 15°, 30°, and 45° were used to estimate the apparent thickness of the relevant layer indirectly. Since all measurements d_{meas} at each angle measure the same distance in cross section d_{layer}, these values are related according to

$$d_{layer} = \frac{d_{meas}}{\cos\left(\alpha_{remap} - \beta_{corr}\right)},$$

where the real tilt angles of 15°, 30°, and 45° are mapped to 60°, 45°, and 30° (α_{remap}), respectively. This mapping results from the observation that the cross sections were typically still visible at 0° stage tilt and only disappeared around -15°, making this the "true" 90° angle of the cross section relative to the horizontal plane. The correction angle β_{corr} is a variable that changes for different locations on the sample and is optimized for each measurement, such that the three estimates of d_{layer} agree to within 1-2 μm at most. The agreement is quite good, especially given measurement uncertainties due to human error when attempting to recognize the same cross section at three different tilt angles and measuring its width exactly, which is especially difficult for shallow angles.

4.2.6. Oxygen sources

Since the chamber is filled in air, the LBE is expected to be at saturation O concentration (see Figure 4). At 200 °C in air at 1 atm, the saturation concentration is ~10^{-7} wt% (see Figure 4). The average atmospheric pressure at LANL is 0.766 atm, which implies that the O saturation concentration is slightly lower. Regardless, at the target temperature of 450 °C, ~10^{-7} wt% is in the middle of the oxide-forming operational regime. A concentration above ~10^{-9} wt% dissolved O must be maintained for the entire duration of the experiment, i.e., up to 200 hours, to maintain an oxide-forming environment. Air is one source of O, both from the air-filled plenum above the LBE and small air bubbles that are inevitably left during filling that should rise to the plenum as the LBE melts. The second source is a Bi_2O_3 pellet (3x3x2 mm^3, 99%, American Elements) that is added to the chamber before each experiment. It would be interesting to measure pellet consumption during an experiment, but unfortunately, a weight-loss measurement is not possible because of LBE adhesion. However, they do not significantly change shape during the experiment, so their consumption is likely limited.

4.2.7. Heater

The heater is a cylindrical ceramic fiber heater (either a 650 W, 120 V full cylinder or two 450 W, 60 V half-shells, Watlow) that is mounted around the ICE chamber and heats it radiatively. The bare metal leads are electrically insulated with spark-resistant wrap-around sleeving (silicone-rubber coated fiberglass, McMaster-Carr), which are temperature-resistant up to 260 °C. For optimal operation, the heater can be thermally insulated with a ceramic fiber blanket (Watlow), which can withstand temperatures up to 1260 °C. Other accessories to improve heating performance, such as black surface coating for the interior of the heater (Watlow), were kept in reserve to increase heating efficiency further if needed. During the experiment, a camera (C930e webcam, Logitech, connected to a Raspberry Pi 4 Model B with 4 GB RAM, element14) is mounted near the heater to monitor the inside of the shielding enclosure (see Section 4.2.11.2).

The heater is operated manually through a variable transformer (model 3PN1010, Staco Energy Products Company) to maintain constant power output and promote temperature stability of the chamber. Attempts were made to control the heater with a controller (SDC120KC-A, BriskHeat) with feedback from chamber TCs or a TC in the heater. With the chamber TCs, the heater ramped up to extremely high temperatures rapidly (> 700 °C in 2 minutes) because of the thermal lag of the chamber and because a ramp rate cannot be set on this controller model. Using immediate feedback from the TC in the heater (also a sheathed K-type, Omega) produced a more stable ramp curve (aided by slowly increasing the set point manually) but led to cyclical behavior once the chamber was at temperature, especially if the TC control was then replaced with one of the chamber TCs due to the aforementioned lag. Since the beam needs to be monitored continuously regardless, direct manual control of the heater ended up being easiest.

4.2.8. Temperature data

Temperature data from the chamber TCs, TC_A (irradiation-corrosion side) and TC_B (corrosion-only side), as well as the heater TC, TC_H, are recorded with a temperature data acquisition add-on (MCC 134 Thermocouple Measurement DAQ HAT, Measurement Computing Company) for the Raspberry Pi. For ramp up and cooldown, temperatures are typically recorded every second. Once the beam is on target and the chamber temperature is stable, intervals can be increased. The short intervals allow the immediate response of the chamber temperature to the

presence of the H^+ beam to be captured (see Figure 18). This shows the start of Experiment 1 (Exp. 1) when the beam is tuned and positioned on the sample, which is why the beam is turned on and off repeatedly.

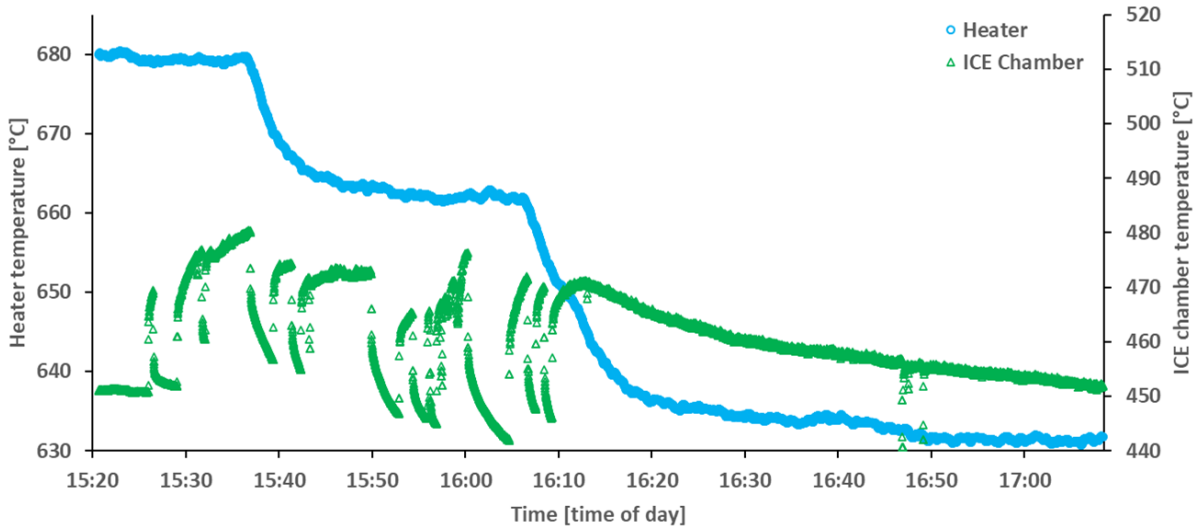

Figure 18 – Temperature data from the start of Exp 1. The chamber temperature (green triangles) is measured by TC_A and responds immediately to the beam turning on or off independently of the heater temperature (blue circles).

4.2.9. Beamline safety

During the experiment, the vacuum in the accelerator is separated from the hot corrosive medium by the sample. Failure of the sample is therefore a concern because of several turbopumps between the beamline end station and the source and the potential for contamination of the end station with Pb. This section describes several steps taken to ensure the protection of the beamline in case of sample failure.

4.2.9.1. Corrosion testing in vacuum setup

Multiple long-term corrosion tests with LBE were performed at different temperatures on a separate vacuum setup. Early tests were performed at UCB to determine if a high vacuum could be held with samples in place. To protect the turbopump in this smaller setup, a 200x200 mesh AISI 304 wire cloth disc (McMaster-Carr) was cut to size and placed underneath the flange on the turbopump inlet. This reduced pump efficiency and affected the vacuum quality at room temperature (increase from 10^{-6} to 10^{-5} Pa range) but did not seem to have a significant effect once the chamber was at temperature. At that point, the vacuum is primarily affected by the outgassing of components close to the hot chamber and the chamber itself. At LANL, a similar vacuum setup was replicated in the newly established Pb area. Corrosion tests with the current chamber design were performed for up to 200 hours (450 °C, Cu gaskets) and both samples remained intact.

4.2.9.2. Fast-acting valve

While corrosion-only experiments without beam are valuable, previous experience with a similar irradiation-corrosion experiment at LANL with pure Ni and molten NaCl-$CeCl_3$ had shown that excessive beam heating can lead to sudden sample failure regardless (176). For this previous iteration of ICE, a fast-acting straight through vacuum valve (model VS2F, NEC) was installed on

the beamline, which is triggered when the vacuum reaches a set threshold. For the first ICE III experiment, this valve was re-armed. As will be described in Section 4.4.2, this turned out to be unnecessary because, even though Sample A ended up failing after almost 60 hours, the slower acting valves on the beamline successfully closed protected it. Since there was no apparent damage to any parts of the beamline, the fast-acting valve was not used for subsequent experiments.

4.2.10. Proton beam

4.2.10.1. Beam production

The H^+ beam is produced by a SNICS (source of negative ions by Cs sputtering, NEC, see (177)) with a Ti-hydride cathode. H^- ions are accelerated towards the center of the 3 MV NEC Tandem accelerator, where N stripping gas strips the electrons off to produce H^+ ions that are then accelerated further towards the end station. For ICE III, a defocused beam with currents up to 3 µA on an area of up to 3x3 mm^2 is used. The beam energy is set to 4 MeV to strike the balance between radioisotope production (lower energy equals less activation; see Section 4.2.11.1) and experiment duration (thicker samples equal longer experiments and higher possible dpa), while also maintaining consistent defect production at the metal-liquid interface, even if the corrosion front moves over time (see Figure 19). The initial beam setup for all experiments discussed in this dissertation was performed by Matt Chancey (LANL).

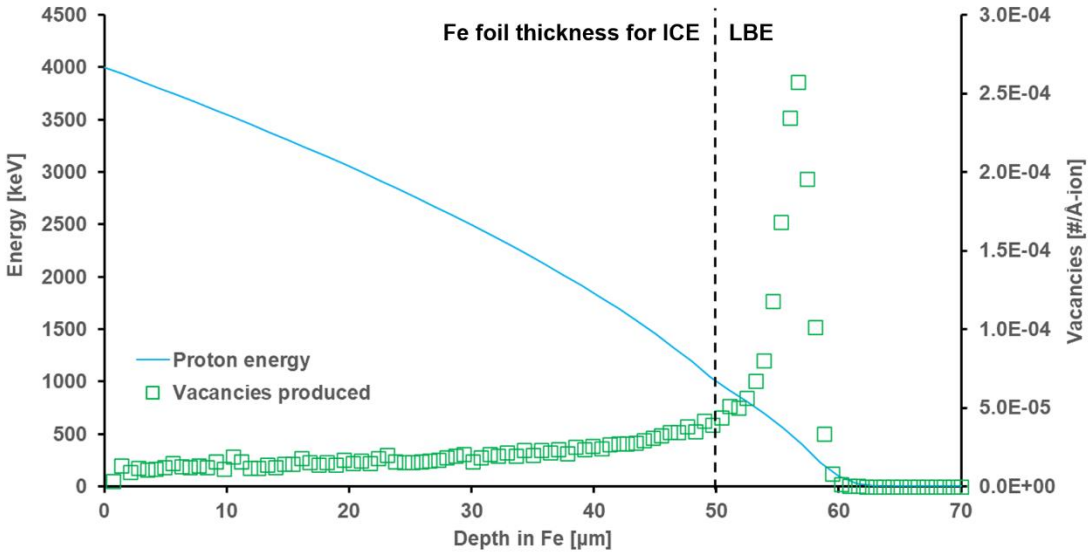

Figure 19 – Dose profile (green squares) and proton energy (solid blue line) for 4 MeV protons passing through 50 µm of Fe, adapted from (178). Vacancies shown to be created in the liquid LBE only serve as an indication of theoretical Bragg peak location.

4.2.10.2. Beam spot location

At the beginning of the experiment, the beam spot must be positioned on the sample, ideally in the center. The chamber is recessed, so the surface of Sample A is only barely visible from the main viewport on the beamline end station and attaching scintillator material to it is not possible. Instead, double-sided Cu tape is taped across a larger DN100CF adapter flange to create a "K-shape", where the wide angle of the K is centered on the sample. Pieces of alumina scintillator are

attached to the tape around the opening. A camera is mounted on the viewport and connected to the Raspberry Pi to monitor the beam spot position during the experiment.

4.2.10.3. Beam monitoring

The beam current is periodically measured (every 30-60 minutes) with a Faraday cup in the end station, which gives accurate values for the current regime (few µA) the experiments operate in. Data points are recorded manually as well as with the help of a Python script that writes Faraday cup readings to file every 5 s. When the Faraday cup is not inserted, spurious currents produce readings in the range of 1e-10 A, which are considered "no current". Unfortunately, the valid data points are scarce compared to how quickly and how drastically the beam current can change. The reported total dose of all experiments is based on linear interpolations of the beam current between readings, which is standard practice for other irradiations. Since the beam needs to be monitored continuously and because the experiment cannot be interrupted, longer experiments require overnight shifts. Daytime monitoring for the experiments was supported by Matt Chancey (LANL), Hyosim Kim (LANL), and Yong Wang (LANL).

An indirect measure of beam current can sometimes be deduced from the total number of counts or the number of counts for certain peaks in the x-ray spectrum recorded by the x-ray detector (see Section 4.3.2 for more detail). However, unlike regular metal irradiation targets, whose composition does not change significantly over the course of the irradiation, the Fe samples in ICE III undergo significant mass losses (see Section 4.4.3). Due to the lower x-ray energies of Fe K-series x-rays (~6-7 keV, see Appendix 8.4) compared to Pb and Bi L-series x-rays (~12-13 keV), the "missing" Fe x-rays are replaced by disproportionately more Pb and Bi x-rays, because they are attenuated less (see Section 4.3.1). Therefore, the total number of x-rays in the spectrum cannot directly be used as a measure of current (see Appendix 8.4). Another option is to monitor the counts of a single constant peak, such as Al (scintillator, absorber) or Cu (tape), but even these are unreliable due to slight changes in beam spot location and a rise in detector temperature over the course of the experiment, which results in an increase of thermal noise.

The beam shape is monitored qualitatively with a beam position monitor (BPM). The goal is to maintain a defocused beam with a homogeneous proton distribution across the entire 3x3 mm^2 beam spot. Perfect homogeneity is difficult to realize without rastering the beam, which would drastically reduce the current and therefore the deliverable dose. Because of this tradeoff, the defocused beam delivers a slightly higher dose to the center of the beam spot. Overall, however, the exposure difference between the center and the outer edges is assumed to be small.

4.2.10.4. Vacuum monitoring

A high-vacuum ion gauge in the end station is read out continuously by the NEC control software for the Tandem accelerator. Command line tools were used to save vacuum data every 60 s. The intent is to monitor the vacuum quality overall and to detect slow leaks in the end station due to the experiment. Ideally, the vacuum should improve over the course of the experiment as a larger surface area of the end station heats up and is baked out (see, e.g., Figure 20). Extended beam retuning events tend to temporarily increase the pressure by almost an order of magnitude because the Faraday cup heats up and outgasses. Figure 20 also shows brief decreases in pressure when the cup is first inserted, which reflects the removal of the beam from the target, while the Faraday cup is still cold.

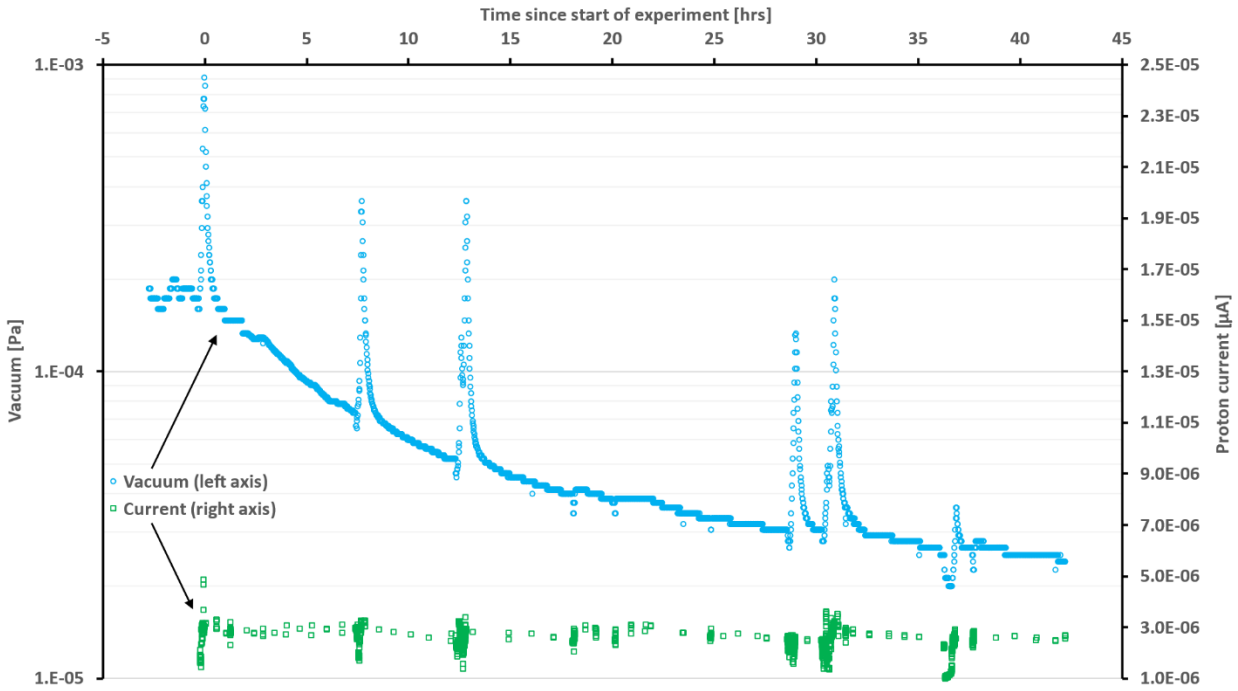

Figure 20 – Vacuum readings (blue circles, here from Exp. 3) in the beamline end station generally improve over the course of an ICE III experiment. The insertion of the Faraday cup for extended periods of time –typically for retuning (clusters of green squares) – leads to sudden increases in pressure.

4.2.11. Radiation safety

Radiation safety is an important aspect of irradiation experiments. This includes understanding of the types and quantities of isotopes likely to be produced, which should inform radiation shielding materials choices to protect operators during the experiment as well as handling procedures for the target after the experiment.

4.2.11.1. Radioisotope production

The target is made of 99.99% pure Fe with an assumed natural isotopic composition of 91.75% ^{56}Fe, 5.85% ^{54}Fe, 2.12% ^{57}Fe, 0.28% ^{58}Fe, and trace amounts of ^{60}Fe. All major isotopes are stable. Noteworthy reactions with 4 MeV protons include:

$$^{54}Fe(p,\gamma)^{55}Co, Q = 5064.07\ keV, \sigma \leq 2\ mbarn$$
$$^{56}Fe(p,\gamma)^{57}Co, Q = 6027.77\ keV, \sigma = \sim 0.5\ mbarn$$
$$^{57}Fe(p,n)^{57}Co, Q = -1618.25\ keV, \sigma < 250\ mbarn$$
$$^{58}Fe(p,n)^{58}Co, Q = -3089.85\ keV, \sigma = \sim 100\ mbarn$$

Natural Pb consists of 52.4% ^{208}Pb, 24.1% ^{206}Pb, 22.1% ^{207}Pb, and 1.4% ^{204}Pb, all of which are stable. ^{205}Pb and $^{209\text{-}214}$Pb are only present in trace amounts. Bi consists almost entirely of ^{209}Bi (100%, with trace amounts of ^{210}Bi), which is very long-lived with a half-life of 2.01x10^{19} years. Hypothetically, there are a few reactions that 4 MeV protons can undergo with some of the listed LBE constituents that could produce radioactive isotopes of Tl, Pb, Bi, or Po. However, given that the protons must pass through 50 μm of Fe, their energy will be reduced to 1 MeV as shown in

Figure 19. Even towards the end of the experiment, when the foil is ~30 μm thick (see Section 4.4.4), the proton energy is reduced to ~2.5 MeV. If the foil breaks, the experiment ends with the automatic valves along the beamline closing within seconds, so there is not enough time to produce substantial amounts of any of these isotopes. Based on the reactions listed above, a mixed radiation field of gamma rays and some neutrons will be produced during the experiment.

4.2.11.2. Shielding

The L15 end station (at a 15° angle with the beam path) is surrounded by a shielding enclosure made of double walls of low-Z polyethylene sheets (~5 cm thick). It has a door that can be pulled back to access the end station and a window that allows for easy access from the side. The window only has one regular polyethylene sheet and a thinner outer sheet of borated polyethylene. This makes it lighter, which puts less stress on the hinges while remaining an effective neutron shield. The original enclosure was built for the previous ICE iterations, but it had to be expanded for ICE III because beamline modifications in the meantime had moved the end station too close to the enclosure door to safely operate the heater. To that end, additional double-walled side panels were cut from the remaining polyethylene stock and screwed onto the existing panels with wood screws, which created an additional 30 cm of space between the door and L15. γ-ray shielding is achieved by hanging Pb-filled bags from the sides of the enclosure. During the experiment, mobile photon and neutron detectors are used to monitor operator exposure at the control panel.

4.2.11.3. Residual radioactivity

The radioisotopes mentioned in Section 4.2.11.1 render a pure Fe sample with an estimated activity of ~1.76 μCi after 200 hours of irradiation, which is the maximum duration originally planned for. Most of this initial activity is due to the decay of ^{55}Co, which has a half-life of 17.53 hrs. Once it has decayed away, the activity is dominated by ^{57}Co ($t_{1/2}$ = 271.74 days) with contributions from ^{58}Co ($t_{1/2}$ = 70.86 days), which is present in smaller quantities. The samples are stored in a radioactive sample cabinet until they have lost most of this radioactivity (at most ~5 months).

4.3. In situ monitoring of corrosion under irradiation with particle-induced x-ray emission (PIXE) spectroscopy

In situ monitoring techniques can provide information about a process continuously, as opposed to the snapshots obtained by only analyzing samples after an experiment. Unfortunately, few irradiation-corrosion studies (e.g., (165)) have used such methods because the experimental design becomes inherently more difficult and, in some cases, the interpretation of the results can be complicated by the presence of the ion beam. However, the ion beam can also produce useful signals as a side effect: High energy ions create displacement damage that also ionize lattice atoms as they travel through the material. The excitation of inner shell electrons leads to the production of characteristic x-rays, which are used in PIXE to characterize the elemental composition of thin specimens in fields such as geology, archaeology, and environmental science (179–181). Here, PIXE was used to continuously monitor the behavior of a sample under simultaneous irradiation and corrosion over time.

4.3.1. Considerations for corrosion monitoring

PIXE is normally used to analyze thin samples that minimally slow down the light ions, such as protons and α particles, passing through. This allows for flexible detector placement (at a shallow angle with the beam axis in front or behind the sample) and it can be assumed that emitted x-rays are not attenuated by the sample. Typical PIXE energies for protons are 2-5 MeV (181). At lower energies, the ionization cross sections of target elements decrease drastically, while at higher energies, the spectrum will increasingly be dominated by nuclear reaction products (181). The measurable sample composition is averaged over the size of the beam spot. Highly focused microbeams can be used for 2D mapping of samples with lateral changes in composition (micro-PIXE, see, e.g., (182)). The production rate of x-rays Y in a thin sample can be described as follows:

$$Y = \phi * N * \sigma * \omega \, ,$$

with the ion current ϕ, the areal number density of target atoms N, the ionization cross section σ, and the fluoresence yield for a specific shell ω. Measuring Y provides a quantitative measurement of sample composition once the detection efficiency is considered, except for special cases where the proximity of two elements A and B with similar x-ray energies (~1 keV apart) leads to the absorption of A's higher energy x-rays by B and subsequent emission of B x-rays (183). This results in an overrepresentation of B atoms and an underrepresentation of A atoms that must be corrected for.

PIXE has also been adapted for thick samples (184). In this case, the energy dependence of σ must be considered as the ion loses energy with depth. In addition, the attenuation of x-rays emitted from deeper layers in the sample must be accounted for. In general, higher-energy x-rays are attenuated less, unless their energy is directly above an absorption edge. In the case of ICE III, the relevant depth for PIXE is the entire thickness of the sample and ideally a small distance into the corrosive medium, so that the metal-liquid interface can be probed. As shown in Figure 19, 4 MeV H^+ passing through 50 µm of Fe still have about 1 MeV of energy to generate x-rays in the corrosive medium.

Attenuation by the sample limits the usefulness of this technique to liquids with higher Z and thinner samples. For example, H_2O cannot be monitored this way unless the sample is extremely thin and the detector sensitive enough to measure O K-series x-rays (0.525 keV). For heavier elements, such as Pb and Bi, a substantial number of L-series x-rays will pass through 50 µm of Fe. Alternatively, the sample can be monitored using only its own x-rays, i.e., without a contribution from the corrosive medium. However, this requires monitoring of the beam current with the help of a consistent spectral peak.

4.3.2. X-ray detector

A high-count-rate (10^6 counts per second (cps) (185)) silicon-drift detector (SDD, here, an Amptek FastSDD®) was used for these experiments. The Si wafer is 500 µm thick with an active area of 25 mm^2 that is located behind a 12 µm thick Be window. The operational energy range of detectable photons is ~0.9 keV to ~33 keV. These limits are based on an arbitrary cutoff at 10% of the detector's intrinsic efficiency, which is shown in Figure 5 of (185). In practice, the lower limit also corresponds to the lower limit set by thermal noise (and therefore the slow threshold) during high-temperature experiments. Under ideal conditions, the SDD's resolution at a peaking

time of 1 µs is 126 eV full width at half maximum (FWHM) for Mn-55 (185). This was tested periodically between experiments with an Fe-55 source.

The SDD is mounted on an Al heat sink with ultra-high-vacuum compatible readout cables. A 15-Pin D feedthrough connects it to an Amptek SDC-915 preamplifier, which is connected to an Amptek PX5 digital pulse processor unit. Amptek's DPPMCA software is used to communicate with the PX5. The PX5 settings had to be adjusted for the high-count-rate environment expected for ICE III and some of the relevant parameters are shown in Table 6. With these settings, the channel width is ~12 eV for 2048 channels. The complete list of settings for the different experiments discussed in this work is shown in Table 12 in Appendix 8.6.

Table 6 – Relevant detector settings for ICE III PIXE.

Gains	Total gain	14.979
	Fine gain	1.028
Shaping parameters	Peaking time	0.8 µs
	Fast channel peaking time	800 ns
	Flat top width	0.2 µs
	Slow threshold	2.5%
	Fast threshold	27 channels
Other settings	Reset lockout	102 µs
	Temperature	265-275 K
	FPGA clock time	80 MHz

The Al heat sink is mounted on a flexible holder (see Figure 21) to allow shallow detector angles with respect to the beam. The original assembly was made of stainless steel that lacked active cooling. During the experiments, this proved to be insufficient as heat buildup within the detector pushed its operating temperature from an ideal range of 220-230 K to up to 280 K. This made active cooling necessary, which has been installed in the form of a chiller (Isotemp 3013, FisherScientific) that recirculates cold water through a tube wrapped around the outside of the flange holding the detector mount. To improve heat transfer between the detector and the flange, the steel holder parts were replaced with almost identical Al parts with additional space to mount a Rutherford backscattering spectroscopy (RBS) detector in addition to the SDD (see Figure 21).

The detector is mounted ~30 cm away from the sample surface at an angle of ~6° with the beam. This ensures that the detector has the beam spot in its field of view. Since 4 MeV protons will produce a significant number of x-rays, it is important to estimate how many x-rays will be produced per second and if this is within the count rate range of the detector (1 Mcps).

Generally, lower count rates are desirable because they reduce pileup for large peaks, such as the Fe peak, and improve peak resolution. To achieve this, the detector can be moved further away from the source to cover a smaller solid angle, which is not possible in this case due to space constraints, or an absorber may be placed in front of it to attenuate some of the photons. The absorber thickness must be chosen as a compromise between detector pileup and attenuation of (initially) low-intensity peaks from the corrosive medium that are attenuated by both the sample and the absorber. Alternatively, reducing the beam current would lower the count rate, but also decrease the dpa delivered to the sample.

The details of the following calculation are shown in Appendix 8.7.1. The estimate shows that a maximum of about 2.03×10^{12} x-rays per second will be produced by a 3 µA current of 4 MeV protons incident on pure Fe. Note that this calculation does not consider energy loss of the protons or x-ray attenuation in the sample and is therefore likely an overestimate.

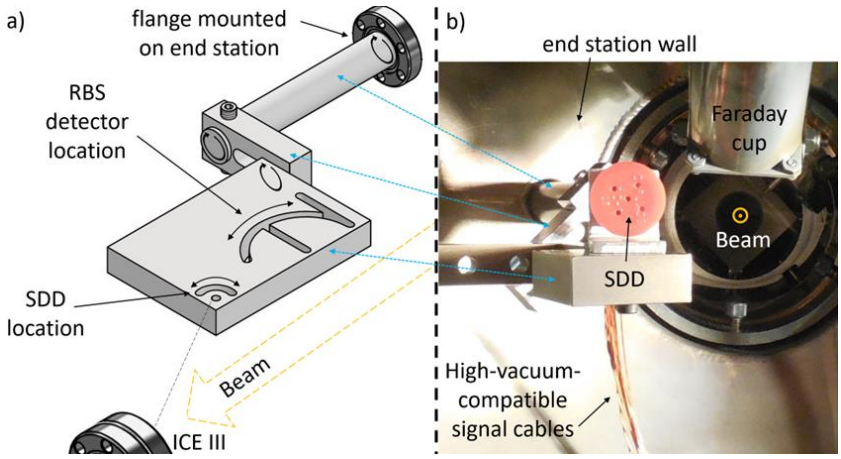

Figure 21 – a) Assembly drawing of a newer version of the detector holder that has additional space for an RBS detector. The circular arrows indicate rotatable parts, and the curved arrows show how much the detectors can swivel, so that their line of sight (dashed black line for the SDD) is as parallel to the beam as possible. b) Photo of the original steel holder with the SDD mounted from the perspective of the ICE III chamber.

Since the detector is 30 cm away and has a surface area of 25 mm^2, the geometric efficiency ϵ_{geom} is roughly 2.21×10^{-5} (see Appendix 8.7.2). While this is a substantial reduction, this would still mean that the detector is exposed to 10 Mcps, which it is not designed for. Additionally, while the Fe K x-rays are expected to be the largest contributor, there will be other x-rays in the spectrum that will add to the total x-ray count. Therefore, some form of attenuation is needed, which is added in the form of a stack of Al foils held by the detector cap.

With 240 µm of Al (ϵ_{Al}: 5.69×10^{-4}) and 12 µm of Be (ϵ_{Be}: 0.994), the x-ray source term is reduced significantly:

$$\epsilon = \epsilon_{geom} * \epsilon_{Be} * \epsilon_{Al} * \epsilon_{\mathrm{det}} = 1.01 * 10^{-8} * \epsilon_{\mathrm{det}},$$

where ϵ_{det} is a catch-all for other relevant factors, such as the intrinsic detector efficiency, electronic losses, and attenuation contributions of the polymer cap holding the Al foils. Note that ϵ_{Al} is given for 6 keV photons here as an example (see Appendix 8.7.4).

To test the detector at high count rates with the chosen absorber thickness, a 3.3 µA 1.5 MeV proton beam was used to irradiate 5x3 mm^2 of pure Fe (99.99%, GoodFellow). Over the course of two minutes, 41000 x-rays were counted, which corresponds to 342 x-rays/s. A source term estimate similar to the one for 4 MeV protons gave a theoretical yield of 9.56×10^{10} x-rays/s produced in the sample (see Appendix 8.7.3). This means that the experimental efficiency is

$$\epsilon_{\mathrm{exp}} = \frac{342}{9.56 * 10^{10}} = 3.58 * 10^{-9},$$

which is only an order of magnitude lower than the estimate above. This is likely due to inaccuracies in the calculation, as mentioned previously, and there may be a small contribution from ϵ_{det}. Overall, an agreement between the theoretical and the experimental estimate within an order of magnitude is quite reasonable and supports the choice of absorber thickness. One thing to note is that the presence of such an absorber preferentially filters x-rays of lower energies, which hardens the x-ray spectrum.

During actual ICE III experiments, count rates between 10^4 and 10^6 counts per second have been recorded for up to 3 µA of 4 MeV protons incident on pure Fe. A new spectrum is recorded every 5 s to allow for the removal of spurious x-rays and noise, which are recorded during current measurement and beam retuning events. This acquisition time does not exactly correspond to real time that has passed, which is typically closer to 6 s. This difference is due to interruptions in data collection, e.g., during data transfer (see (186) and Appendix 8.8 for more detail). The collection times referred to in this text are the constant acquisition times of the spectra.

4.3.3. Calibration curve

During the first experiment, PIXE data showed a reduction in sample thickness (see Section 4.4.2). Even though it was not clear yet if corrosion was uniform or localized, the hope was that PIXE could be used to estimate the sample's thickness continuously throughout the experiment. To establish a simple connection between the PIXE signal and the thickness, a standard was needed. The alternative is to model the spectra with assumed Fe and LBE distributions, which would require additional microscopy information.

Most of the content of this section has been published in (178). For the standard, a fixture was designed that can hold a solid LBE tablet and Fe foils (see Figure 22 c)). The tablet was produced by filling the center hole of the base flange with liquid LBE and pressing it flat with a stamp matching the hole diameter. 5 and 10 µm thick Fe foils (99.85%, Goodfellow) are stacked on the tablet to achieve different Fe thicknesses. The tablet is not heated during the irradiation to reduce the time between measurements. This means that the slightly higher density of LBE at room temperature compared to LBE at 450 °C will lead to a slight overrepresentation of PbBi x-rays in the calibration curve derived from the standard. Additionally, the narrower opening of the holder generates a larger steel background in the spectra than is present during an ICE run.

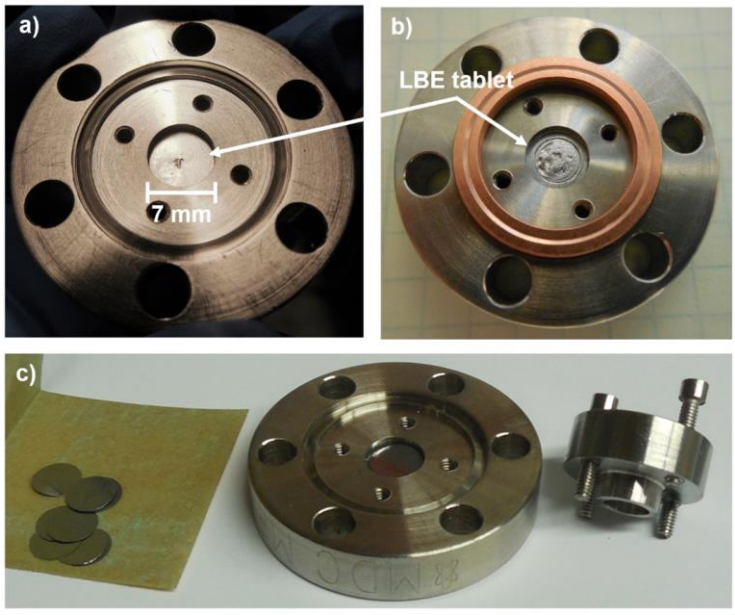

Figure 22 – Calibration curve standard fixture. a) and b) show the LBE tablet before and after the measurements for Experiment 2. c) shows the individual Fe foils on the left and the holder that screws into the DN16CF base flange. Adapted from (178).

To reduce systematic bias between experiments, e.g., due to detector position, a calibration curve needs to be produced for each experiment individually. Each measurement takes about 45 minutes (mounting / unmounting, vacuum venting and pumping, irradiation), so a curve with 5 µm steps from 5 to 50 µm and one at 70 µm (noise, see next paragraph) can be produced within a workday. Measurements were done with 4 MeV protons, but at lower currents than in the regular experiment (1-2 µA as opposed to 3 µA) and with a smaller beam spot size (2x2 mm^2 vs. 3x3 mm^2) to reduce the activation of the foils and the LBE. As in the actual experiment, spectra were collected every 5 s.

The largest peaks present in the spectra from Experiments 2 (Exp. 2) and 3 (Exp. 3) are the $Fe_{K\alpha}$ peak for Fe and the $Bi_{L\beta}$ peak for LBE. The ratios between the x-ray counts in these peaks are used in the calibration curve (see Figure 23 and Figure 24). Taking the ratio of two peaks in the spectrum removes the impact of proton current variations (assuming that the dead time is sufficiently small and that the current is not so high that pile-up is non-negligible). The $Fe_{K\alpha}$-$Bi_{L\alpha}$ curve for Exp. 2 is also shown for the interpretation of Exp. 1 (see Section 4.4.2). The stack thickness is first increased in 10 µm steps starting from 5 µm (blue and yellow circles) and then decreased starting from 45 µm (green and red squares). This is done to ensure that there are no changes in the PIXE signal due to accumulated beam-induced damage to the LBE tablet (see the holes introduced by local vaporization of the LBE tablet after all measurements for Exp. 2 in Figure 22 b)). For Exp. 3, the calibration curve is established similarly. In addition to the curves, there is also a group of measurements with a 70 µm thick stack (black triangles). This is too thick for 4 MeV protons to pass through, and so the "ratio" of Fe to counts in the Bi x-ray bins constitutes a background measurement. The $Fe_{K\alpha}$-$Bi_{L\beta}$ ratio at 50 µm is clearly distinct from background, which is impressive considering that the channel with the most counts in the $Bi_{L\beta}$ peak contains less than 10 counts for a 5 s interval. In comparison, background noise generates 0-2 counts per channel in the same amount of time.

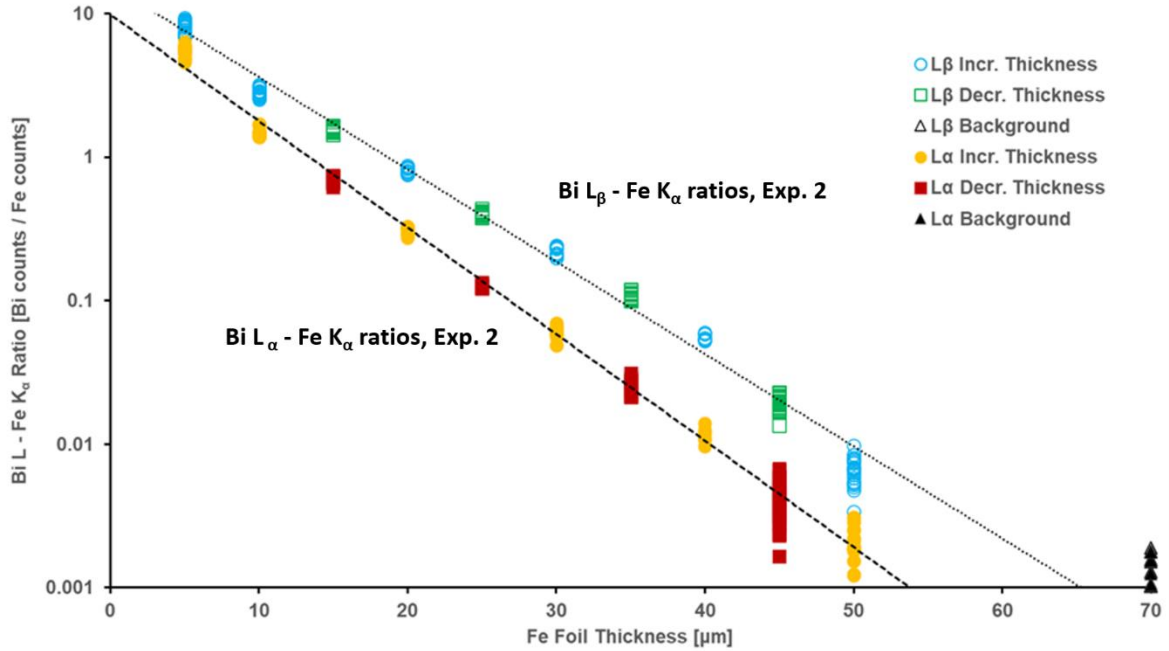

Figure 23 – Semi log plot of calibration curves for Exp. 2 (adapted from (178)). Each data point corresponds to a 5 s long spectrum and ratios were obtained with the 3-channel method (see Section 4.3.4). The trendlines are based on all data points excluding background at 70 µm.

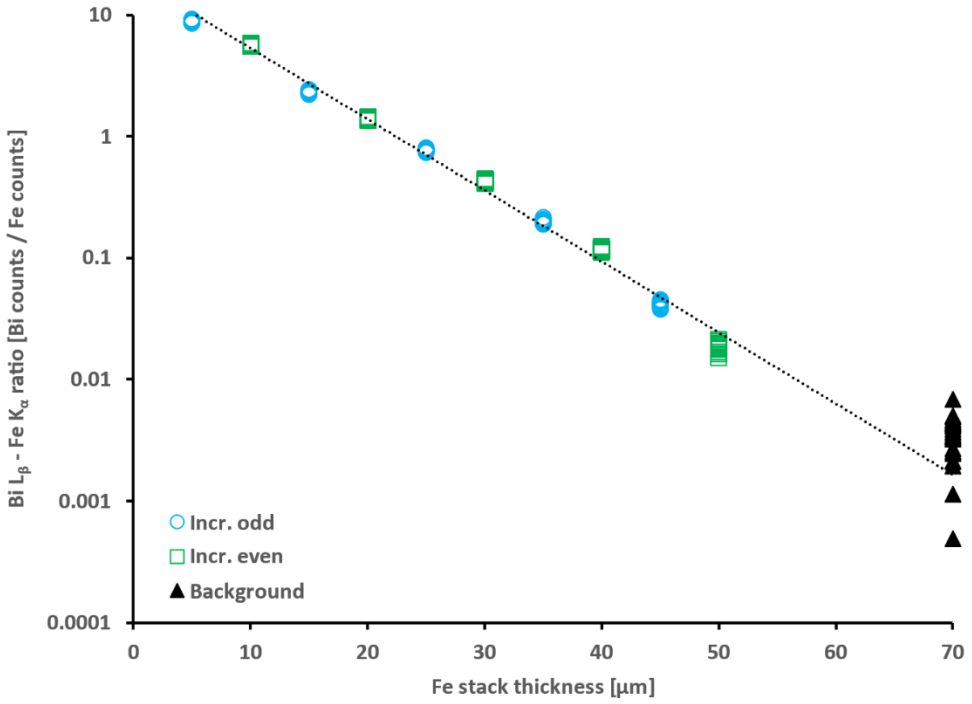

Figure 24 – Semi log plot of the calibration curve for Exp. 3. Each data point corresponds to a 5 s long spectrum and ratios were obtained by Gaussian peak fitting (see Section 4.3.4). Spectra were taken in 10 µm increments from 5 µm to 45 µm, followed by background (70 µm), and another series of 10 µm increments from 10 µm to 50 µm. The trendline is based on all data points excluding background at 70 µm.

4.3.4. Data processing

During ICE runs, the beam is taken off the sample frequently during beam tuning and when the current is measured. The insertion of the Faraday cup creates stray x-rays, so any spectra taken at this time contain erroneous data. These spectra have significantly fewer total counts because of shielding from the Faraday cup, so any spectrum with fewer total counts below a set threshold is discarded. However, this threshold should be set carefully to account for beam current variations over time.

Because of the low background (see previous section), spectra are processed directly without background correction. Initially, only counts in the three center channels of each peak were considered to reduce the impact of overlapping peaks (see (178)). Peaks are typically much broader (~30 channels), and so later, Gaussian functions of the following form were fitted to the peaks:

$$f(x) = a * \exp\left(-\frac{(x-b)^2}{2c^2}\right),$$

where a corresponds to the amplitude, b to the peak center, and c to the peak width. The values are bounded between 0 and positive infinity and fitted with the lsqcurvefit function in MATLAB R2018b. Initial guesses for each variable are obtained by evaluating the sum of all spectra for a given data set. Despite this, the results of Gaussian fitting tend to vary significantly early on in the experiment because error minimization for peaks as small as the PbBi peaks can lead to a variety of different solutions, which affects the spread of the calculated Bi-Fe ratios.

The difference between the calibration curve Bi-Fe peak ratios produced by both methods is shown in Figure 25. For the same data, fitting Gaussians to the peaks and forming ratios with the area under the respective curves leads to a right-shift compared to ratios calculated based on the three center channels of each peak. Between the two experiments, there is reasonable agreement, but a difference is visible and becomes larger as the Fe foil stack becomes thicker. This is likely due to slight differences in detector positioning between the two experiments.

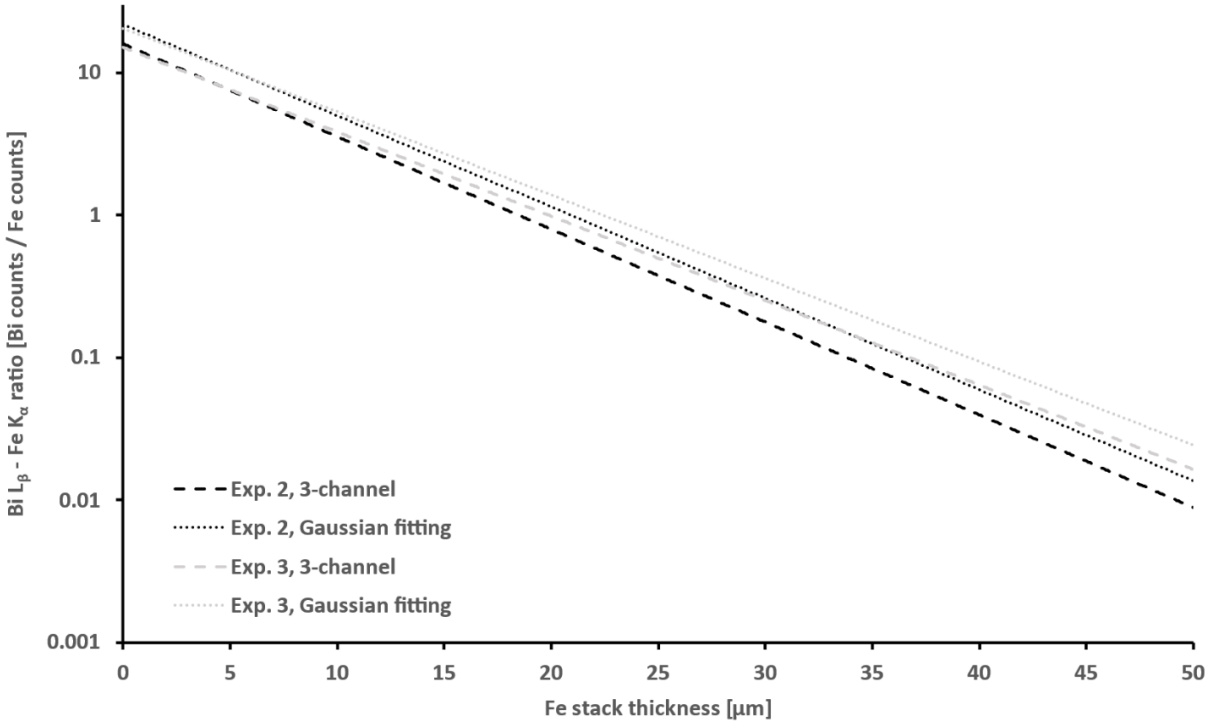

Figure 25 – Comparison of Bi L_β – Fe K_α calibration curves for Exp. 2 (black lines) and 3 (grey lines) calculated with the 3-channel method (dashed lines) and with fitted Gaussian curves (dotted lines).

4.3.5. Alternative corrosion monitoring techniques

Several other in-situ techniques could complement or replace PIXE for the purpose of corrosion monitoring, such as Rutherford backscattering spectroscopy (RBS), particle-induced gamma emission spectroscopy (PIGE), and electrochemical methods. The latter require the addition of electrodes to the chamber, which is briefly discussed in Section 4.5.1.

4.3.5.1. Rutherford backscattering spectroscopy (RBS)

RBS measures the number and energy of light ions – typically α particles, but protons may be used as well – backscattered from the sample and is commonly used in conjunction with PIXE (see, e.g., (187, 188)). This information is used to estimate a sample's composition and porosity, as well as the thickness of layers in layered samples (187). In the case of ICE III, RBS could provide an additional surveillance tool for the sample and possibly produce a measure of oxide layer thickness. It could also provide information about the distribution of low Z coolants that PIXE is not sensitive to because of their low x-ray energies. RBS was not used for the experiments presented here, but preparations for adding an RBS detector for future experiments are underway.

4.3.5.2. Particle-induced γ emission spectroscopy (PIGE)

PIGE is the γ-ray equivalent of PIXE. It is sensitive to specific isotopes that undergo γ-producing nuclear reactions under ionizing radiation, which can make the resulting spectra challenging to interpret, but extremely useful in special cases (189). For example, it could be used for ICE III with a molten salt as the corrosive medium that contains one the following isotopes: ^{19}F, ^{23}N, ^{24}Mg, or ^{26}Mg (based on a list of relevant isotopes in (189) and known (p,p'γ) reactions with 1 MeV protons listed in (190)). At higher energies, other reactions, such as the (p,p'γ) reaction for ^{35}Cl open up, but sample activation would also be increased (see Section 4.5.1.3). Currently, there are no plans to add a detector for PIGE, but it may be considered in the future.

4.4. Irradiation-Corrosion Experiment III operation and results

Figure 26 gives an overview of the experimental duration and dpa achieved for three irradiation-corrosion experiments (Exp. 1, 2, and 3) conducted during this work. Table 7 shows the experimental parameters in more detail. In this section, the general experimental conditions will be discussed, followed by a brief description of each experiment, temperatures measured, in situ PIXE results, and post-irradiation analysis. The results and their implications will be discussed at the end.

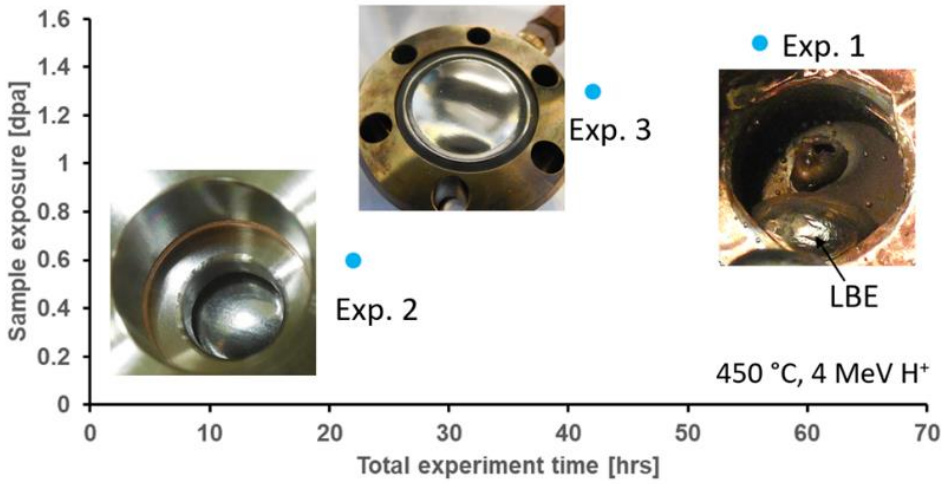

Figure 26 – Theoretically achieved dpa vs. total experiment time for the three experiments discussed in this section. The photos show the samples after the experiment. Photos for Exp. 1 and Exp. 2 are adapted from (178).

Table 7 – Experimental parameters for Exp. 1-3.

	Exp. 1	**Exp. 2**	**Exp. 3**
Target temperature [°C]		450	
Beam energy [MeV]		4	
Beam current [μA]		Up to 3	
Beam area [mm^2]		~3x3	
Total experiment time [hrs]	56	22	42
Fluence [ions/cm^2]	3.09E19	1.24E19	2.72E19
Exposure [dpa]	~1.5	~0.6	~1.3

4.4.1. Experimental conditions

Since the purpose of these experiments is to determine the interplay of irradiation and corrosion, it is important to ensure that both processes occur at relevant rates. Below 400-450 °C, corrosion of steels in static LBE will occur but at slow rates. Above 450 °C, both oxidation and dissolution rates in steels are drastically increased (see Figs. 3.26 and 3.28 in (51)). Since Fe corrodes much faster in comparison, an experiment temperature at or below 450 °C is desirable to ensure that measurable corrosion will occur without immediate sample failure. Corrosion testing revealed that 50 μm thick pure Fe foils can last up to 200 hours and possibly longer in the ICE III chamber at 450 °C without breaking.

On the radiation damage side, very high temperatures are undesirable because radiation damage will anneal at increased rates. At lower temperatures, radiation effects manifest more obviously, e.g., below 425-450 °C, irradiation hardening occurs in F/M steels (55). To strike a balance between the corrosion and radiation-induced processes, the experiments are run at 450 °C. The beam current was set to 3 μA on a 3x3 mm^2 area, which is roughly the maximum achievable stable current for 4 MeV protons on the IBML Tandem accelerator to guarantee a significant amount of radiation damage being imparted on the sample. The reasons for choosing 4 MeV for the beam energy are discussed in Section 4.2.1.2.

Reaching the target temperature of 450 °C takes a few hours. An experiment officially begins once both chamber TCs have reached 450 °C. Without beam on target, TC_B typically reads slightly higher temperatures because it is located deeper in the heater, while TC_A is closer to the end station, which has a lot of thermal mass. Once the beam is on target, TC_A reads ~10-20 °C more than TC_B. The heater is then turned down, so that TC_A reads ~450 °C with the beam on. Whenever the beam current drops and leads to a decrease in temperature, it is adjusted back to ~3 μA. The heater temperature must be adjusted periodically as the end station heats up.

4.4.2. Experiment 1

The purpose of Exp. 1 was to determine how long ICE III with 50 μm of pure Fe could run with beam on target. Much of what is presented in this section is covered in (178). As mentioned previously, under corrosion-only conditions, the samples did not break even after 200 hours at 450 °C. With the proton beam, however, Sample 1A failed after ~60 hours and 1.5 dpa. The result was an immediate drop in vacuum, at which point the automatic valves along the beam line closed. The only manual turbopump valve is in the end station and was also closed immediately. For unclear reasons, the fast-acting valve did not close even though it had been tested successfully and re-armed for this experiment. One possible reason is that the battery needed to activate the valve was depleted during testing. Regardless, since the regular automatic beamline valves successfully protected the pumps higher up the beamline, the fast-acting valve was not used again.

Figure 27 shows the aftermath of Exp. 1. Some of the LBE had escaped and solidified a few cm away from the chamber. The largest LBE droplet showed black impurities arranged in a flow pattern, which were originally thought to be corrosion products from the experiment. Energy dispersive x-ray spectroscopy (EDS) analysis in the SEM showed, however, that the highly symmetrical crystals are primarily pure Cu and occasionally a Cu-Al alloy. Cu was likely picked up by the LBE flowing over the Cu tape and the Cu gaskets. It is less clear where the Al originated from, but it is possible that it is present as an impurity in the Cu tape. The tape near the chamber was intended to help guide the beam with the Cu x-ray signal, which did not work well because Cu is also present in the beam-guiding “K shape” mentioned in Section 4.2.10.2. In addition, heating up Cu tape this close to Sample A during the experiment likely leads to a significant

amount of outgassing that may oxidize the sample from the vacuum side. Because of these considerations, no tape was used near the ICE chamber in subsequent experiments.

Exp. 1 was a test in several other ways: Unlike later experiments, it had only one TC in the chamber, which recorded a temperature increase of ~30 °C within seconds of the beam hitting the target (see Figure 18). Furthermore, the recorded x-ray data is rather spotty. The original intent of the SDD was not to do PIXE, but to monitor the beam current, which turned out not to be possible in a straightforward manner (see Section 4.2.10.3). The gain was unintentionally set too high, so that only Pb and Bi L_α x-rays could be recorded. Also, only one spectrum was going to be collected for the entire duration of the experiment, as opposed to the 5 s intervals used in later experiments. However, after ~17 hours of collection, the channels in the center of the $Fe_{K\alpha}$ peak, which is the largest in the spectrum, reached an integer overflow condition. This occurs at $2^{24} = 16.78E6$ counts because the PX5 digital pulse processor allocates 3 bytes per channel according to the Amptek manual (191). To restore the total number of x-rays, this number can simply be added after the experiment as many times as certain channels reset. However, not only is it tedious to keep track of which channels have reset and how often, but the reset channels also interfered with the dead time estimates produced by the software. To avoid this issue, the spectrum was subsequently restarted every few hours.

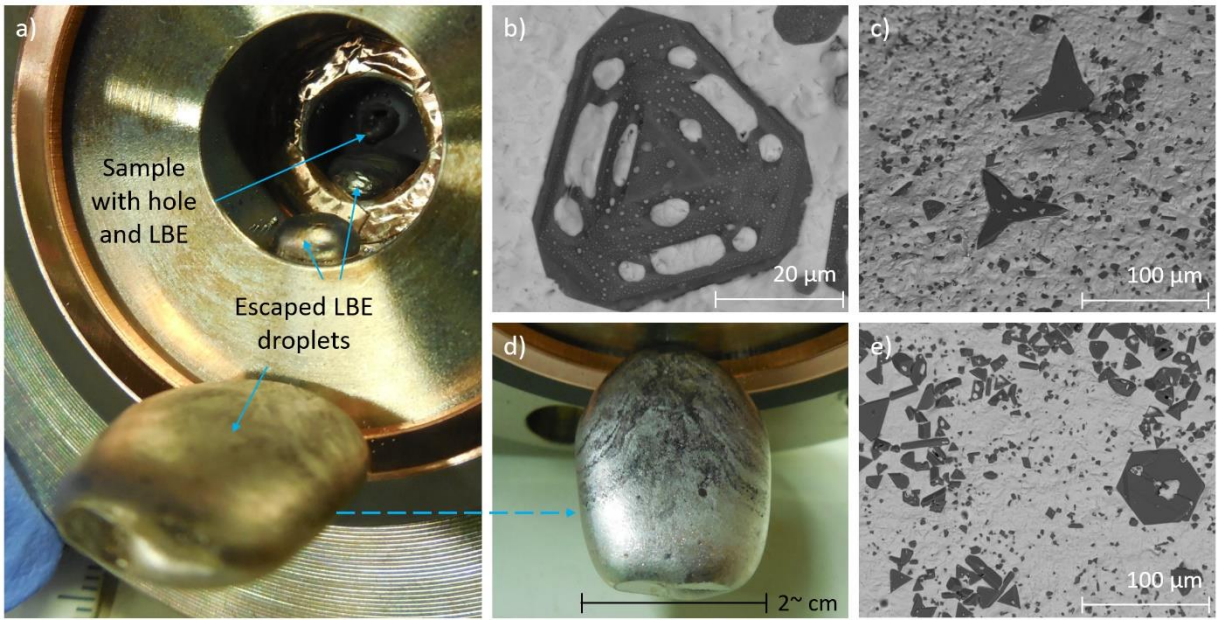

Figure 27 – Photos of LBE escaped from the chamber (a) and d)) and SEM images (b), c), and e)) of Cu crystals (dark grey) grown in the largest escaped LBE (light grey) droplet (d)).

Despite how irregularly the spectra were taken, they contained plenty of useful information. Figure 28 shows an overlay of normalized spectra taken after 6, 28, 36, and 52 hours. Their respective dead times are 14.47%, 30.45%, 27.55%, and 35.79%. In the low energy range, more thermal noise is observed as the end station and the detector heat up. The Fe and Fe_{escape} peaks decrease slightly (note that this is a log-scale) and there is a clear and dramatic increase in Ni, Pb, and Bi peaks. Ni is often present as a background peak because all flanges and the end station itself are made from stainless steel. However, the only steel component that may be directly in the beam path is the TC sheath. Together with the increase in counts from the LBE, this indicates that the

foil is thinning out, which is sensible, given that it ruptured after 52 hours of irradiation (56 hours total experiment time).

For later experiments, there is a calibration curve that links Fe foil thicknesses to PIXE measurements (see Section 4.3.3). For Exp. 1, this had not been done, and so an attempt was made to estimate the thickness of Sample 1A based on the calibration curve for Exp. 2 (see Figure 29). Figure 29 a) shows ratios between the sum of $Pb_{L\alpha}$ and $Bi_{L\alpha}$ x-ray counts and $Fe_{K\alpha}$ counts, which were recorded by hand. The different sets correspond to the different cumulative x-ray spectra they were extracted from. Since the ratios are cumulative, each spectrum reset introduces a discontinuity.

In Figure 29 b), an estimate of the sample's thickness is given based on the comparison of the extracted $Bi_{L\alpha}$–$Fe_{K\alpha}$ ratio from Exp. 1 and the calibration curve from Exp. 2. The dotted lines are a direct conversion of the ratios shown in a). However, since these are cumulative, they need to be converted to the "true" non-cumulative ratio at any given time, shown as the solid line. The ratios for Exp. 2 were taken between the three center channels of each peak, and so a direct comparison is only possible when spectra were saved, so that accurate values for the three center channels can be used. Those ratios are the large symbols shown in b) and, since they are also cumulative, they should be compared to the dotted lines, which they are in reasonable agreement with. To obtain thickness estimates (dashed lines) for these data points, they need to be compared to the dotted line from their set, projected onto the solid line, and then compared to the thickness, as shown with arrows for the last data point, which should have a true ratio of ~0.22, and therefore a thickness of 20-25 μm. Since Sample 1A was effectively destroyed at the end of the experiment, it was unfortunately not possible to confirm this with microscopy.

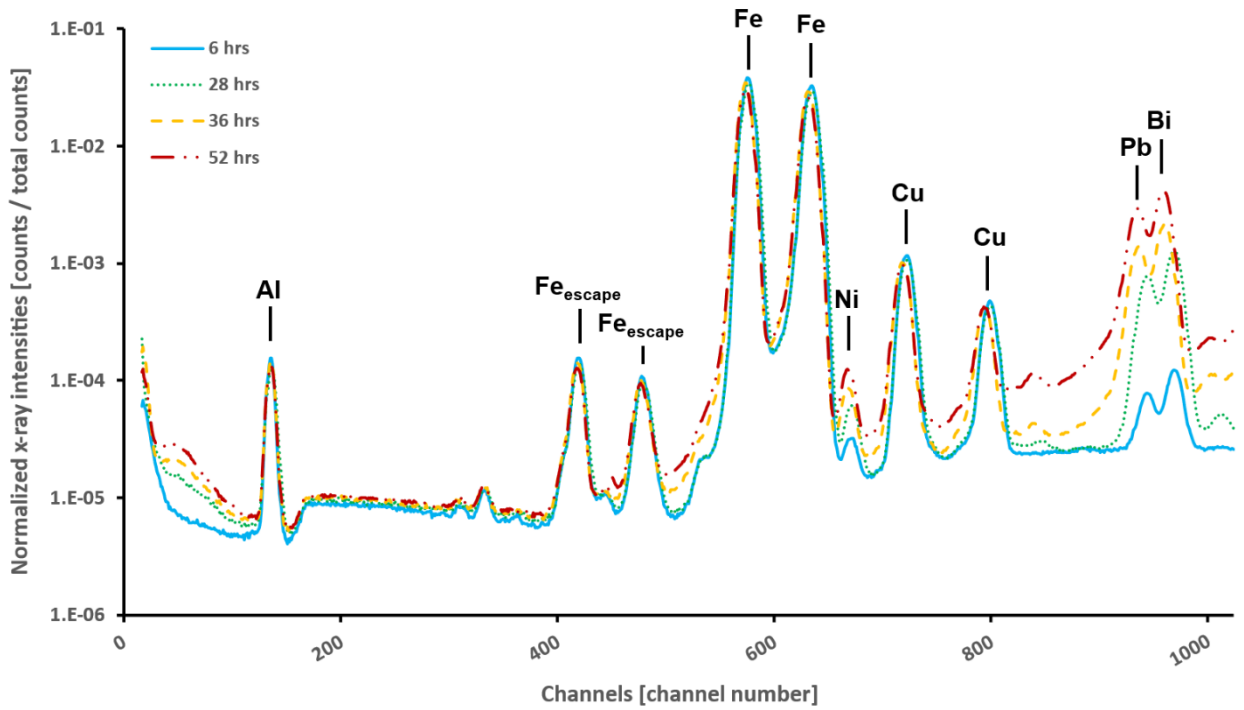

Figure 28 – PIXE spectra taken after 6 (solid blue line), 28 hours (dotted green line), 36 hours (dashed yellow line), and 52 hours (dashed and dotted red line) with relevant peaks labeled. Counts are normalized to the total number of counts in the spectrum and plotted on a log-scale.

4.4.3. Experiment 2

Exp. 2 was the first to feature 2 TCs and a "proper" PIXE setup as described in Section 4.3 with spectra taken every 5s. Like in Exp. 1, there is an immediate temperature increase (~50 °C for TC_A and ~30°C for TC_B) when the beam hits Sample 2A (see Figure 30). There is also a ΔT between the two TCs of about 15-20 °C when the beam is on, where TC_A is higher because it is closer to the beam spot, and ~2 °C when the beam is off, where TC_B is higher because it is located further inside the heater. This temperature difference persists throughout the experiment.

The PIXE data (originally reported in (178)) shows the same sample thinning that was already observed in Exp. 1, but in much more detail (see Figure 31 a)). Gaps in the plot indicate that the spectra taken in those intervals were below the total counts threshold (see Section 4.3.4 and the number of total counts per spectrum in Figure 31b)). The large gap around hour 13 was caused by a loss of beam. Retuning took more than an hour. When the beam was back, the beam energy was accidentally tuned to 4.1 MeV, which was corrected quickly, but created outliers in the PIXE data marked with the rightmost green circle. The increase in Bi-Fe ratios can be understood as more x-rays produced in the LBE since higher energy protons have more residual energy after passing through the sample and penetrate deeper. Even though there are also more Fe x-rays, the number of Bi x-rays increases disproportionately. The other two outliers (also marked with green circles) are due to spikes in the x-ray counts (see green circles in Figure 31 b)) and likely the beam current, which appears to disproportionately affect certain parts of the PIXE spectrum. Based on the standard, Sample 2A was ~38 μm thick at the end of the experiment (thickness estimates from standard shown as horizontal dashed lines).

One thing to note is that the ratios seem to have more spread as they get larger. This seems at odds with the uncertainty of the ratio being dominated by the uncertainty of the much smaller number of Bi counts (compared to Fe) since the variance scales with the inverse of the number of counts. With the increase in Bi x-rays, the uncertainty should decrease despite the decrease in Fe counts because the number of Fe x-rays is orders of magnitude larger. The apparent increase in spread in Figure 31 a) is an illusion created by the linear y-axis. If plotted on a log-scale, the decrease in spread with the increase of Bi counts is immediately apparent (see Figure 32).

Figure 32 shows the same PIXE data as in Figure 31 a) (blue dots). The trendlines in Figure 31 a) show the exponential increase of the ratio before and after the 13-hour gap. Interestingly, if the data is plotted as if the beam was on target continuously (yellow dots in Figure 32), a single exponential trendline can easily be fitted through all data points. This is important because it indicates that the corrosion process had paused or at least significantly slowed down without the beam and resumed when the beam was back on target.

As shown in Figure 26, Sample 2A appeared pristine after the experiment with no signs of oxidation on the vacuum side. The attempt at cutting the sample with a femtosecond laser (see Section 4.2.5) at UCB led to too much heat deposited in the sample and ultimately vaporization and redeposition of the material being cut (see Figure 33). Figure 33 a) shows a FIB-cleaned cross section on Sample 2A after laser-cutting, while b) shows a similar cross section on Sample 2B, the corrosion-only sample. The cross section in a) only shows LBE (original and redeposited) with an Fe-oxide layer detached from the base metal. b) shows some LBE adhering to Sample 2B and the original Fe substrate. There is no immediately obvious oxide layer and the vaporization / redeposition makes it impossible to determine the Fe foil's thickness. At this time, the sample is being shipped back to LANL for further analysis, similar to that performed on Sample 3A (see Section 4.4.4).

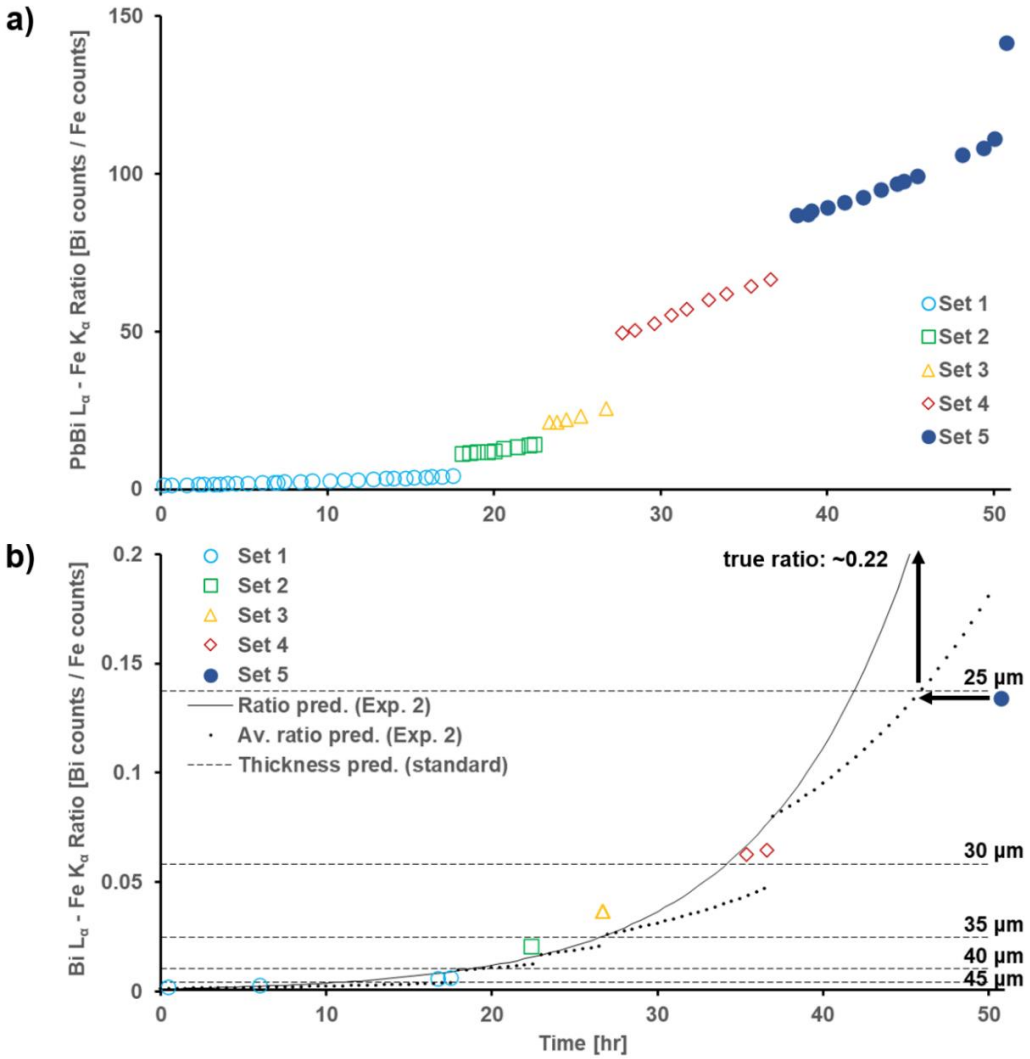

Figure 29 – Attempt at estimating the final thickness of Exp. 1 from (178).

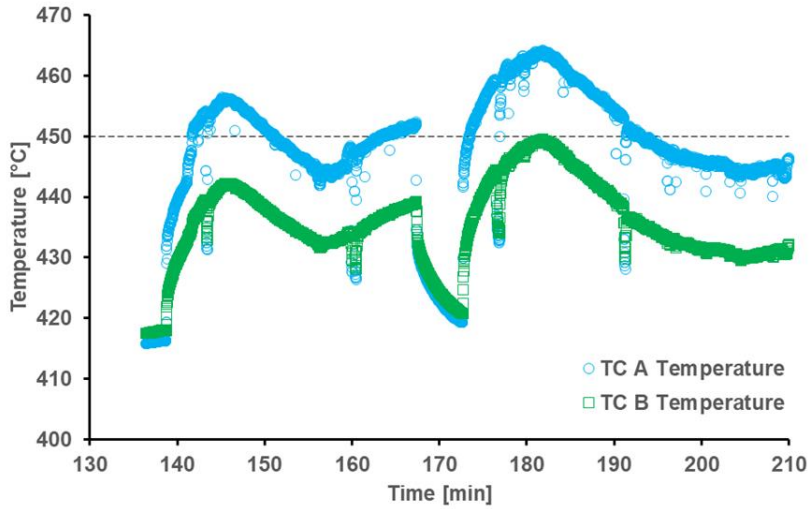

Figure 30 – Temperature measurements from TC_A and TC_B at the beginning of Exp. 2 (time since start).

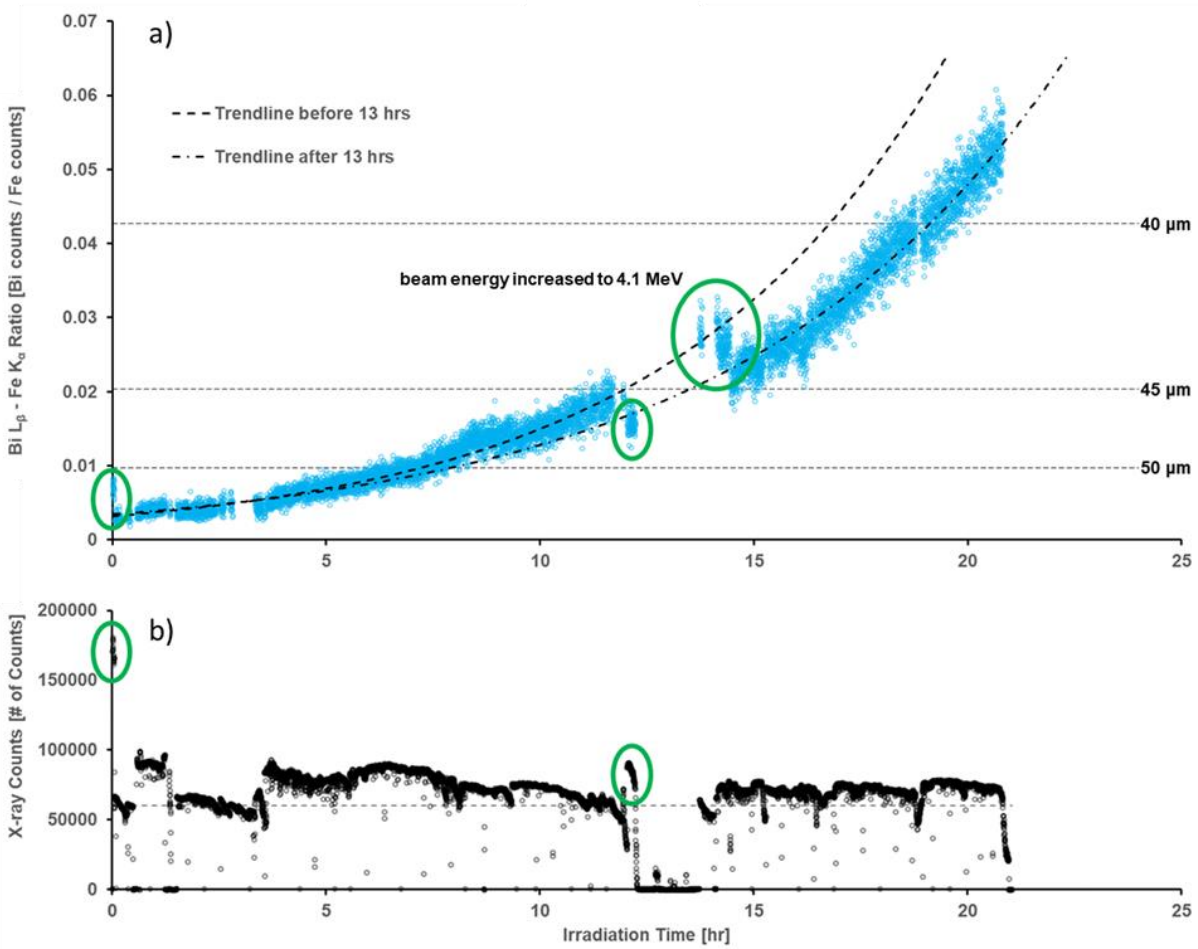

Figure 31 – a) $Bi_{L\beta}$-$Fe_{K\alpha}$ ratios (3-channel method) over the course of Exp. 2 and b) total number of x-ray counts in each spectrum adapted from (178).

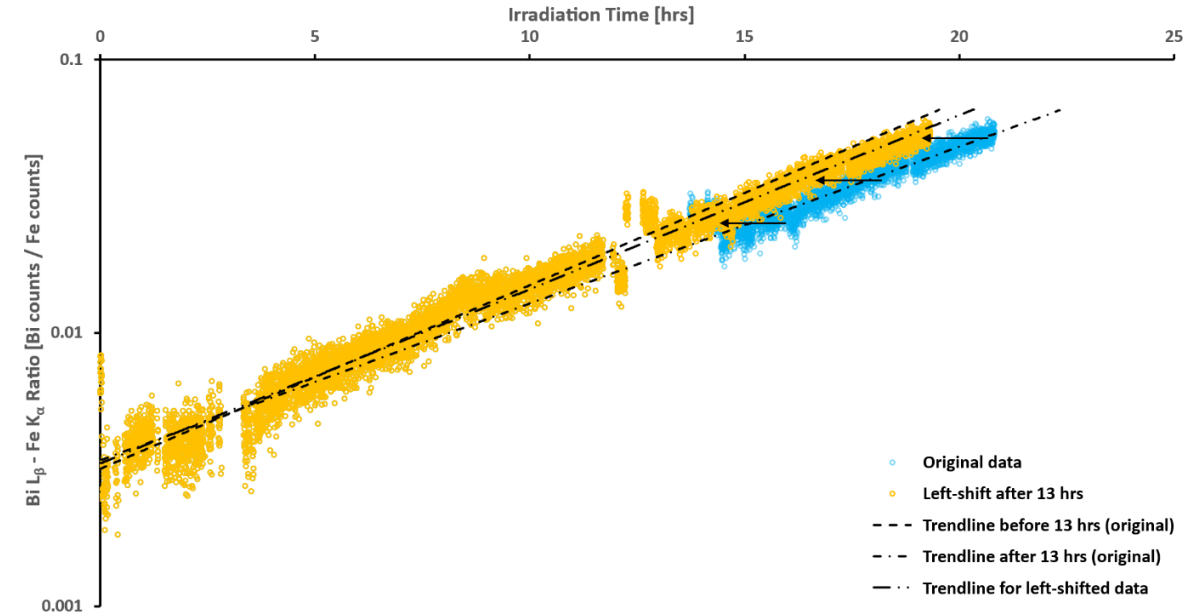

Figure 32 – Log plot of original PIXE ratios (3-channel method) from Exp. 2 (blue dots) and data series with data after the 13-hour mark shifted to the left (yellow dots).

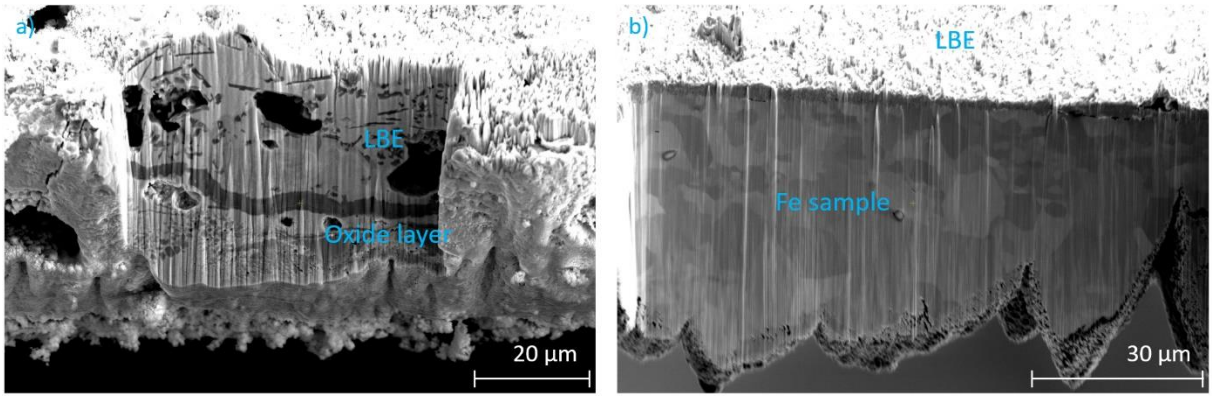

Figure 33 – FIB-cleaned cross sections of laser-cut areas on a) Sample 2A and b) Sample 2B. SEM images courtesy of Peter Hosemann (UCB).

4.4.4. Experiment 3

Exp.3 fills in the duration and dpa gap between the first two experiments. As before, the beam creates temperature fluctuations in the TCs, this time ~15-20 °C for TC_A, ~10 °C for TC_B, and <10 °C between the two (TC_A higher) with the beam on and again ~2 °C (TC_B higher) when the beam is off. Figure 34 shows the PIXE data from Exp. 3 with the trendlines from Exp. 2 overlaid. The initial response for Exp. 3 is quite different, which is possibly due to slightly different initial thicknesses of the Fe foils (±10% according to the manufacturer (175)). Only starting around hour 12 is there better overlap between the lowest trendline in Exp. 2 and Exp. 3. However, that is the trendline that is fitted through the data after the irradiation gap, so, as discussed in the previous section, it is likely not a good representation of the actual irradiation-corrosion behavior of Sample 2A. Therefore, Sample 3A appears to be corroding much more slowly than Sample 2A. Based on the calibration curve (see Figure 23), the final thickness of Sample 3A is ~42 µm, which is similar to the final predicted thickness for Exp. 2 (~38 µm) after approximately twice the corrosion time and dpa. This is more easily seen in the comparison of the calculated sample thicknesses for both experiments shown in Figure 35. To put the results into perspective, the expected sample thickness based on a power-law kinetics model for Fe-oxide formation on pure Fe in O-rich flowing LBE (450 °C) (see (77)) is shown as well. The Fe mass loss Δx_{Fe} can be calculated as follows:

$$\Delta x_{Fe}(t) = \frac{\rho_{Ox} w_{Fe,Ox}}{\rho_{Fe}} \sqrt[n]{k_n t}\,,$$

with the oxide density ρ_{Ox} (here assumed to be magnetite with a density of 5.16 g/cm^3), the Fe mass fraction in the oxide $w_{Fe,Ox}$ (0.724), the density of Fe ρ_{Fe} (7.86 g/cm^3), the exponent n (3.361), the rate constant k_n (2.618 µm/hr), and the corrosion time t in hours (77). By comparison, the corrosion of Samples 2A and 3A is clearly accelerated in the beam spot, as is the corrosion of Sample 3B although to a lesser extent. This discrepancy will be discussed in more detail in Section 5.1.

For the evaluation of the samples from Exp. 3, cross sections were cut into Sample 3A with a PFIB, as described in Section 4.2.5. The observed cross sections show the fate of an oxide layer forming on Fe in LBE (see Figure 36). Initially, the oxide is adherent to the base metal. The oxide shown here is formed by LMC and is not a native oxide because no counterpart is observed on the

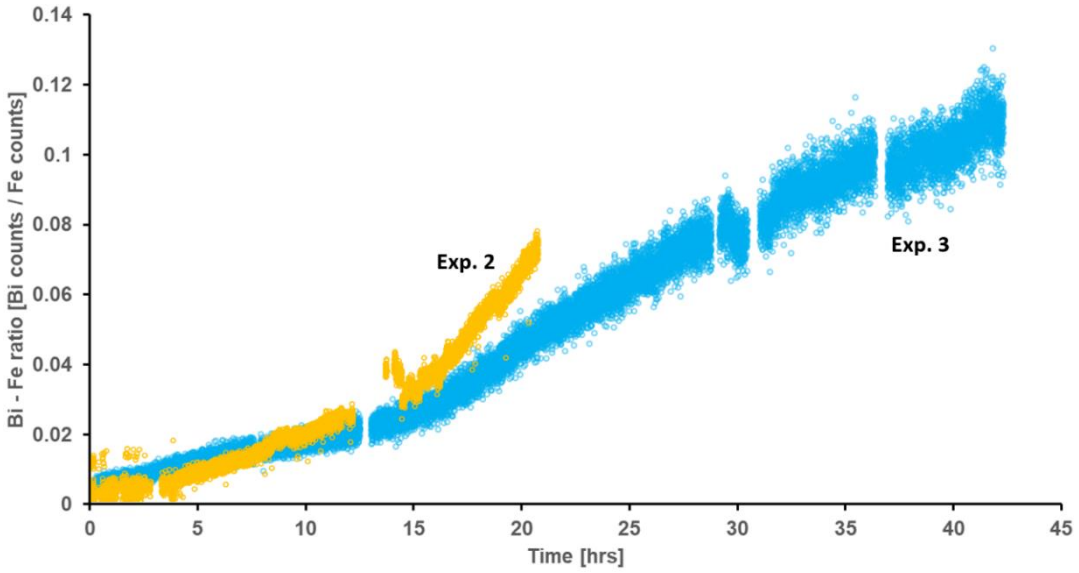

Figure 34 – Linear plot of PIXE results (fitted Gaussians) for Exp. 3 (blue circles) with fitted Gaussian ratios from Exp.2 (yellow circles) overlaid.

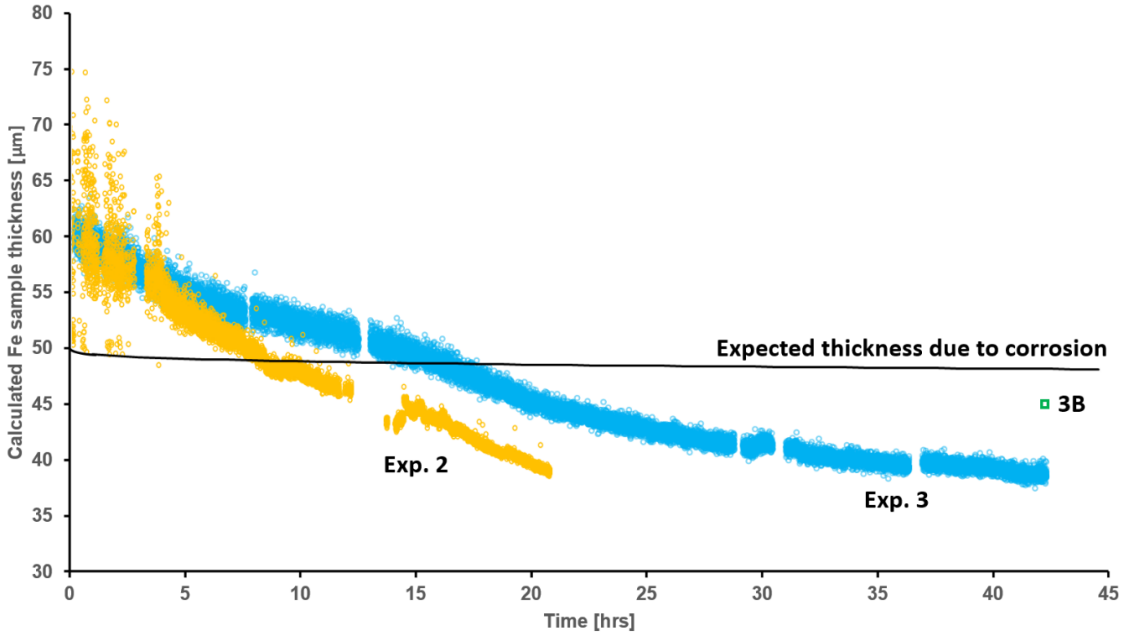

Figure 35 – Calculated sample thicknesses in the beam spot on Samples 2A and 3A based on Gaussian fits and the respective calibration curves for Exp. 2 (yellow circles) and Exp. 3 (blue circles). The black line shows the expected sample thickness based on the power-law corrosion kinetics model presented in (77). An initial sample thickness of 50 µm was assumed for this calculation. The green square shows the average measured thickness of Sample 3B (corrosion-only) after the experiment for comparison.

vacuum side. Over time, the LBE penetrates the oxide and eventually creates pits underneath it (Figure 36 a)). Note that the oxide on top of the pits is thicker than the oxide that still adheres to the sample. The LBE pits grow laterally, but also vertically, i.e., into the base metal. Once two pits meet, the oxide layer is fully detached (b)). The boundaries of the former pits are still visible in both the oxide layer and the Fe layer as (sometimes quite subtle) dents pointing towards one another (best seen in c), but a few can also be observed in b)). The detached oxide layer then slowly

moves away from the base metal as more and more LBE pools underneath it. Over time, the oxide's edges become rougher as the LBE dissolves it from both sides. At this point, the remaining oxide is now thickest at the edges of the dissolution pits where it was attached longest.

Figure 36 c) shows a good example of the oxide and the Fe sample almost mirroring each other in curvature where a corrosion pit started. It also shows a horizontal line connecting the two pit boundaries and stretching further on either side. Its nature and origin are not quite clear although it might be a second-generation oxide that formed after pitting had begun. Multiple generations of oxides can be observed in some areas of the sample (see, e.g., Figure 37). Unfortunately, more detailed images of the oxide are currently difficult to obtain due to the depth of the trench cut by the PFIB. Note that the angle some of the Fe layers appear to be at (as opposed to being horizontal) is a consequence of the sample's local curvature, as discussed in Section 4.2.5. At 0° tilt, the slit appears horizontal.

The numerous cross sections in Sample 3A (a total of 10 trenches, each at least 1 mm wide) were used to measure the thickness of the remaining Fe foil to confirm the PIXE predictions. Measurements were obtained with the tilting method described in Section 4.2.5. The result is shown as a heat map in Figure 38, where red dots show thin (a minimum of 29 μm) and yellow dots show thick cross sections (up to 46 μm). Unsurprisingly, the sample is thinnest in the area surrounded by the white dashed square, which marks the approximate location of the beam spot. Locating the beam spot is challenging because there is no obvious mark on the vacuum side of the sample. The oxidation seen in the photo occurred during cutting of the sample in the PFIB, which indicates that 1 μA is too high of a cutting current (or at least that better thermal contact with the stage is required) and that the Xe beam is introducing substantial amounts of damage into the sample locally. Regardless, the assumed location of the beam spot not only aligns well with the observation of the sample's thickness, but also with observations made during beam positioning. It is directly above the cross, which was added at the end of the experiment to mark the bottom of the sample, so it is well-centered on the vertical axis. It is also slightly above the horizontal center line, which the beam spot generally tends to be with how the beam-guiding scintillators are arranged.

Two more things are important to note about this figure: 1) There are areas far away from the beam spot that are up to 46 μm thick, which is almost the original thickness of the sample and comparable to similar measurements on Sample 3B. These areas have experienced almost no corrosion over the course of ~40 hours. 2) The transition from irradiated to unirradiated areas of the sample is not abrupt, but rather a gradient, which is best seen in the color gradients in the slits at the bottom and bottom left. This shows that the presence of the beam spot induces a bystander effect on neighboring regions that are not directly irradiated.

Attempts were made to take this analysis a step further by obtaining EDS line scans of the cross sections. Unfortunately, the steep angle made it impossible for the EDS detector to measure the number of x-rays consistently with depth, even with depth correction. Within 40-50 μm from the surface, the signal disappears almost entirely, which also makes manual treatment of the data impossible. Therefore, it is desirable to cut the sample in half in the future, ideally with a femtosecond laser at low power, so that the cross sections can be studied in more detail. The nature of the oxide is also not known, although, based on the literature, Fe_3O_4 is the oxide expected to form (77). The oxide's behavior and appearance in cross section also indicates that its Pilling-Bedworth ratio is large and close to 2, which makes it non-protective and is compatible with the assumption that this is indeed magnetite.

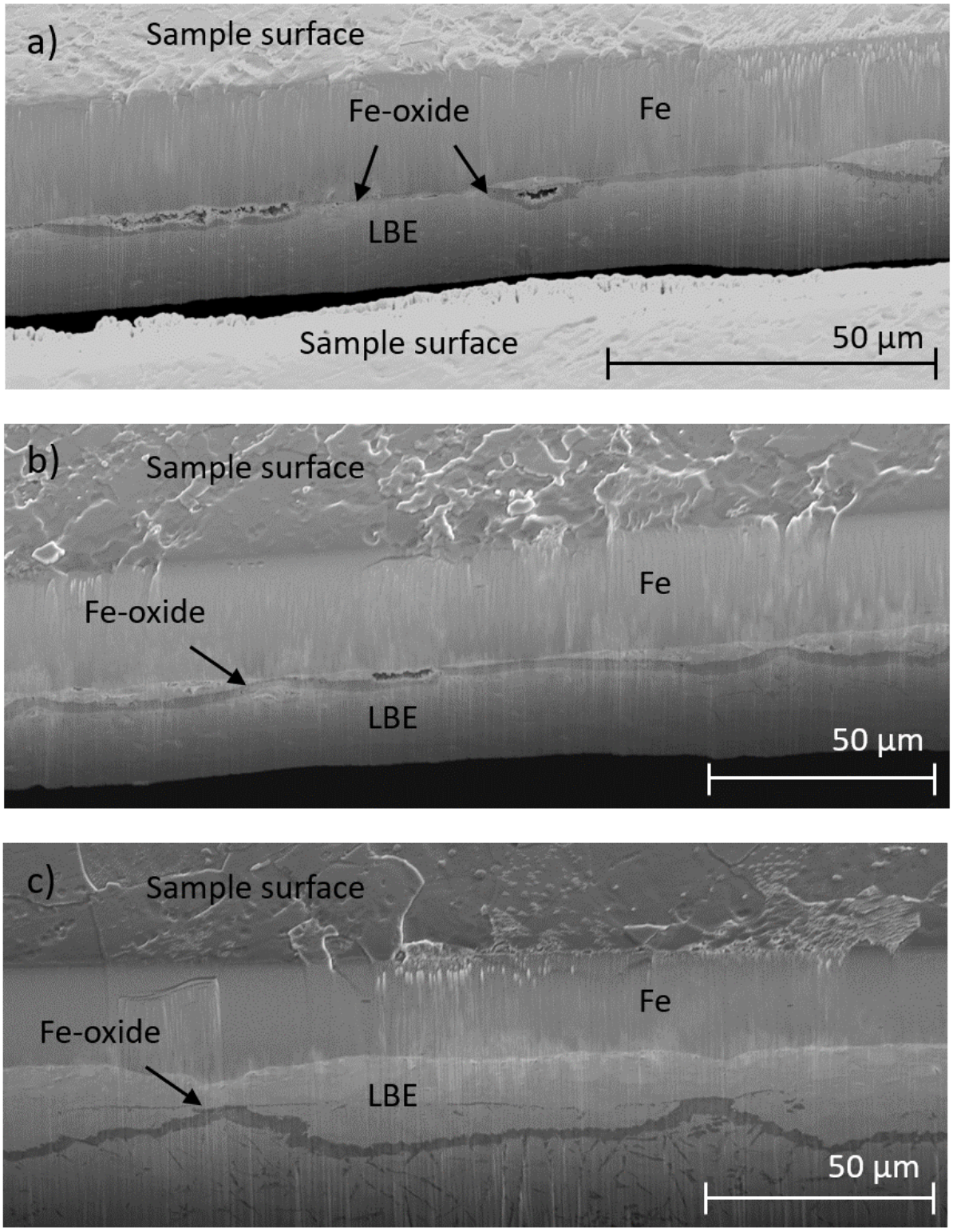

Figure 36 – SEM images showing the progression of corrosion of pure Fe in LBE. All images were taken on Sample 3A. a) was taken at a tilt angle of 15° and shows the onset of pitting corrosion under the oxide. b) and c) were taken at a tilt angle of 45° and show the complete detachment of the oxide from the base metal. Note that the angle at which the Fe surface appears to be is due to the local curvature of the sample, as mentioned in Section 4.2.5. At 0° tilt, the sample surface appears horizontal for all locations shown.

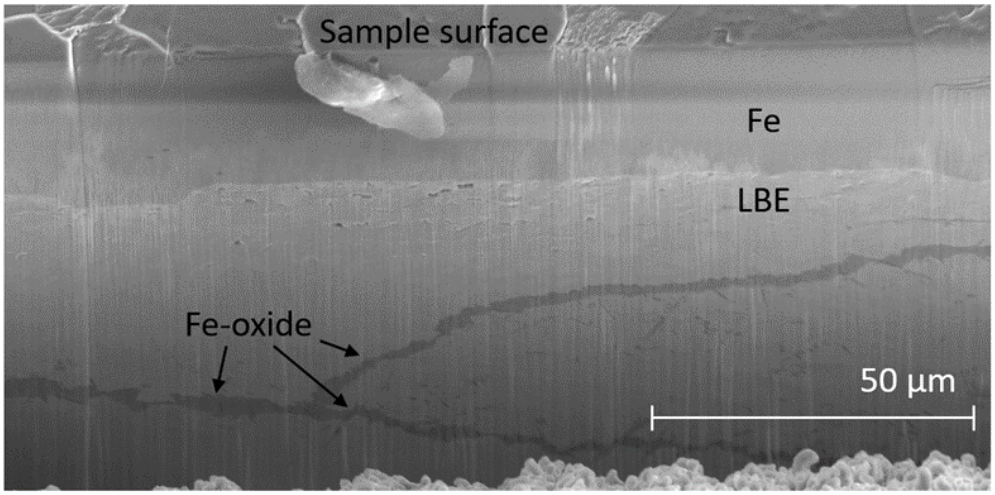

Figure 37 – SEM image (25° tilt angle) showing two generations of oxides connecting to a single oxide layer.

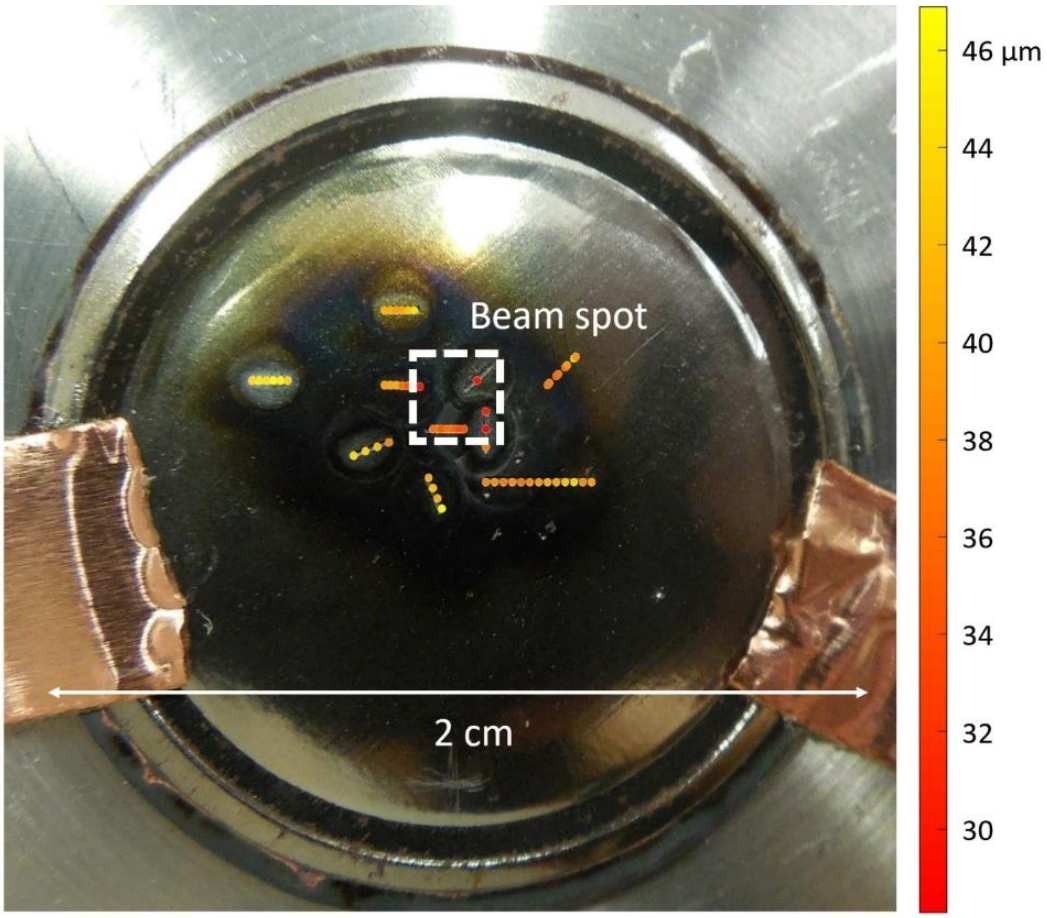

Figure 38 – Heat map of Fe foil thicknesses measured on Sample 3A. Measurement locations are approximate, but data points were obtained in roughly equidistant intervals for each trench.

4.4.5. Interpretation of experimental results

In this section, some discussion of the experimental results of the three ICE III experiments presented above is provided to make it easier to go back and forth between the figures shown here

and their interpretation. Additional discussion of the results in the context of the literature will be provided in the main discussion section (Section 5).

4.4.5.1. Accelerated corrosion under irradiation

This series of experiments has yielded several rather interesting results. The most obvious and most important result is that the proton beam clearly accelerates pure Fe corrosion in LBE. The PIXE data from Exp. 2 showed that corrosion stopped completely or was at least significantly decelerated when the beam was off compared to when the beam was on target. Furthermore, Sample 1A broke after 56 hours and the other two experiments showed substantial thinning in their irradiation-corrosion samples, while the corrosion-only samples were significantly less corroded. In corrosion tests in preparation for ICE III, samples have lasted up to 200 hours in the same corrosion conditions (450 °C) without rupturing. To put this into perspective, in some rare cases, pure Fe exposed to flowing LBE at 450 °C for ~8000 hours has been reported to show no observable signs of corrosion, while other samples in the same experiment showed behavior similar to that shown in Figure 36 (77).

What is less clear is why the thicknesses predicted by PIXE are so close for Exp. 2 and 3, even though the latter was corroded twice as long and exposed to twice the dpa. The only immediate difference between them is that the two experiments show different ΔT when the beam is on, both for the TCs individually as well as between the two (see Table 8). If this was a matter of TC positioning in the chamber, which varies between experiments due to how the TCs are mounted (see Section 4.2.3.2), the TCs likely would have responded differently. For example, assuming that both TCs were closer to Sample A in Exp. 2 than in Exp. 3, the individual ΔTs due to the presence of the beam could be higher in Exp. 2. However, the temperature difference between the two should be similar for both experiments. This is supported by the fact that there even is an observable ΔT in TC_B, which shows how efficient heat transfer within the chamber is because the distance between TC_A and TC_B is much larger (several mm) than any potential error introduced during chamber assembly (< 1 mm). The TC orientation was visually confirmed after each experiment when the chamber was emptied, although the distances were not measured. Therefore, the observation that the individual temperature differences for the TCs are smaller in Exp. 3 even though the same current was measured with the Faraday cup indicates that less beam was on the sample. It appears that during beam positioning, a larger portion of the beam was positioned on the scintillator. However, this does not change the fluence on the sample for the area that was exposed to the beam, which is substantially higher for Exp. 3, and yet the foil thicknesses predicted by PIXE are quite similar. This means that radiation-induced defects alone cannot be responsible for the acceleration of corrosion observed in all three experiments, and so the creation of a ΔT between the beam spot and other parts of the chamber also plays a role in accelerating corrosion here. There may also be a small contribution from the increased number of thermal vacancies in the beam spot due to beam heating.

Table 8 – Summary of temperature differences observed in all three ICE III experiments under different beam conditions.

Condition	ΔT Exp. 1 [°C]	ΔT Exp. 2 [°C]	ΔT Exp. 3 [°C]
TC_A beam on-off	+30	+50	+15-20
TC_B beam on-off	-	+30	+10
TC_A-TC_B beam on	-	+15-20	+<10
TC_A-TC_B beam off	-	-2	-2

On the other hand, it is also clear that a temperature gradient alone cannot be responsible for the observed increase in corrosion rate. As mentioned in the previous paragraph, heat transfer in the chamber is excellent, which is shown by the immediate response of TC_B to beam heating even though this TC is further away from Sample A and well beyond where the protons can penetrate. This implies that not only the region of the beam spot on Sample A, but effectively all of its surface area must be experience an increase in temperature that is much larger than that of Sample B. Yet, as shown in Figure 38, the thickest and thinnest parts of Sample 3A are only mm apart. If beam heating alone was to blame for the observed acceleration of corrosion, the heat map should show a red (thin) area centered on the square 3×3 mm^2 beam spot and a gradient of increasingly more yellow (thicker) data points spreading in all directions away from the beam spot to the edges of the sample. The fact that such a gradient exists in some areas but is quite limited in size, suggests that irradiation-induced defects play a role as well. If they did not, it is not clear why the Fe thickness observed on Sample 3A in some areas less than 5 mm away from the edge of the beam spot is comparable to thicknesses measured on Sample 3B. Another preliminary experimental result supporting the argument that radiation-induced defects have an impact on corrosion of pure Fe in LBE in the dissolution regime will be presented in Section 4.5.2.2). The relative contributions of radiation damage and beam heating, however, remain elusive.

The results of Exp. 2 show that it is not primarily the injection of longer-lived defects by irradiation, but indeed this combination of short-lived non-equilibrium radiation-induced defects and beam heating discussed in the previous paragraphs that produces most of the acceleration of corrosion. This can be seen in the 13-hour-gap, where corrosion effectively ceased because the beam was not present. If there is a contribution of longer-lived non-equilibrium defects to accelerated corrosion, it is very small. Rather, it appears that most of these defects are annealed shortly after irradiation stops. This observation underlines the need for simultaneous irradiation-corrosion experiments, such as those presented in this work, as opposed to corrosion experiments with pre-irradiated samples.

One important question remains, and that is whether the beam primarily affects the metal or the oxide. In the later stages of the corrosion process, when the oxide is fully detached, the answer seems obvious, since there is no oxide that can contribute. However, when the oxide is still adherent, the answer is not that clear-cut. It is possible that the introduction of defects into the oxide and the disruption of bonds within it makes the oxide even more easily penetrable than it already is under corrosion-only conditions. A similar argument was recently made for oxides on SIMP steel, a martensitic steel under simultaneous irradiation by 247 MeV Ar and corrosion by flowing LBE (151). The defects introduced into the base metal likely contribute as well. A recent study on irradiated Fe capped with Fe_2O_3 showed that defects from the metal accumulate at the interface with the oxide (192). From a corrosion perspective, this makes the oxide less adherent and accelerates its detachment. Therefore, it appears that radiation-induced defects in both the base metal and the oxide may play a role in accelerating corrosion of pure Fe in LBE, but – once again – the relative importance of the two effects is not immediately obvious.

4.4.5.2. Accuracy of PIXE predictions

The quality of the PIXE data merits some discussion as well. The comparison of the PIXE results and SEM measurements for Sample 3A shows reasonable agreement between the predicted (~42 μm) and observed (~35 μm on average) Fe foil thicknesses. This shows that PIXE is a rather useful tool for the in-situ monitoring of corrosion under simultaneous proton irradiation over time, even though the PIXE response measured is an average of the entire area of the beam spot. One of

the reasons for why PIXE works so well for the prediction of sample thicknesses is that the corrosion of Fe in LBE is relatively uniform. If corrosion was extremely non-uniform, e.g., if it was dominated by highly directional grain boundary attack (see, e.g., (193) for such an example in molten salt), a calibration curve like that established here cannot be applied. However, even in non-uniform cases, PIXE may yield useful results. For example, if x-rays from an element in the molten salt become measurable over the course of the experiment, the depth of corrosion along the grain boundary could be inferred. In addition, it serves as an early warning sign for runaway corrosion if peaks from the corrosive medium grow very quickly, at which point the experiment should be terminated.

The discrepancies between the PIXE results and the SEM measurements are worth discussing in a bit more detail. Figure 35 shows that PIXE significantly overestimates the sample's initial thickness (more than 60 µm, compared to the nominal thickness of 50 µm +/- 10% according to the manufacturer). Based on the SEM results for Exp. 3, this discrepancy becomes smaller over time (> 10 µm initially compared to ~7 µm at the end of the experiment), which is probably a consequence of the improved counting statistics of the $Bi_{L\beta}$ x-ray peak as Sample A thins out. This indicates that the final thicknesses of Sample 1A and Sample 2A predicted by PIXE are likely overestimated by several µm as well. Unfortunately, this assumption can no longer be proven directly with microscopy due to the destruction of the samples.

The comparison of the calibration curve ratios computed by the 3-channel method and by Gaussian peak fitting (see Figure 25) shows a systematic shift towards larger Bi-Fe ratios for the same sample thickness. However, this shift is also reflected in PIXE ratios collected during ICE runs. Note, for example, the difference in ratios from Exp. 2 between the 3-channel method (Figure 31 a)) and the larger ratios obtained by Gaussian fitting (Figure 34). This shift reflects the smaller height-to-width ratio of the Gaussian fitted to the $Bi_{L\beta}$ peak compared to the much narrower 3-channel "fit". As a result, the Gaussians cover a larger number of channels and therefore account for a larger area under the curve than the 3-channel method, which disproportionately affects the $Bi_{L\beta}$ peak (see energy difference between $Bi_{L\beta1}$ and $Bi_{L\beta2}$ vs. $Fe_{K\alpha1}$ and $Fe_{K\alpha2}$ in Table 11 in Appendix 8.4), and therefore increases the Bi-Fe ratio.

Another potential source of error resulting from the use of the calibration curve stems from the curve fit to the calibration curve data points. As shown in Figure 23 and Figure 24, the curve sometimes over- or underestimates a cluster of ratios at a given Fe stack thickness. At 50 µm, the curve overestimates the ratio for both Exp. 2 and Exp. 3. This results in an overestimate of the predicted initial thickness during the experiments of ~2 µm when compared to predictions based on the average ratio for 50 µm measured for the calibration curve. This may also hint at a discrepancy between the fit applied to obtain the calibration curve and the actual Bi/Fe ratio at large Fe foil thicknesses. The sample thickness before the experiment has been measured in the SEM to be between 52 and 55 µm, so it is indeed thicker than the expected 50 µm. It is possible that the Bi/Fe ratio for 55 µm of Fe is substantially lower than estimated by the exponential fit assumed in the calibration curves. This may explain why the extrapolation to Fe thicknesses larger than 50 µm yields surprisingly large sample thicknesses initially and should be confirmed with 55 and 60 µm thick Fe foil stacks during another calibration curve measurement. This does not, however, explain the mismatch between PIXE data and SEM observations later in the experiment where the Fe sample thickness is well within the range of the calibration curve.

Therefore, the remaining observed discrepancies are likely due to systematic differences between the ratios in the calibration curve and the ICE runs. One obvious difference is that the calibration curve is measured at room temperature, while ICE is at 450 °C. The resulting density

difference (10.5 g/cm^3 vs. ~10.1 g/cm^3), however, results in a rather small (~0.3 μm) overestimate of the Fe foil thickness during the experiment. Other differences include that the calibration curves are measured using smaller proton currents (1-2 μA vs. 3 μA) on a smaller area (2x2 mm^2 vs. 3x3 mm^2) compared to ICE runs; that the LBE tablet holder has a small opening that contributes additional steel background compared to ICE; and that the beam-guiding alumina scintillator and the Cu tape it is mounted on are present only during ICE.

Another potential source of error stems from the presence of Fe in the oxide as well as in solution in LBE near the sample surface during ICE. The Fe x-rays from Fe in these regions will count towards the total Fe counts and slightly distort the Fe thickness estimate. However, the lower density of Fe-oxides compared to pure Fe and the small amount of Fe soluble in LBE at 450 °C (see Figure 2) implies that this contribution is rather small. At the beginning of the experiment, the growth of an Fe-oxide or the dissolution of Fe should, in fact, have the opposite effect on PIXE predictions, i.e., the sample should appear thinner due to the smaller number of Fe atoms per volume compared to pure Fe.

It is not quite clear what the individual contributions of these differences are. Some factors, such as the higher beam current during ICE, even indicate that ICE PIXE ratios should be an underestimate of the Fe foil thickness rather than an overestimate because disproportionately more Fe counts may be lost to pile-up and escape peaks. Detailed parametric studies are required to illuminate this issue and to make the PIXE predictions more accurate. Nonetheless, even in its current form, PIXE provides a powerful tool for the observation of corrosion under irradiation.

4.5. Extensions of the Irradiation-Corrosion Experiment III

4.5.1. Molten salt setup

Another group of Gen-IV reactor-relevant coolants consists of molten salts, specifically chlorides and fluorides, that are used as either fuel solvent, coolant, or both (see e.g., the Molten Salt Reactor Experiment (MSRE), the Molten Salt Actinide Recycler and Transmuter (MOSART), the Thorium Molten Salt Reactor (TMSR), the Molten Salt Fast Reactor (MSFR) (194), and the Fluoride-salt-cooled High-temperature Reactor (FHR) (195, 196)). In molten salt cooled reactors, the protection of structural materials relies on the reduction of dissolution corrosion by controlling the redox potential of the salt rather than the formation of an oxide since these are generally not stable (see, e.g., (197)). Corrosion resistance for species commonly found in structural materials is in a different order for molten salts ($Ni > Fe > Cr$) compared to HLMs ($Fe > Cr > Ni$).

ICE III was designed with the intent to also accommodate molten salts to study the dissolution of materials under simultaneous corrosion. However, there are major differences between the LBE and molten salt experiments. The salts have higher melting points and therefore require higher temperatures during the corrosion experiments. While Cu gaskets have not led to issues at 450 °C, they are increasingly more likely to diffusion-bond with the knife edge at higher temperatures, so they are replaced by Ni gaskets. Corrosion behavior in molten salts is very sensitive to salt purity and many molten salt coolant candidates are hygroscopic or deliquescent, so handling and filling of the chamber must occur in a well-controlled environment. In addition, the chamber must be fully sealed, which includes welding the Swagelok adapter holes shut. This implies that in order to fill the regular ICE III chamber design with salt, salt powder has to be densely packed into the main chamber, which will likely lead to a large plenum above the liquid, as was seen in Figure 12. The presence of such a large gas space can likely not be avoided, but it is desirable to keep it as small as possible to avoid changes in salt chemistry due to the segregation of more volatile species

into the gas phase. Dense packing is challenging with two TCs in the middle of the chamber, so a slightly different design is used for molten salts, which is described in Section 4.5.1.1. Testing is described in Sections 4.5.1.2, 4.5.1.3, and 4.5.1.4.

4.5.1.1. Molten salt ICE chamber

The purpose of the molten salt ICE III chamber design is to ensure that enough salt is present independently of the chamber's internal geometric complexity, e.g., due to the presence of TCs. There are two additional goals: 1) to have an irradiation-corrosion setup for rare salts, e.g., UCl_3, where using a large chamber would be prohibitively expensive; and 2) to add more access ports, e.g., for electrodes for electrochemical measurements. A design that meets all these constraints is shown in Figure 39. The center port is used as the salt powder reservoir, while the other two ports can be used for TCs or electrodes. Since the salt volume is rather small, the experiment time needs to be relatively short, so that the salt does not saturate with corrosion products.

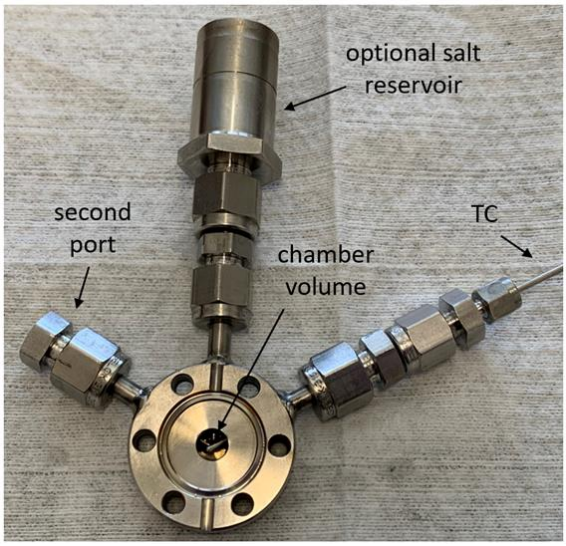

Figure 39 – Photo of molten salt chamber for rare salts (courtesy of Scott Parker (LANL)).

4.5.1.2. Corrosion test

A leak test was conducted with a DN16CF flange with a pocket (machined by Scott Parker (LANL)), similar to the molten salt ICE chamber. The test sample was a 50 μm thick AISI 304 foil and the corrosive medium was $0.52MgCl_2$-$0.48NaCl$ (T_{melt} = 450 °C), which is close to the eutectic composition of the $MgCl_2$-NaCl system. NaCl-$MgCl_2$ is one of the candidate solvents for liquid-fueled MCFRs (194). AISI 304 was selected because it should be more corrosion-resistant than pure Fe, but not as corrosion-resistant as Ni-based alloys. It is also chemically similar to the chamber materials, which is desirable for corrosion experiments (see, e.g., (154) and Section 4.5.2.2). The goal for this experiment, the subsequent irradiation test (see Section 4.5.1.4), and future ICE runs is to increase the likelihood of measurable corrosion occurring while preventing immediate failure of a less durable sample, such as pure Fe or pure Ni under irradiation (see (176)). This should allow possible effects of radiation on corrosion to be observed in a relatively well-controlled environment before moving on to other sample materials.

Approximately 14 g of salt were packed into the chamber and sealed with a Ni gasket by Scott Parker (LANL). The assembly was then heated to 760 °C in a furnace inside a glovebox with the

sample facing down. The test lasted for ~10 days with a 1-day break after 3 days, after which heating continued in a different furnace provided by Charles Lhermitte (LANL). No salt leak occurred, and the cross section of the sample revealed no substantial corrosion.

4.5.1.3. Corrosion monitoring demonstration with solid salt tablet

The first step in establishing whether PIXE is feasible for molten salts was to attempt a measurement of solid salt behind Fe foil stacks of varying thickness, similar to the LBE calibration curve measurement described in Section 4.3.3. The tablet was made by mixing and grinding food-grade NaCl and KCl (~50% each), wetting the stamp with water, and pressing the powder into a wetted pellet by hand to fuse the powder grains by partially dissolving and then recrystallizing them. With the wet pellet method, the surface of the pellet was flat and cohesive without additional processing, which allowed it to be mounted vertically in the beamline.

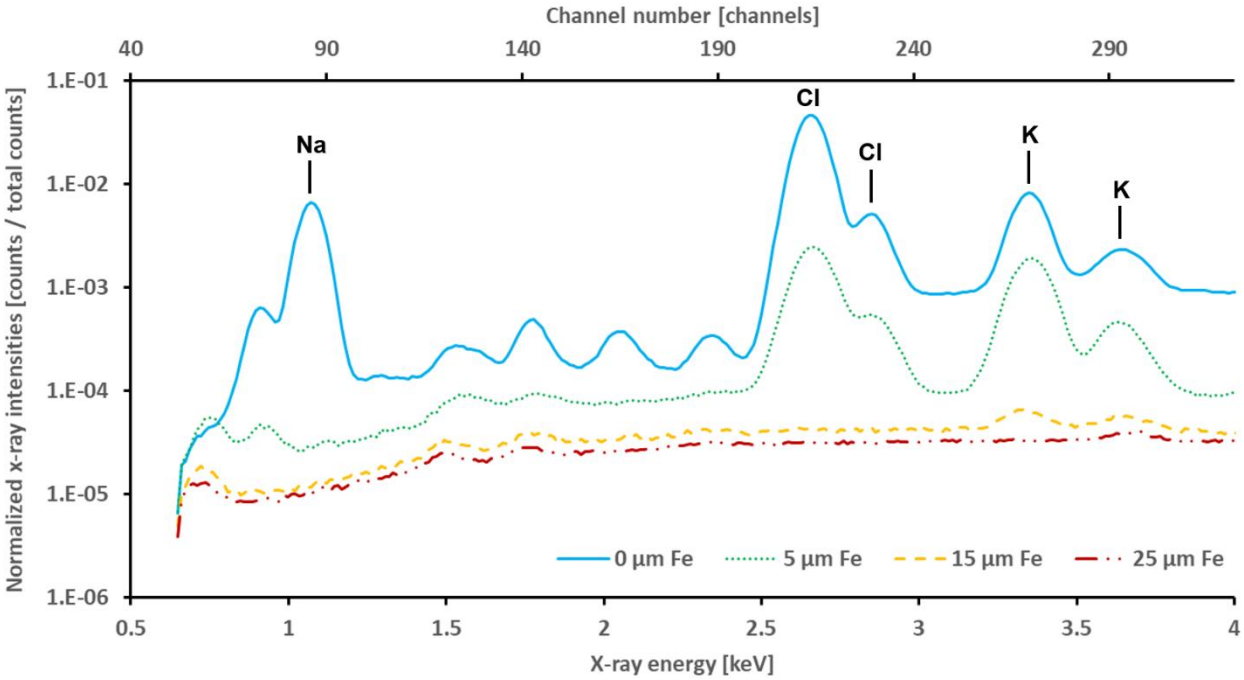

Figure 40 – Qualitative comparison of normalized PIXE data from solid salt tablet test. X-ray peaks from the salt are easily visible until the Fe thickness reaches 25 µm, at which point the $K_{K\beta}$ peak is the last remaining barely observable salt peak. Measurements for the bare salt tablet were taken for 500 nA of 1.5 MeV protons (2x2 mm^2 beam spot size) to reduce the risk of the tablet melting. Measurements with Fe present were done with 4 MeV protons and currents of 340, 320, and 300 nA for 5, 15, and 25 µm thick Fe, respectively.

Figure 40 shows normalized PIXE results for proton irradiation of the salt tablet with Fe foil stacks up to 25 µm thick. Beyond this thickness, none of the elements present in the salt were detectable. It is important to note that the density of the produced tablet is unknown and likely smaller than that of a pure molten salt, which means that it may be possible to observe certain molten salt x-rays with samples slightly thicker than 25 µm. However, these results serve as an indication of the maximum sample thickness that is likely to be suitable for molten salt PIXE.

Another interesting thing to note is that salt constituents down to energies of ~1 keV can be detected (detector temperature during test: 265 K). This is encouraging, and it may even be possible to measure these x-rays during a real experiment if the detector is actively cooled.

One possible alternative to establishing PIXE ratios, which requires signal from the corrosive medium, is to monitor only the x-rays of the sample, which should change over time as it is corroded. However, this requires the presence of a constant peak that can be used to monitor the beam current, which is challenging, as mentioned in Section 4.2.10.3. In addition, if a steel is used as the sample, it needs to be distinguishable from the steel background in the end station. To remove this background, Ti parts (sheet and tubing, Titanium Joe) may be used to cover these steel parts on the vacuum side and replace the steel background with a Ti background that does not overlap with signal from the sample.

Another alternative to PIXE ratios is to use PIGE (see Section 4.3.5.2) to detect the 1219 keV γ-rays from the $^{35}Cl(p,p'\gamma)$ reaction. ^{35}Cl is 76% naturally abundant, but the cross section for this reaction drops drastically with low proton energies, so higher energies (~3.5 MeV in the salt, see (188), and therefore more than 4 MeV to begin with) are needed, which would lead to more activation of the sample.

4.5.1.4. Irradiation test

Since all LBE-ICE III experiments were conducted with 50 μm thick Fe foils, an irradiation-corrosion test with $0.52MgCl_2$-0.48NaCl and a 25 μm thick AISI 304 sample – as suggested by the salt tablet demonstration – was conducted to ensure beamline safety. This was done with the help of Matt Chancey (LANL). The goal was to determine which beam currents the sample can withstand and what kind of ΔT (beam on-off) may be expected on TC_A, given that the salt volume is significantly smaller than in regular ICE. In addition, the heat transfer coefficient of molten NaCl-$MgCl_2$ is much lower than that of LBE. The proton beam energy for the test was set to 2.75 MeV, which places the Bragg peak in the corrosive medium, while producing a relatively flat exposure profile in the sample.

The temperatures recorded by TC_A (the only TC for this setup) are shown in Figure 41. Beam currents as low as 500 nA lead to temperature increases of 10s of °C, which means that, if beam heating is to be avoided, a current of ~250 nA or less is appropriate, especially if higher proton energies (up to 4 MeV) are used to increase the chance of obtaining a PIXE signal from the molten salt. Note that Figure 41 shows a temperature decrease for some currents even though the beam is on the sample continuously. This is due to adjustments of the heater temperature, which are not shown here, to restore the chamber temperature to the target of 500 °C. The decrease in heater power causes the chamber temperature to drop below the melting point before the 1.7 μA and 3 μA tests. Obviously, an actual irradiation-corrosion experiment should be run well above the melting point, so that solidification of the corrosive medium does not occur (unless the goal is to arrest corrosion in the absence of irradiation). This was primarily done to determine the stability of the sample, which was warped in the beam spot after the experiment, but otherwise still intact. With this, the stage is set for a real molten salt experiment in ICE III.

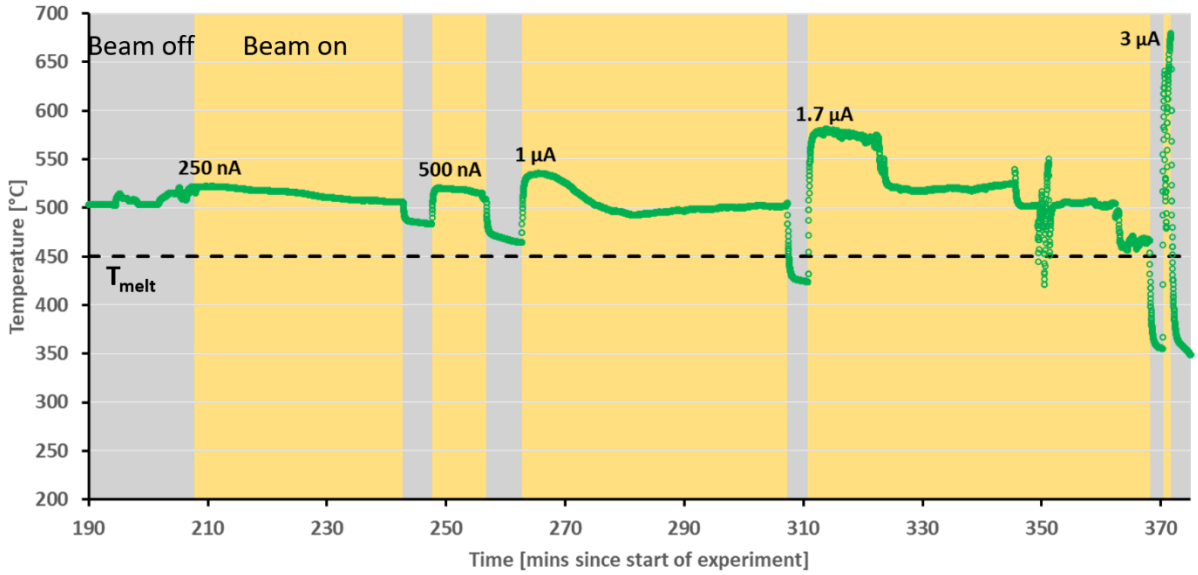

Figure 41 – Temperature response of molten salt chamber to different beam currents.

4.5.2. Accelerated testing of materials under simultaneous proton irradiation and LBE corrosion with Tiny ICE

One of the shortcomings of the ICE III designs presented so far is that sample evaluation still takes relatively long due to activation, even though activation has been reduced substantially compared to its predecessor ICE II. The only way to reduce it further is to reduce the beam energy further, which requires even thinner samples. With large amounts of corrosive medium present in the chamber and while under irradiation, it seems obvious that a foil even thinner than 25 µm cannot survive for long and puts the beamline at risk for contamination and exposure to gases from inside the chamber. One solution is to reduce the volume of the corrosive medium, which requires a reduction of the experimental duration to prevent saturation of the liquid.

The other issue with thinner samples is availability. Certain metals and metal alloys are commercially available as free-standing foils of a few µm thickness but many are only available as thicker bulk materials. To study the irradiation-corrosion response of binary or ternary model alloys as a function of composition, many different compositions need to be readily available. One method of producing samples of well-controlled and readily achievable composition is to use PVD for thin-film deposition on a substrate, which can be exposed to simultaneous irradiation and corrosion conditions.

An approach using smaller samples and smaller corrosion chambers may also alleviate another issue seen with the ICE results presented in this work: the variability of experimental outcomes due to unintended variations in the setup of each experiment, such as the observed differences in ΔT across the chamber. While the highly detailed PIXE and temperature measurements taken during the experiments help tremendously with disentangling those variables, a larger sample size and repeated trials would increase confidence in the interpretation of the results.

This section describes a novel approach to irradiation-corrosion experiments where a thin-film of arbitrary composition is deposited directly onto a solid LBE surface. A single deposition could produce tens of these so-called Tiny-ICE "chambers". These chambers are heated on a heater stage and exposed to very low-energy proton beams ($\geq$ 200 keV) to keep activation and beam heating low, which should allow for the inherent separation of radiation-induced effects on

corrosion from beam heating. An added benefit is that accelerators producing low-energy protons tend to be more available and have fewer safety requirements compared to higher-voltage accelerators.

4.5.2.1. Experiment preparation and thin-film growth

5x5x3 mm^3 stainless steel sample holders / corrosion chambers were machined by Marshall Maez (LANL). Each holder has a 1-2 mm deep ~0.9 mm diameter hole. These holes were filled with small pieces of LBE and hand-polished once the LBE has solidified. The LBE pieces were made by dipping a cold steel needle into molten LBE. Once enough solid LBE was placed near the hole, the holders were heated and the LBE pressed into the hole as it liquefied. This process is tedious because LBE has rather high surface tension that prevents immediate wetting of the cavity. Polishing of the surface was also challenging due to the difference in hardness between steel and LBE. The most practical method was found to be pre-polishing of the steel holders to decrease their surface roughness before filling them with LBE.

Once a reasonably flat surface was achieved, 800 nm of pure Fe were deposited via PVD at room temperature and without bias by Ben Derby (LANL). RBS measurements performed by Yong Wang (LANL) on the Si witness sample showed that the resulting film had approximately 11% porosity, which is likely due to the low deposition temperature. Unfortunately, the low melting point of LBE prevents the use of more appropriate higher temperatures. The result is a nanocrystalline film covering the entire surface of the sample holder (see Figure 42 a)). Clearly, the hand-polishing left marks on the surface that carry over into the thin-film. However, they also act as scoring marks along which the film can tear once heated, relieving stresses building up in the film as the LBE expands. This can be seen in Figure 42 b), which shows Fe thin-film pieces floating on now frozen LBE, which expanded after 1 hour at 500 °C.

4.5.2.2. Experimental results and discussion

18 Tiny-ICE chambers were produced for this work and were used for various purposes in addition to irradiation-corrosion experiments, such as heating tests on the high-temperature stage. Initially, there were concerns that the thin-films may not survive extended periods of corrosion and that the LBE may flow out of the chamber since the sample holders have to be tilted 90° during irradiation. Several corrosion tests at different temperatures showed that the LBE generally stays in place due to its high surface tension. Thin-films are lost occasionally, which likely happens during the cooldown phase at the end of the experiment. It appears that the contraction of the LBE upon cooling creates a gap between its surface and the thin-film. The corrosion test results also showed that variability in film appearance after the experiment can be quite high, underscoring the need for repeat trials.

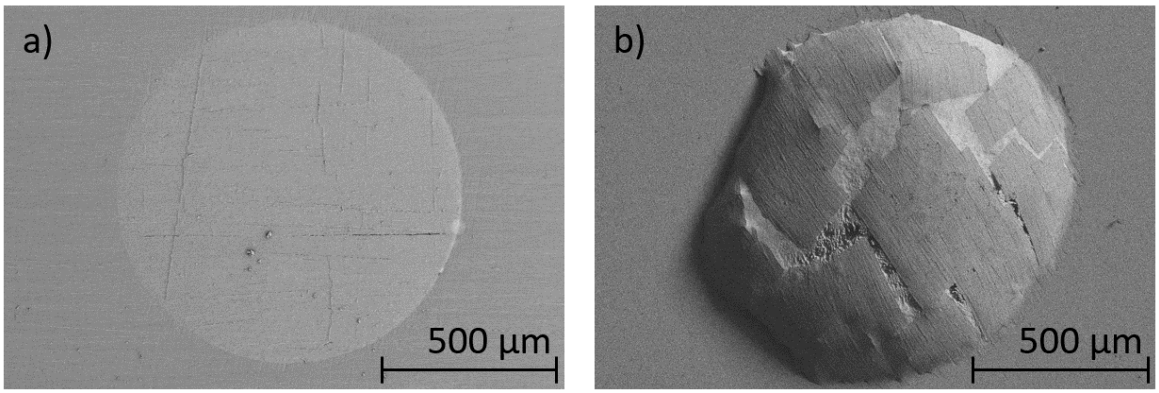

Figure 42 – 800 nm thick Fe thin-film grown on LBE (light) and steel (dark) a) before and b) after 1 hour at 500 °C.

Two samples were ultimately used for the irradiation-corrosion experiment and two for a corrosion experiment with a nearly identical temperature history. The irradiation was performed by Yong Wang (LANL) on a 200 kV Danfysik ion implanter at the IBML. The samples were held at 450 °C and irradiated with a rastered beam of 200 keV protons for ~10.5 hours (8.86×10^{16} H/cm^2, ~0.19 dpa at 800 nm depth). A bare TC was mounted next to the samples on the high-temperature stage and exposed to the beam. No radiation-induced heating was observed. After the experiment, TEM lift-outs of one irradiation-corrosion sample and one corrosion-only sample were prepared with a FIB (FEI Helios NanoLab 600 DualBeam FIB, (EML, LANL)) by Hyosim Kim (LANL). A comparison of remaining thin-film thicknesses on these lift-outs is shown in Figure 43. Measurements are sorted by increasing thickness and show that the corrosion-only sample is tens of nm thicker than the irradiation-corrosion sample although there is a substantial amount of overlap between the two.

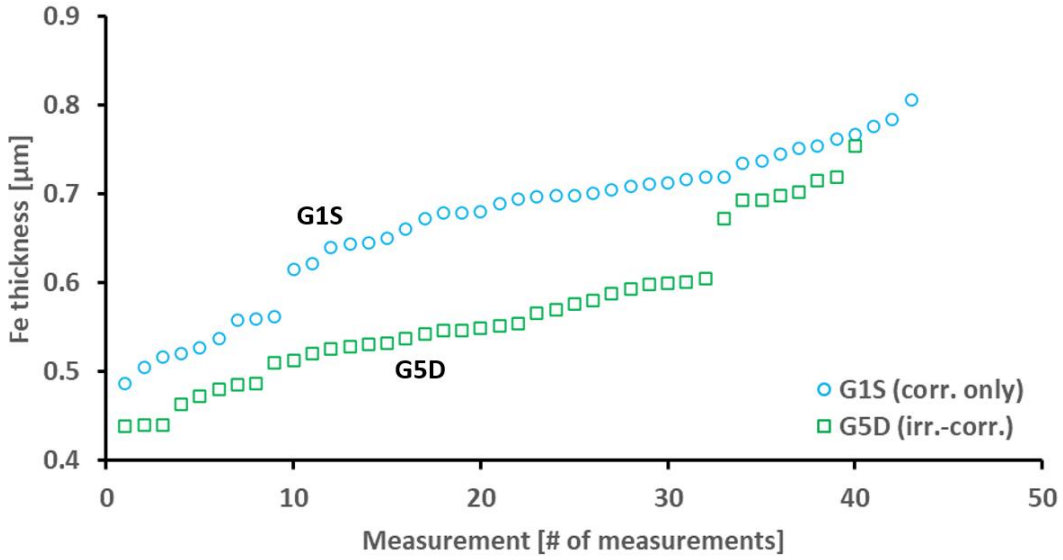

Figure 43 – Fe thin-film thickness measurements on two TEM lift-outs (irradiation-corrosion vs. corrosion-only).

One interesting observation common to all lift-outs of corroded Fe thin-films is the presence of a Ni-Bi phase underneath the thin-film (see Figure 44). Since an austenitic stainless steel was used as the sample holder, the LBE likely leached Ni from it. It is not clear if this deposition occurred during the experiment or the final cooldown phase. The icicle-like shape may indicate a

crystallization process during cooldown. The thin-film is farthest away from the heating stage and therefore the coolest surface, which may be why crystallization occurred there. If the deposition did not occur during the experiment, it should have no impact on the comparison of irradiation-corrosion and corrosion-only results. However, to exclude the possibility of Ni's influence, future experiments will be conducted with 98% Fe (rod, from Goodfellow) as the sample holder material.

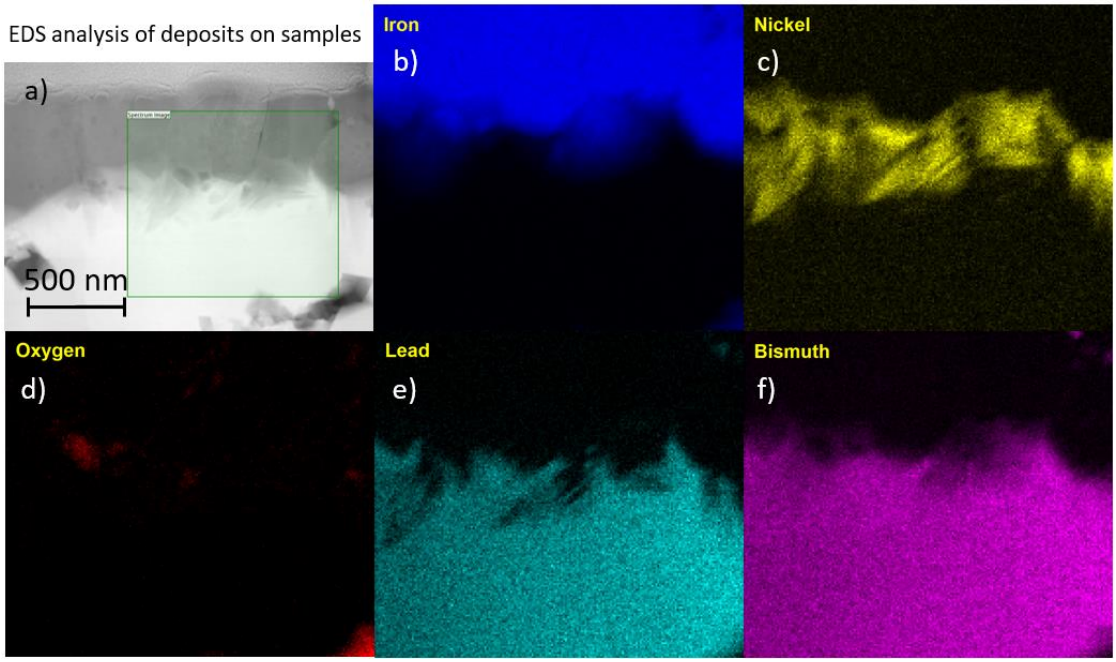

Figure 44 – EDS maps showing Ni-Bi phase deposits in LBE under an Fe thin-film in Tiny-ICE. Maps were obtained by Hyosim Kim (LANL) on an FEI Tecnai TEM (EML, LANL).

The tearing of the thin-films implies that the LBE is not separated from the vacuum in the accelerator. As a result, dissolved O is likely lost to the vacuum and corrosion is dominated by Fe dissolution. To study samples under irradiation in an oxide-forming corrosion environment with the Tiny-ICE setup, the chamber must be sealed in some way. In addition to the equilibrium concentration of dissolved O established during LBE loading, a second source of O, such as PbO or Bi_2O_3, is likely required to maintain O concentrations above the dissolution regime for a given experiment temperature. However, even in its current form, the preliminary results presented here are rather promising for the future use of Tiny-ICE chambers for the accelerated testing of various materials compositions under irradiation-corrosion conditions on lower-voltage accelerators that are often more readily available.

5. Discussion

Some discussion of the individual results is provided with the description of each experiment in Section 4. In this section, the validity of the experimental parameters is discussed based on a comparison of the experimental results with some of the existing LBE corrosion literature. Then, an attempt is made to combine the various competing processes into a mechanistic description of Fe corrosion in LBE under simultaneous proton irradiation. Finally, some advantages and disadvantages of the presented experimental approaches are reiterated and the need for in situ monitoring methods and a better understanding of model materials is stressed.

5.1. Replication of relevant experimental conditions and sample behavior with ICE III

Studies of pure Fe corrosion in LBE are relatively scarce in the literature and currently, there appear to be none considering the added impact of irradiation on Fe corrosion, aside from (178), in which some of the results presented here are reported. In this section, the experimental results from ICE III will be discussed in the context of available data on Fe corrosion. In addition, some discussion of other irradiation-corrosion studies in LBE will be provided in this and the following section, which will focus on the mechanistic aspects of irradiation-corrosion processes.

5.1.1. Corrosion mode

The prevalence of oxide-formation or dissolution attack for pure Fe in LBE is largely determined by the temperature and the dissolved O content of the system (see Section 3.2.1.2). Thick spalling oxide layers on pure Fe have been observed after 3000 hours of corrosion in a static setup at 450 and 550 °C with an assumed dissolved O concentration of 3.2×10^{-4} and 1.2×10^{-3} wt%, respectively (82). A thinner magnetite layer combined with dissolution attack was observed on pure Fe in LBE with 5×10^{-8} wt% dissolved O at 450 °C (198), which is near the stoichiometric line for Fe_3O_4 (see Figure 4). At 550 °C and with 3×10^{-9} wt% dissolved O, which is in the dissolution regime, only dissolution was observed on pure Fe (198). Pure Fe (98%) samples exposed to flowing LBE (2 m/s, 450 °C, 1.1×10^{-6} wt% dissolved O) in the CORRIDA loop for up to 8000 hours exhibited a mixed corrosion mode with magnetite covering the sample surface and locally occurring dissolution pits (77). The dissolved O concentration for the experiment is well above the stoichiometric Fe_3O_4 line at 450 °C, so the occurrence of simultaneous dissolution and oxide formation is somewhat surprising. A possible explanation may be that the temperature threshold for the occurrence of a mixed corrosion mode hypothesized in (68) is significantly lower for pure Fe than 550 °C because the experimental data points shown in Figure 4 are largely based on corrosion experiments with alloys.

In ICE III, the assumed dissolved O concentration for the regular experiments discussed in Section 4.4 is between those reported for 450 °C in (198) and (77) ($5\times10^{-8} < 10^{-7} < 1.1\times10^{-6}$ wt%). This shows that the observed dissolution pits are likely a local phenomenon occurring on the surface of both Sample A and B and not a sign of a global switch to the dissolution regime in the chamber. The fact that the LBE bulk in the ICE chamber still contains sufficient O to support oxide formation is evident in those sample areas that are covered by Fe-oxide, which should either not be present at all or show signs of dissolution attack rather than the smooth surface observed in Figure 36 a). It is likely that, as hypothesized in (77), the LBE trapped underneath the oxide is

being depleted in dissolved O by continued oxide formation, which promotes the dissolution of the base metal.

The dissolution process at the Fe/LBE interface would eventually cease if at least one of the following two criteria is met: 1) the LBE reaches the dissolved Fe saturation concentration; or 2) sufficient dissolved O and Fe is present at the Fe surface to allow for oxide formation. At 450 °C, the saturation concentration of dissolved Fe in LBE is quite large (~$10^{-4.2}$ wt%, see Figure 2). Therefore, the first criterion is unlikely to be fulfilled given the temperature, the duration of the experiment, and the relative quantities of LBE and Fe available in the samples and the steel chamber.

The second criterion requires that the LBE in the corrosion pit is supplied with O from the bulk and that the dissolved Fe equilibrium concentration necessary to for oxide growth can be maintained near the solid-liquid interface. The excessive growth of the oxide that detached first – compared to the oxide thickness of other areas where it is still attached – shows that mobility of dissolved O and Fe through the oxide is rather high, but it still acts as a barrier that delays efficient species exchange with the bulk. Therefore, it appears that concentration gradients for both O and Fe are established across the oxide and the trapped LBE, which prevent an immediate return from a dissolution-dominated to an oxide-forming regime in the corrosion pit. While dissolved O migrates into the pits, Fe is continuously transported away from the base metal surface into the LBE bulk, which is relatively poor in dissolved Fe in comparison to the corrosion pit. As a result, a stable oxide cannot be formed on the base metal in the corrosion pit because the required interdependent Fe and O concentrations necessary for magnetite formation cannot be reached.

Dissolution attack also affects the detached oxide, which is no longer supplied with Fe sufficient to be maintained or grow. Over time, the oxide becomes rougher in appearance and ultimately thinner than oxide still attached to the base metal (see Figure 36 c)). At some point, it stops functioning as a barrier for species exchange with the bulk and oxide formation of the base metal should occur again, which restarts the oxide life cycle shown in Figure 36. Evidence for the existence of multiple oxide layers is shown in Figure 37 and has also been observed in the literature (77). In contrast to a static corrosion chamber like ICE III, erosion corrosion in a flow loop should accelerate the destruction of the oxide and therefore promote the return from an oxide-forming to a dissolution-dominated environment.

It should be noted that the equilibrium concentration of Fe necessary to form an oxide is not only dependent on temperature, but also on dissolved O content, and vice-versa (77). As more oxide is formed over time, the overall concentration of dissolved O in the LBE bulk decreases slowly, and a higher concentration of dissolved Fe is necessary to maintain oxide production. Therefore, in a static corrosion chamber, the dissolution rate in newly forming corrosion pits should accelerate over time. The O sources in the chamber (see Section 4.2.6) are supposed to counteract this acceleration, but their impact is difficult to quantify. A decreasing global O concentration also has implications for the stability of the oxide under temperature cycling (199), which will be discussed in more detail in Section 5.2.3.Therefore, the observation of a mixed corrosion mode in ICE III (see Figure 36) fits well with the results reported in the literature.

The samples in (77) also showed detached and buckling oxide layers as well as oxide networks similar to that shown in Figure 37, but more extensive and complex. The complexity is likely due to the significantly shorter corrosion time in the experiments presented here (up to ~60 hours compared to up to 8000 hours). A thin oxide parallel to the original oxide-metal interface like that shown in Figure 36 c) was observed as well (see Figure 6 b) in (77)). Interestingly, the authors also found evidence that some areas on the samples experienced practically no corrosion after 8000

hours of exposure while others showed intergranular dissolution, which has not been observed in the ICE III samples. It is possible, however, that a more detailed analysis of the ICE III sample cross sections will reveal evidence of local intergranular dissolution in the future. The nature of the oxide in ICE III should also be investigated further because the results presented in (77) clearly indicate the presence of bi-layered magnetite on pure Fe with some Pb and Bi present at the interface between the two oxide layers. Overall, however, the corrosion behavior observed in this work is consistent with that expected for pure Fe in LBE. This shows that – despite the static nature of the ICE III corrosion cell and the absence of active dissolved O control – a mixed corrosion mode (oxide formation / dissolution) typical for pure Fe can be achieved for the experimental durations considered here.

5.1.2. Corrosion rate

The corrosion rates observed in ICE III are substantially higher than predicted, for example, by the power-law kinetics model developed by (77), which indicates a loss of ~2 μm after 40 hours of corrosion in O-rich LBE (see Figure 35). The sample thicknesses observed on Sample 3B (corrosion-only sample) and on Sample 3A (irradiation-corrosion sample) far away from the beam spot are between 45 and 47 μm. Assuming an original sample thickness of 50 μm, this corresponds to a loss of 3-5 μm in ~40 hours. However, the typical thickness of the as-rolled samples was measured to be 52-55 μm, so the corrosion rate is actually even higher.

One possible reason for this may be the lower dissolved O content of the LBE in ICE III, compared to (77). It is assumed that the LBE initially contains ~10^{-7} wt% O, which is the saturation concentration at 200 °C, the filling temperature of the ICE chamber (see Section 4.2.6). The plenum above the LBE and the solid Bi_2O_3 pellet in the chamber are supposed to continuously supply O. However, since this cannot be verified, it is possible that the kinetics of O uptake by LBE from either source are too slow. The presence of oxide layers on and near both samples in the experiments shows that sufficient O is present to support oxide formation, as discussed in the previous section. Over time, as more oxide is formed on all surfaces in the chamber, O is consumed. If the O sources are not effective in replenishing the consumed O, it is likely that the dissolved O concentration decreases continuously. 10^{-7} wt% O is slightly above the stoichiometric line for Fe_3O_4, but over time, the O concentration may drop below it without necessarily reaching the Fe_3O_4 stability limit. This likely extends the dissolution step of each oxide lifecycle, which may explain the high corrosion rates observed in this work, even in corrosion-only regions (Sample B, Sample A far away from the beam spot).

A second consequence of a low dissolved O concentration is that the concentration becomes significantly more sensitive to temperature changes even if the O content is within the supposedly stable regime for Fe_3O_4 (199). Dissolved O concentrations were measured for a static batch of LBE with a dissolved Fe concentration of 1.6×10^{-5} wt% and varying O concentrations (within the operation regime) while the temperature was cycled between 300 and 500 °C (199). At low O concentrations (between10^{-7} and 10^{-8} wt%), this temperature difference of 200 °C led to O concentration changes of ~4 orders of magnitude, while no such drastic changes could be observed at high O concentrations (10^{-5} wt%) (199). The authors ascribe this to interactions of the LBE primarily with dissolved Fe and the temperature-dependent promotion of Fe_3O_4 formation and dissolution. Under ICE III conditions, if the dissolved O concentration falls below 10^{-7} wt%, a theoretical drop by almost an order of magnitude could be reached in the beam spot for Exp. 2, where the temperature changes from 400 to 450 °C when the beam is turned on (see Table 8). For Exp. 3, with a ΔT of 20 °C for TC_A, such a change would be less dramatic (less than half an order

of magnitude), which may in part explain the differences between the corrosion rates of Exp. 2 and 3. In (199), the temperature changed with a rate of 1.6 °C per minute, which is much slower than the temperature changes experienced by the ICE III chamber when the beam is turned on or off (a few seconds). In addition, the ICE III chamber is typically not held at the lower temperature (beam off) for more than 10 s, unless the beam needs to be tuned. Therefore, the system likely does not have enough time to equilibrate in the same manner as reported in (199). Nevertheless, the brief temperature changes introduce a driving force for oxide precipitation (beam off) or oxide dissolution (beam on), assuming that the dissolved O concentration is indeed low enough to reach this region of instability.

Another possible cause for the differences in corrosion rate between the corrosion-only areas of the ICE III samples and values reported in the literature is the surface preparation of the samples. The Fe foils in the experiments presented here were mounted in as-rolled condition. The varying thickness of the samples (52-55 μm) shows that the surface is quite rough. This implies that during corrosion, the oxide does not grow on a truly flat surface, which increases the stresses that develop in the growing oxide. Higher stresses may lead to accelerated oxide detachment, as discussed in Section 3.2.1.2, and therefore an earlier onset of pitting corrosion and local dissolution, which increases the frequency of oxide life cycles. To remove this potential factor, an experiment with electropolished samples should be performed for comparison.

5.1.3. Irradiation rate

The corrosion rate in and near the beam spot is clearly significantly higher than far away from it on the same sample or on the other side of the chamber on Sample B. Before the underlying mechanisms can be discussed (see Section 5.2), it is worthwhile to put the dose rate applied in this experiment into perspective. Figure 45 shows expected dpa rates for LWR, LFR, and MSR environments vs. temperature. For comparison, irradiation-corrosion experiments with sample doses or dose rates reported in the literature are shown for the three environments. This shows that most laboratory irradiation-corrosion experiments, most of which employ protons instead of neutrons to increase the dpa rate, operate in a dose rate regime well above that expected for most materials in a nuclear reactor environment. For exceptionally high fuel burnup, some core internal materials, such as fuel cladding, may experience dose rates on the order of 10^{-6} dpa/s, assuming a dose of 150-200 dpa at the end of their 2-4 year-long residence time in LFRs. This is an order of magnitude larger than the maximum typical dose rate shown in Figure 45, but still lower than many laboratory irradiation-corrosion experiments, including this work.

The choice between accelerated ageing and the attempt at an accurate replication of the expected in-reactor dose rate regime is extremely important for the interpretation of the results. At low dose rates, radiation-induced defect longevity largely depends on the availability of sinks. At high dose rates, recombination becomes more prevalent, which implies that disproportionately fewer created point defects reach sinks, such as GBs. The boundary between the sink-dominant and the recombination-dominant regime is dependent on dose rate and temperature, but also materials properties and the nature of the point defect (see, e.g., (200)). Therefore, to maintain a certain level of defect mobility, changes in dose rate can be compensated by changes in temperature ((153)). As mentioned in Section 3.5.1.3, neutron flux has been shown to affect corrosion rates of Zircaloy. The accelerated replication of these results with ion irradiation would require a temperature shift, which would inevitably change corrosion kinetics. The extent to which the simulation of corrosion under irradiation can be accelerated is therefore fundamentally limited

by this trade-off between maintaining representative irradiation-induced defect behavior and temperature-appropriate corrosion kinetics.

The dose rate also plays an important role in Tiny-ICE. Since the beam is rastered to avoid beam heating, a large number of defects is induced locally when the beam passes over a certain region. However, while the beam passes across other areas of the sample, these point defects have time to evolve in the absence of the beam. Defects that have recombined or annihilated at a sink in this time frame are no longer available to interact with newly created defects on the next pass of the beam. Therefore, the surviving defect content of two samples irradiated to the same dose using either a rastered beam or a defocused beam will likely be different, which may affect the expected synergies between irradiation and dissolution corrosion in Tiny-ICE.

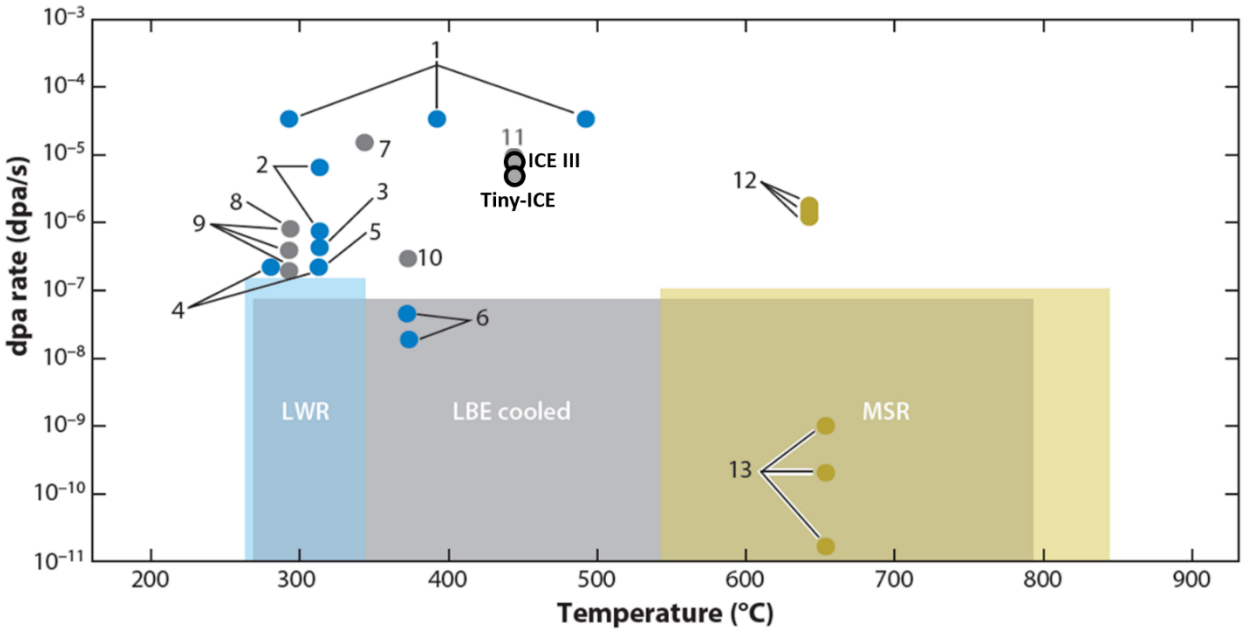

Figure 45 – Semi-log plot of estimated dpa rate regimes for LWRs, LFRs, and MSRs vs. temperature, adapted from (26). Each data point corresponds to a simultaneous irradiation-corrosion experiment with a coolant relevant to one of the reactor types (1-6 LWR, 7-11 LFR, 12-13 MSR) and a reported dose estimate. The references for the individual data points are: 1: (126), 2: (138), 3: (201), 4: (202), 5: (203), 6: (204), 7: (150), 8: (205), 9: (147), 10: (146), 11: (157), 12: (142), 13: (206). The two points with a black border show the dose rates for regular ICE III experiments and Tiny-ICE.

5.2. Enhanced corrosion mechanisms of pure Fe in LBE under simultaneous proton irradiation

Aside from radiation-induced defects, which are the primary object of study, there are beam-induced thermal effects that play a role in producing the experimental results observed in ICE III. Beam heating and its potential impact on corrosion is important to understand because it interferes with the interpretation of the results, which likely cannot purely be ascribed to radiation-induced damage. In fact, the slightly accelerated corrosion of Sample 3B, which was not exposed to proton irradiation and was discussed in Section 4.4.5, may even suggest that beam heating effects overshadow the much more subtle consequences of radiation-induced defects.

In this section, the potential effects mentioned throughout this work are summarized and an attempt is made to provide a mechanistic picture of the irradiation-corrosion process of pure Fe in LBE. It is assumed that the oxide formed during the regular ICE III experiments under oxide-

forming conditions is Fe_3O_4, as expected for pure Fe corrosion in LBE, although additional sample analysis is required to confirm this. The system considered here is therefore a polycrystalline pure α-Fe (bcc) base metal covered with a polycrystalline Fe_3O_4 film.

5.2.1. Fe and Fe_3O_4 in the absence of radiation

In the absence of radiation-induced defects, the higher concentration of equilibrium vacancies compared to equilibrium interstitials leads to a vacancy mechanism controlling self-diffusion in bulk bcc-Fe at all temperatures (207). The higher equilibrium vacancy concentration is due to a lower formation energy at low temperatures and a higher formation entropy at high temperatures compared to interstitials (207). For GB self-diffusion, however, some models show that self-interstitials have a significant impact in bcc-Fe, which is in part due to similar predicted formation energies for vacancies and interstitials (208). The results also showed that GB diffusion is significantly faster than diffusion in the bulk, with the value of the GB diffusion coefficient depending on the nature of the GB (208).

An excellent review of the properties of the different Fe-oxides is given in (209). Fe_3O_4 is thought to have an inverse spinel structure with a close-packed cubic O lattice, in which Fe^{3+} ions occupy the tetrahedral sites and a 50:50 mix of Fe^{3+} and Fe^{2+} ions occupies the octahedral sites, although ionic ordering and charge distribution in Fe_3O_4 are likely not this straightforward (see (210)). Within a framework that considers Fe_3O_4 to be ionically ordered, the cation distribution becomes disordered and ultimately random with increasing temperature. However, this disorder is not expected to have a large impact on cation diffusivities in Fe_3O_4, at least between 500 and 1400 °C (see (211, 212)). In oxidizing conditions, cation diffusion occurs via a vacancy mechanism in the octahedral sublattice, while under reducing conditions, an interstitial-based mechanism dominates (213). As the mechanism changes, the Fe diffusion coefficient reaches a minimum that varies with O fugacity and temperature (213). Fe diffusion is generally faster than O diffusion in Fe_3O_4 and is thought to be the primary driver of the oxidation of Fe to Fe_3O_4 (214).

5.2.2. Radiation damage effects

High energy protons produce a large number of non-equilibrium point defects in the base metal and the oxide during the collision cascade. Those point defects that do not immediately recombine migrate through the material until they are absorbed by a defect sink or annihilate. To what extent the diffusion coefficients in the bulk and at GBs are affected by radiation-induced defects is not well-understood.

In situ TEM irradiation of model Fe/Fe_3O_4 samples with 1 MeV Kr^{2+} ions up to 10 dpa (at a dose rate of approximately 10^{-3} dpa/s) showed that dislocation loops formed in single-crystal Fe starting at ~1 dpa at different temperatures (25, 300, and 500 °C) and grew with dose (215). In the polycrystalline oxide, however, dislocation loops and defect clusters resolvable by TEM could not be observed at 500 °C due to point defects migrating to sinks before a buildup of higher-order defects could occur (215). Increased defect mobility due to temperature was already observed at 300 °C, where only thicker regions of the oxide developed loops. In contrast, at 25 °C, dislocation loops that grew with dose were observed in oxide grains, which shows the sensitivity of defect mobility to temperature. The presence of defect-denuded zones near Fe_3O_4 GBs implies that – even at 25 °C – the GBs acted as efficient defect sinks, which could not be observed in the single-crystal Fe metal (215). These results show the impact of radiation dose on defect evolution, and also emphasize the importance of grain size for defect accumulation within the grain.

At lower doses (between 10^{-4} and 2.2×10^{-2} peak dpa), self-ion irradiations of an epitaxially grown pure Fe with a 50 nm thick Fe_2O_3 cap with 2 MeV Fe^{2+} at room temperature have shown the accumulation of dislocation loops at the metal/oxide interface via TEM as well as vacancy accumulation via PALS (192). Both the number of vacancies as well as vacancy cluster size near the interface increase with dose. It is important to note here that the interface is more than 500 nm away from the dpa peak in the single crystal Fe base layer (see Figure 1 in (192)). The authors ascribe the growth of vacancy clusters to dislocation loops acting as preferential sinks for interstitials in contrast to the interface, which acts as a neutral defect sink.

In extreme cases, radiation damage can amorphize crystalline materials, which may have an impact on bulk diffusion. Fe_3O_4, however, appears to be quite amorphization resistant. Neutron irradiations up to a fluence of 2×10^{20} neutrons/cm^2 induced no amorphization and produced very weak swelling (< 0.1 vol%) in Fe_3O_4 (216). The authors ascribe this amorphization and swelling resistance to the large number of empty lattice sites in the inverse spinel structure of Fe_3O_4 (216). A resistance of Fe_3O_4 to amorphization was also observed for heavy ion irradiations (217). Fast electron irradiation of Fe_3O_4 up to a dose of 2 MGy has been found to induce a phase transformation to FeO (wüstite) via intermediate steps where α-Fe_2O_3 (hematite) and γ-Fe_2O_3 (maghemite) are present (218). Based on the neutron irradiation results mentioned above, however, it is unlikely that such a radiation-induced transformation is taking place under ICE III conditions.

Aside from radiation dose effects, the dose rate is also important for transport in solids. Isotope tracer studies in epitaxially grown Fe_2O_3 have shown that self-diffusion of cations and anions is enhanced with increasing dose rate under heavy ion irradiation (400 keV Ar^+ at dose rates of 2×10^{-5} and 2×10^{-3} dpa/s at 500 °C up to 0.62 dpa at the tracer layer) (200). A similar observation was made for anions in Fe_2O_3 under proton irradiation (1 MeV up to 0.1 dpa at a rate of 10^{-6} dpa/s) at 450 °C (219). Cations were not studied in these experiments. Interestingly, in both studies, Fe_2O_3 locally transformed into Fe_3O_4, and in some samples, the transformed region reached the isotopically labeled tracer layer (200, 219). Unfortunately, no direct comparison between Fe_3O_4 irradiated at two different conditions could be made. However, it seems reasonable to assume that cation and anion diffusivity will increase under irradiation as well, although likely to a lesser extent than for hematite because the magnetite diffusivities are already quite large in comparison.

The proton beam also excites atomic electrons and ionizes atoms in its path. In this ionized state, the reactivity of the oxide species is increased, which may lead to increased reaction rates at the metal/oxide and oxide/HLM interfaces. In oxides, the electrical conductivity can increase under irradiation (132), which signals a higher mobility of electrons and/or ions in the oxide. Therefore, charge exchange at the interfaces may be accelerated, which may lead to increased corrosion rates.

In ICE III, the presence of GBs is expected to hamper the accumulation of radiation-induced point defects necessary to form higher-order defect structures in both the polycrystalline oxide and the polycrystalline base metal. Given the lower dose rates in ICE III (~2 orders of magnitude lower), damage accumulation is likely to take longer, which should result in an even smaller dislocation loop density than observed in (215). The defects traveling towards the GBs may lead to complex effects beyond recombination, such as GB migration (220, 221). Irradiation-induced cation interstitials may also use GBs as fast diffusion paths to reach the oxide/LBE interface quickly and accelerate the growth of the oxide while leaving vacancies behind in the base metal.

One of the key aspects of the Fe corrosion process in LBE is the accumulation of pores at the oxide-Fe interface (without the presence of radiation) (80). As corrosion progresses, the migration of Fe outward through the oxide-LBE interface leaves behind vacancies at the interface with the

metal. These vacancies can then be filled by new oxide growth ("available space model") or annihilated by Fe diffusion from the base metal. The defects radiation produces in the base metal and in the oxide and their migration should affect the corrosion-induced vacancy accumulation at the oxide-metal interface in some way. Radiation-induced defects may accelerate or decelerate corrosion-induced vacancy accumulation at the metal/oxide interface via the promotion of Fe diffusion through the oxide away from it or by accelerating Fe diffusion through the base metal and thereby promoting annihilation at the metal/oxide interface, respectively.

Early in the corrosion process, the presence of vacancies at the metal/oxide interface is beneficial. The decrease of the surface area between the oxide and the base metal decreases the amount of Fe that can diffuse through the oxide and thereby decreases its growth rate. At the same time, however, increased porosity at the oxide-metal interface weakens the adherence of the oxide. Under irradiation, cation and anion diffusivity is likely enhanced in both the base metal and the oxide, as discussed previously. Therefore, it seems likely that radiation-induced defects promote quick growth and simultaneously early detachment of the oxide by contributing to the vacancy accumulation at the metal/oxide interface. This is because the cation diffusivity in the oxide should still be substantially faster than that in the bulk, even under irradiation. Consequently, the oxide experiences a process similar to its behavior without irradiation present, but faster. If this is the case, more and likely thinner detached oxide layers should be found floating in the LBE away from the sample surface under simultaneous irradiation-corrosion conditions than under corrosion-only conditions.

5.2.3. Beam heating effects

An increase in temperature while the beam is on leads to accelerated diffusion kinetics in the sample. This implies that radiation-independent diffusion processes occur at slightly higher rates, but also that any radiation-induced defects migrate and annihilate or recombine slightly faster than they would without beam heating. On the lower end of measured ΔT values on TC_A (the TC closer to the beam spot) a difference of ~15 °C for Exp. 3 is not expected to have a large impact on kinetics. For Exp. 2, however, where the measured ΔT was 50 °C behind the beam spot, it may have a measurable impact.

While the increase of defect mobility due to the higher temperature in and near the beam spot may play a role in accelerating corrosion, it seems more likely that the primary effect of beam heating is related to the temperature-dependent dissolved O and Fe concentrations required for Fe_3O_4 formation and stability. This effect was already discussed in Section 5.1.2 because it appears to be the primary driver behind the accelerated corrosion rates observed in ICE III compared to those reported in the literature. The relatively low dissolved O concentration of 10^{-7} wt% at the beginning of the experiment and its decrease throughout due to the formation of oxides increase the sensitivity of the system to temperature fluctuations. As a consequence, beam heating locally destabilizes the oxide and promotes its dissolution compared to other areas of Sample A further away from the beam spot and the much colder Sample B on the other side of the chamber.

Another, presumably minor, effect is due to the injection of H into the LBE by the proton beam. H_2 gas could scavenge dissolved O from the LBE and thereby lower the O concentration even faster than the corrosion process alone. However, any contributions to a decreasing O concentration are expected to be negligible given the relatively linear thickness loss Samples 2A and 3A experience (see Figure 35). If this was a strong effect, Sample 3A should be affected disproportionately since a substantially larger amount of H was injected over the course of a longer experiment (42 vs. 22 hours). Rather, it appears that the thickness loss of the sample is primarily

linked to more O being bound in the form of Fe_3O_4, as discussed previously, which in turn appears to be linked to temperature fluctuations.

Such a link between ΔT values and acceleration of corrosion would also explain the similar thicknesses of Samples 2A and 3A, even though Sample 3A experienced almost twice the dose of Sample 2A. It appears therefore, that the observed irradiation-corrosion behavior in ICE III is largely due to beam heating, while irradiation-induced non-equilibrium defects play a smaller role. This shows that beam heating is not necessarily a negligible effect and that it should not be dismissed out of hand as a factor in the interpretation of irradiation-corrosion experiments as is sometimes done in the current literature.

5.3. Concluding remarks on the different ICE III experiments

The members of the family of ICE III setups presented in this work have a number of advantages and disadvantages compared to one another. The "regular" ICE III chamber is supposed to be the standard irradiation-corrosion chamber and is meant for the study of bulk materials in the form of relatively thin (up to 50 µm) circular (2 cm diameter) samples. The purpose of the molten salt chamber is to allow for irradiation-corrosion experiments with smaller volumes of rare corrosive media. Finally, Tiny-ICE was designed to accommodate thin-films in an irradiation-corrosion setup and to increase the quantity of samples that can be produced.

5.3.1. Limitations

The regular ICE III chamber and the molten salt chamber are limited in terms of ions that can be selected (protons, possibly high-energy He) due to the sample thickness required to maintain a seal between the corrosive medium and the beamline vacuum. Both also suffer from the fact that the chambers themselves are made of steel flanges, while the samples are likely a different material, which is not ideal for a corrosion experiment, where similar materials in contact with the corrosive medium are desirable. In some cases, replacing the chamber materials to match the samples may be an option, but in most cases, it will be impossible or prohibitively expensive.

Tiny-ICE, on the other hand, has more flexibility when it comes to sample holder materials, since the entire "chamber" is in vacuum and mounted on a heater stage. Given a sufficiently thin thin-film, high energy heavy ions may even be used instead of light ions. Unlike the larger ICE chambers, Tiny-ICE is intended to be exposed to a rastered beam. While rastering removes temperature effects, which appear to greatly affect the corrosion behavior under irradiation in the experiments with pure Fe in LBE presented in this work, it leads to lower dose rates and slightly different radiation-induced defect creation in the sample compared to a defocused beam.

Finally, none of the setups can reproduce potential effects from TP or FP creation by neutrons, which is an inherent limitation of the use of proton irradiation to emulate neutron damage. In addition, the experimental duration is limited by the sample thickness and the ability of a static corrosion chamber to maintain the corrosion process of interest, e.g., by providing sufficient dissolved O in LBE or by preventing the saturation of molten salts with corrosion products.

5.3.2. Importance of in situ monitoring techniques

The semi-quantitative monitoring of corrosion made possible by PIXE is a very helpful tool for the analysis of corrosion processes under irradiation. Without PIXE, practically no information about Sample 1A could have been recovered. Another example is the discovery of the interruption

of accelerated corrosion in the absence of the beam observed in Exp. 2. Without PIXE, this observation would not have been possible. Furthermore, the observation that the corrosion of Sample 2A proceeds much faster than that of Sample 3A despite similar dpa rates would likely have been interpreted differently in the absence of PIXE data. The final thickness of the samples in the beam spot shows that there must have been a difference between the corrosion conditions of the two experiments. Without additional information, the main explanation for this probably would have been a lower/higher initial thickness of Sample 2A/3A. Figure 35 shows, however, that the average initial thickness of both samples is the same. Therefore, the difference in corrosion rate under irradiation must either be due to differences between the samples other than the thickness, e.g., surface roughness or degree of cold work, or differences between the corrosive environments, e.g., the dissolved O content or local temperature differences. Since the samples came from the same batch of pure Fe sheets, the former seems unlikely. As discussed in Section 5.1.2, the dissolved O content of the LBE is not well-controlled, but the chamber filling temperature is the same for all experiments and all chambers have an air-filled plenum and a Bi_2O_3 pellet as a potential O source. The most obvious difference between the two experiments is the temperature difference observed by the TCs inside the ICE chamber, as discussed in Section 4.4.5.1.

The TCs played a vital role in obtaining this information. A single TC is already valuable to gain some insight into beam-induced temperature differences when the beam is on or off. The addition of the second TC facing away from the beam allowed conclusions about the temperature distribution across the corrosion chamber and the differences in conditions between Sample A (irradiation-corrosion sample) and Sample B (corrosion-only sample) to be drawn. Without the TCs, one of the primary arguments presented in the discussion of the experimental results, namely that beam heating plays a significant role in accelerating corrosion in the presence of the proton beam, could not have been drawn.

This underscores the value of having one or several in situ monitoring techniques to unravel the multitude of complex processes occurring in simultaneous irradiation-corrosion environments. With the complexity added by studying binary or ternary alloys, the value of these tools will increase even further. Therefore, the addition of these or similar techniques, such as PIGE, RBS, or electrochemical techniques should be considered for any irradiation-corrosion experiment.

5.3.3. Relevance of pure Fe studies to structural materials

In HLM systems, the corrosion rate of pure Fe is important to understand because it tends to correlate well with corrosion rates of F/M steels, as mentioned in Section 3.2.1.2. T91 (9 wt% Cr), for example, shows similar dissolution rates in O-poor flowing LBE ((79)) as well as similar oxide growth rates in O-rich flowing LBE ((77, 78)) at 450 °C compared to pure Fe. The primary difference is that the magnetite/FeCr spinel oxide on T91 is rarely found to be detached from the substrate and that LBE is less often found at the oxide-metal interface. The measured thicknesses indicate, however, that the inner FeCr spinel does not provide improved oxidation resistance, at least for the duration of the experiment (up to 8000 hours). The question is whether the relationship between Fe and T91 corrosion remains the same under irradiation, and if not, which other model alloy may be more representative of the behavior of F/M steels under simultaneous irradiation and LBE corrosion. It would also be interesting to determine whether the behavior or protectiveness of the oxides changes under irradiation. Unlike F/M steels, austenitic stainless steels, such as 316L, appear to have substantially lower dissolution rates than pure Fe, contrary to the expected accelerated corrosion of high-Ni containing alloys (79). This indicates that, even in the absence of

irradiation, pure Fe is not a suitable model system for studying austenitic stainless steels and that a different model alloy has to be found.

In alloys, corrosion processes are necessarily more complex than in pure metals due to competition of species in the solid. Radiation further increases this complexity by introducing effects, such as RED and RIS, which rely on the presence of at least two different species. These processes are generally thought to exacerbate by corrosion by locally changing the alloy composition, as discussed in Section 3.3.2. In some cases, however, radiation-decelerated corrosion of alloys has been reported, as mentioned in Section 3.5.1.7. One of these studies reported the deceleration of Ni-20Cr corrosion in FLiNaK at 650 °C due to simultaneous 3 MeV proton irradiation up to 0.028 peak dpa (142). However, a similar irradiation-corrosion experiment with pure Fe showed that corrosion was accelerated in the beam spot (142). The authors explain this observation with a model reliant on preferential dissolution of Cr over Ni in the case of Ni-20Cr, where the production of Frenkel pairs by irradiation modifies bulk diffusion rates and promotes self-healing. In a pure metal, however, preferential dissolution cannot occur, and therefore, corrosion is thought to be accelerated by radiation-induced effects in the molten salt (142). It would be interesting to determine if irradiation of a binary or ternary alloy corroded by LBE also shows radiation-decelerated corrosion, what the underlying mechanism may be, and if it is also active in real structural materials.

6. Conclusions and future work

6.1. Summary of experimental results

Section 4.2 presented an extensive description of the design choices made for ICE III and described experimental challenges and lessons learned to inform the design of similar future experiments. The result is a relatively simple setup that can be used for the accelerated testing of materials under simultaneous irradiation and corrosion. The addition of PIXE as an in-situ corrosion monitoring technique gives detailed qualitative insight into the corrosion process of pure Fe in LBE under proton irradiation with unprecedented time resolution (as little as 5 s of acquisition time per data point). With the help of a standard, the PIXE signal can be used to monitor the sample's thickness change continuously over tens of hours of experiment time. According to SEM results presented in Section 4.4.4, the PIXE estimate of the sample thickness at the end of the experiment is ~7 μm larger than the average thickness observed in the beam spot. The thickness overestimate can also be observed at the beginning of the experiment and is likely caused by systematic differences between the standard and ICE III, e.g., due to differences in beam current and beam spot size. Once the exact cause is determined, an appropriate correction should improve the accuracy of the semiquantitative PIXE estimates. Nonetheless, time-resolved PIXE clearly is a powerful tool for corrosion monitoring under irradiation already.

The evaluation of HT-9 irradiated with 5.5 MeV protons and simultaneously corroded by LBE in ICE II was presented in Section 4.1. The results showed that there is a measurable increase in oxide thickness (from 2-10 μm to up to 35 μm) in a ~4 mm wide section of the cross section. However, the sample's thickness in the center of this region is too large to be fully penetrated by 5.5. MeV protons. Therefore, this oxide thickness increase cannot be caused by irradiation damage in the oxide. The results are somewhat ambiguous as to whether beam heating alone or the migration of radiation-induced defects are the cause.

Section 4.4 presented results from three runs of ICE III with pure Fe and LBE. The first experiment already showed that corrosion was greatly accelerated during irradiation, because the sample failed after ~60 hours even though previous corrosion-only experiments under nominally identical conditions were still intact after more than 200 hours of corrosion. The intent of this series of experiments was to cover a large range of experimental durations and sample exposures to determine a relationship between the dpa and the associated acceleration of corrosion. However, the results from Exp. 2 and Exp. 3 show that this relationship is not necessarily linear and other factors, such as beam heating, are at play. The thicknesses predicted by PIXE are within a few μm of one another, even though Sample 3A was exposed to almost twice the dpa and corrosion duration. The temperature differences across the chamber indicate that there is a non-negligible contribution of beam heating to the acceleration of corrosion here. This conclusion can only be drawn because there is direct experimental evidence thanks to two TCs mounted directly in the corrosion chamber.

The results of ICE II were somewhat ambiguous but showed that direct irradiation damage in the oxide is not the main cause of accelerated corrosion of HT-9 in LBE. Exp. 2 showed that equilibrium defects play a small role in accelerating corrosion if any at all. Corrosion effectively stopped when the beam was off, which proves the second hypothesis posed in this work, namely that the acceleration of corrosion is greater under simultaneous irradiation-corrosion conditions than when irradiation and corrosion are decoupled. Of course, the behavior observed in Exp. 2 could also be explained if all acceleration of corrosion is exclusively due to beam heating. However, the fact that both TC_A and TC_B in Exp. 2 and Exp. 3 respond to the presence of the beam despite

the distance between them shows that there is very efficient heat transfer inside the ICE III chamber. This implies that the entire surface of Sample A should be substantially hotter than Sample B in both experiments, which should lead result in Sample A being consistently thinner than Sample B. However, thicknesses measured on Sample 3A indicate a much smaller beam-spot-affected zone, which shows that beam heating alone cannot be responsible. This supports the first hypothesis, namely that radiation accelerates the corrosion of pure Fe in LBE. Preliminary results in the dissolution corrosion regime obtained with Tiny-ICE, where no beam heating was measured, also point in this direction. Therefore, a combination of beam heating and radiation-induced non-equilibrium defects is responsible for the acceleration of pure Fe corrosion in LBE, specifically

1) The increase of the vacancy concentration in the base metal and the oxide due to radiation damage and beam heating;
2) The increase of the interstitial concentration in the base metal and the oxide due to radiation damage;
3) The increase of electron and/or ion mobility and the increase of the reactivity of species in the oxide due to ionization by radiation damage;
4) The increase of temperature-dependent diffusion kinetics of point defects as well as species in the base metal, the oxide, and the LBE;
5) The increase in dissolved Fe transport away from the surface of the irradiated sample due to the establishment of a temperature gradient due to beam heating;
6) The decrease of oxide stability due to beam heating under globally decreasing dissolved O concentrations.

The exact contributions of these factors, however, remain as topics of investigation for future experiments.

6.2. Future work

The goal of ICE III is to provide a platform for the accelerated study of materials under simultaneous irradiation-corrosion conditions. The designs in the ICE III family presented in this work are very flexible and can be used for a variety of irradiation-corrosion studies in different liquid corrosive media. The results presented here have shown that it can provide interesting information about the behavior of samples in such environments within hours rather than years in a reactor. For LBE, studies of pure Fe as a model material are valuable, but only the beginning. In order to understand the behavior of complex alloys in irradiation-corrosion environments, more complex binary and ternary alloys need to be investigated.

For pure Fe, it would be useful to continue experimental work to understand what the relative contributions of radiation-induced and thermally induced defects in the base metal and the oxide are to determine the effects of beam heating on irradiation-corrosion processes. Beam heating can be removed as a factor by using smaller beam currents or rastered beam scans, as in Tiny-ICE. In regular ICE, this could lead to a series of experiments with varying small currents to determine the effect of current density on Fe corrosion. PIXE can be used to monitor the behavior of the sample under irradiation and ideally to determine corrosion kinetics as a function of beam current or temperature gradients in the chamber. The apparent interruption of corrosion during the absence of the beam could be studied in more detail to determine time constants for the different corrosion steps and elucidate underlying mechanisms. Experiments with lower beam energies where radiation damage is exclusively induced in the metal could lead to a better understanding of

radiation-induced defect mobility and the effects defects in the base metal have on oxide layer formation.

Several additions to the current setup could be made in the future to improve its utility. The addition of RBS would be valuable, especially for coolants that do not produce x-rays suitable for PIXE. In the case of molten-salt ICE, in situ electrochemical methods, e.g., electrical impedance spectroscopy, may yield new insights into corrosion product behavior in the corrosive medium under irradiation.

Clearly, there is a substantial amount of fundamental science to be discovered with a tool like ICE. Modern detectors and data acquisition systems enable the capture of a tremendous amount of detail about the state of a dynamic irradiation-corrosion system with very high time resolution. The hope is that the results presented here motivate the incorporation of in-situ monitoring techniques in other irradiation-corrosion setups as well. While the work presented here only hints at some of the questions that could be answered in the field of basic irradiation-corrosion research, the further development of experiments such as this will hopefully continue to accelerate materials discovery for advanced nuclear reactors and other radiation-corrosion environments.

7. References

1. Kelly JE. 2014. Generation IV International Forum: A decade of progress through international cooperation. *Prog. Nucl. Energy*. 77:240–46
2. IAEA. 2022. Nuclear Power Reactors in the World
3. IEA. 2022. *Electricity Market Report January 2022*. https://www.iea.org/reports/electricity-market-report-january-2022
4. Pioro I. 2016. *Handbook of Generation IV Nuclear Reactors - 1st Edition*. Woodhead Publishing
5. Abderrahim HA. 2012. Multi-purpose hYbrid Research Reactor for High-tech Applications a multipurpose fast spectrum research reactor. *Int. J. Energy Res.* 36(15):1331–37
6. Behar C. 2014. Technology roadmap update for generation IV nuclear energy systems
7. IAEA. 2022. *Age Distribution*. https://pris.iaea.org/pris/worldstatistics/operationalbyage.aspx
8. OECD. 2010. *Actinide and Fission Product Partitioning and Transmutation*
9. Lanham WB, Runion TC. 1949. PUREX process for plutonium and uranium recovery
10. Salvatores M, Zaetta A, Girard C, Delpech M, Slessarev I, Tommasi J. 1995. Nuclear waste transmutation. *Appl. Radiat. Isot.* 46(6–7):681–87
11. Salvatores M, Slessarev I, Uematsu M. 1994. Global physics approach to transmutation or radioactive nuclei. *Nucl. Sci. Eng.* 116(1):1–18
12. Yang WS, Kim Y, Hill RN, Taiwo TA, Khalil HS. 2004. Long-Lived Fission Product Transmutation Studies. *Nucl. Sci. Eng.* 146(3):291–318
13. Kambali I. 2021. Feasibility study of Cs-137 nuclear waste transmutation by 13-MeV proton bombardment
14. Choppin GR, Liljenzin J-O, Rydberg J. 2002. The Nuclear Fuel Cycle. *Radiochem. Nucl. Chem.*, pp. 583–641
15. IAEA. 2012. Structural Materials for Liquid Metal Cooled Fast Reactor Fuel Assemblies-Operational Behaviour
16. Loewen EP. 2012. The USS Seawolf Sodium-Cooled Reactor Submarine
17. PRIS IAEA. 2022. *The Database on Nuclear Power Reactors*. https://pris.iaea.org/pris/
18. Alemberti A, Smirnov V, Smith CF, Takahashi M. 2014. Overview of lead-cooled fast reactor activities
19. Lorusso P, Bassini S, Del Nevo A, Di Piazza I, Giannetti F, et al. 2018. GEN-IV LFR development: Status & perspectives. *Prog. Nucl. Energy*. 105:318–31
20. Fazio C, Gröschel F, Wagner W, Thomsen K, Smith BL, et al. 2008. The MEGAPIE-TEST project: Supporting research and lessons learned in first-of-a-kind spallation target technology. *Nucl. Eng. Des.* 238(6):1471–95
21. Fazio C, Sobolev VP, Aerts A, Gavrilov S, Lambrinou K, et al. 2015. Handbook on Lead-bismuth Eutectic Alloy and Lead Properties, Materials Compatibility, Thermal-hydraulics and Technologies - 2015 Edition
22. Zrodnikov A V, Chitaykin VI, Gromov BF, Grigoryv OG, Dedoul A V, Toshinsky GI. 2000. Use of Russian Technology of Ship Reactors with Lead-Bismuth Coolant in Nuclear Power. *IAEA-TECDOC--1172*
23. Zrodnikov A V., Toshinsky GI, Komlev OG, Stepanov VS, Klimov NN. 2011. SVBR-100 module-type fast reactor of the IV generation for regional power industry. *J. Nucl. Mater.* 415(3):237–44
24. Smith CF, Halsey WG, Brown NW, Sienicki JJ, Moisseytsev A, Wade DC. 2008. SSTAR:

The US lead-cooled fast reactor (LFR). *J. Nucl. Mater.* 376(3):255–59
25. Choi S, Cho JH, Bae MH, Lim J, Puspitarini D, et al. 2011. PASCAR: Long burning small modular reactor based on natural circulation
26. Schmidt F, Hosemann P, Scarlat RO, Schreiber DK, Scully JR, Uberuaga BP. 2021. Effects of Radiation-Induced Defects on Corrosion. *Annu. Rev. Mater. Res.* 51(1):293–328
27. Nordlund K, Zinkle SJ, Sand AE, Granberg F, Averback RS, et al. 2018. Primary radiation damage: A review of current understanding and models
28. Kim TK. 2013. GEN-IV Reactors. In *Nuclear Energy*, ed N Tsoulfanidis, pp. 175–201. New York: Springer
29. Ohshima H, Kubo S. 2016. Sodium-cooled fast reactor. In *Handbook of Generation IV Nuclear Reactors*, pp. 97–118. Elsevier Inc.
30. Bhatt NP, Borgstedt HU. 1988. Corrosion behaviour of structural materials in sodium influenced by formation of ternary oxides. *Mater. Corros.* 39(3):115–23
31. Mikami H, Shono A, Hiroi H. 1996. Sodium leak at Monju (I): Cause and consequences
32. Guidez J, Prêle G. 2017. *Superphenix: technical and scientific achievements*. Springer
33. Murty KL, Charit I. 2008. Structural materials for Gen-IV nuclear reactors: Challenges and opportunities. *J. Nucl. Mater.* 383(1–2):189–95
34. Zhang J, Li N. 2008. Review of the studies on fundamental issues in LBE corrosion. *J. Nucl. Mater.* 373(1–3):351–77
35. Feuerstein H, Oschinski J, Horn S. 1992. Behavior of Po-210 in molten Pb-17Li. *J. Nucl. Mater.* 191–194:288–91
36. Smith CF, Cinotti L. 2016. Lead-cooled fast reactor. In *Handbook of Generation IV Nuclear Reactors*, pp. 119–55. Woodhead Publishing
37. IAEA. 2022. *Advanced Reactors Information System*. https://aris.iaea.org/
38. Dual Fluid. 2022. Reinventing Nuclear -- Whitepaper Introducing Fifth Generation Nuclear by Dual Fluid
39. Frogheri M, Alemberti A, Mansani L. 2022. The Lead Fast Reactor: Demonstrator (ALFRED) And ELFR Design
40. Zhang J, Kapernick RJ, McClure PR, Trapp TJ. 2013. Lead-bismuth eutectic technology for Hyperion reactor. *J. Nucl. Mater.* 441(1–3):644–49
41. LeadCold. 2022. *SEALER*. https://www.leadcold.com/sealer.html
42. Choi S, Hwang IS, Cho JH, Shim CB. 2011. URANUS: Korean lead-bismuth cooled small modular fast reactor activities
43. Shin Y-H, Park S, Sup Kim B, Choi S, Soon Hwang I. 2015. Small modular reactor (SMR) development plan in Korea
44. Todreas NE, MacDonald PE, Hejzlar P, Buongiorno J, Loewen EP. 2017. Medium-Power Lead-Alloy Reactors: Missions for This Reactor Technology. *https://doi.org/10.13182/NT04-A3534*. 147(3):305–20
45. Garner F. 2006. Irradiation Performance of Cladding and Structural Steels in Liquid Metal Reactors. In *Materials Science and Technology*. Weinheim, Germany: Wiley-VCH Verlag GmbH & Co. KGaA
46. International Atomic Energy Agency. 2015. Status of Accelerator Driven Systems Research and Technology Development
47. Dai Y, Henry J, Auger T, Vogt JB, Almazouzi A, et al. 2006. Assessment of the lifetime of the beam window of MEGAPIE target liquid metal container. *J. Nucl. Mater.* 356(1–3):308–20

48. Travleyev AA. 2001. Heat Deposition in Spallation Module of Energy Amplifier Prototype (EAP-80) due to Low-Energy Neutrons and γ-rays
49. De Bruyn D. 2009. From MYRRHA to XT-ADS: lessons learned and towards implementation. No. INIS-XA--09N0647
50. Takahashi M, Igashira M, Obara T, Sekimoto H, Kikuchi K, et al. 2002. Studies on materials for heavy-liquid-metal-cooled reactors in Japan
51. Gong X, Short MP, Auger T, Charalampopoulou E, Lambrinou K. 2022. Environmental degradation of structural materials in liquid lead- and lead-bismuth eutectic-cooled reactors
52. Kolman DG. 2019. A review of recent advances in the understanding of liquid metal embrittlement
53. Gorse D, Auger T, Vogt JB, Serre I, Weisenburger A, et al. 2011. Influence of liquid lead and lead-bismuth eutectic on tensile, fatigue and creep properties of ferritic/martensitic and austenitic steels for transmutation systems. *J. Nucl. Mater.* 415(3):284–92
54. Stergar E, Eremin SG, Gavrilov S, Lambrecht M, Makarov O, Iakovlev V. 2016. Influence of LBE long term exposure and simultaneous fast neutron irradiation on the mechanical properties of T91 and 316L. *J. Nucl. Mater.* 473:28–34
55. Klueh RL, Shiba K, Sokolov MA. 2008. Embrittlement of irradiated ferritic/martensitic steels in the absence of irradiation hardening. *J. Nucl. Mater.* 377(3):427–37
56. Van den Bosch J, Hosemann P, Almazouzi A, Maloy SA. 2010. Liquid metal embrittlement of silicon enriched steel for nuclear applications. *J. Nucl. Mater.* 398(1–3):116–21
57. Hosemann P, Frazer D, Stergar E, Lambrinou K. 2016. Twin boundary-accelerated ferritization of austenitic stainless steels in liquid lead-bismuth eutectic. *Scr. Mater.* 118:37–40
58. Lambrinou K, Charalampopoulou E, Van der Donck T, Delville R, Schryvers D. 2017. Dissolution corrosion of 316L austenitic stainless steels in contact with static liquid lead-bismuth eutectic (LBE) at 500 °C. *J. Nucl. Mater.* 490:9–27
59. Del Giacco M, Weisenburger A, Mueller G. 2012. Fretting corrosion in liquid lead of structural steels for lead-cooled nuclear systems: Preliminary study of the influence of temperature and time. *J. Nucl. Mater.* 423(1–3):79–86
60. Zhang J. 2009. A review of steel corrosion by liquid lead and lead-bismuth
61. Klok O, Lambrinou K, Gavrilov S, Stergar E, Lim J, et al. 2018. Effect of deformation twinning on dissolution corrosion of 316L stainless steels in contact with static liquid lead-bismuth eutectic (LBE) at 500 °C. *J. Nucl. Mater.* 510:556–67
62. Tsisar V, Schroer C, Wedemeyer O, Skrypnik A, Konys J. 2016. Long-term corrosion of austenitic steels in flowing LBE at 400 °C and 10-7 mass% dissolved oxygen in comparison with 450 and 550 °C. *J. Nucl. Mater.* 468:305–12
63. Lambrinou K, Koch V, Coen G, Van Den Bosch J, Schroer C. 2014. Corrosion scales on various steels after exposure to liquid lead-bismuth eutectic. *J. Nucl. Mater.* 450(1–3):244–55
64. Schroer C, Nold E, Konys J. 2009. Micro-Analysis of 316L Stainless-Steel After Long-Term Exposure to Lead-Bismuth Eutectic at 550 C
65. He BX, Li N, Mineev M. 2001. A kinetic model for corrosion and precipitation in non-isothermal LBE flow loop. *J. Nucl. Mater.* 297(2):214–19
66. Malkow T, Steiner H, Muscher H, Konys J. 2004. Mass transfer of iron impurities in LBE loops under non-isothermal flow conditions
67. Aerts A, Lim J, Rosseel K, Marino A, Gonzalez Prieto B, et al. 2018. The conditioning and

chemistry programme for myrrha
68. Martín FJ, Soler L, Hernández F, Gómez-Briceño D. 2004. Oxide layer stability in lead–bismuth at high temperature. *J. Nucl. Mater.* 335(2):194–98
69. Hosemann P, Dickerson R, Dickerson P, Li N, Maloy SA. 2013. Transmission electron microscopy (TEM) on oxide layers formed on D9 stainless steel in lead bismuth eutectic (LBE). *Corros. Sci.* 66:196–202
70. Hosemann P, Hofer C, Hlawacek G, Li N, Maloy SA, Teichert C. 2012. Structural, electrical and magnetic measurements on oxide layers grown on 316L exposed to liquid lead-bismuth eutectic. *J. Nucl. Mater.* 421(1–3):140–46
71. Charalampopoulou E, Delville R, Verwerft M, Lambrinou K, Schryvers D. 2019. Transmission electron microscopy study of complex oxide scales on DIN 1.4970 steel exposed to liquid Pb-Bi eutectic. *Corros. Sci.* 147:22–31
72. Hosemann P, Hawley ME, Koury D, Welch J, Johnson AL, et al. 2008. Nanoscale characterization of HT-9 exposed to lead bismuth eutectic at 550 °C for 3000 h. *J. Nucl. Mater.* 381(3):211–15
73. Jianu A, Fetzer R, Weisenburger A, Doyle S, Bruns M, et al. 2016. Stability domain of alumina thermally grown on Fe-Cr-Al-based model alloys and modified surface layers exposed to oxygen-containing molten Pb. *J. Nucl. Mater.* 470:68–75
74. Heinzel A, Kondo M, Takahashi M. 2006. Corrosion of steels with surface treatment and Al-alloying by GESA exposed in lead-bismuth. *J. Nucl. Mater.* 350(3):264–70
75. Martinelli L, Balbaud-Célérier F, Terlain A, Delpech S, Santarini G, et al. 2008. Oxidation mechanism of a Fe-9Cr-1Mo steel by liquid Pb-Bi eutectic alloy (Part I). *Corros. Sci.* 50(9):2523–36
76. Martinelli L, Balbaud-Célérier F, Picard G, Santarini G. 2008. Oxidation mechanism of a Fe-9Cr-1Mo steel by liquid Pb-Bi eutectic alloy (Part III). *Corros. Sci.* 50(9):2549–59
77. Schroer C, Skrypnik A, Wedemeyer O, Konys J. 2012. Oxidation and dissolution of iron in flowing lead-bismuth eutectic at 450°C. *Corros. Sci.* 61:63–71
78. Schroer C, Wedemeyer O, Skrypnik A, Novotny J, Konys J. 2012. Corrosion kinetics of Steel T91 in flowing oxygen-containing lead–bismuth eutectic at 450 °C. *J. Nucl. Mater.* 431(1–3):105–12
79. Martinelli L, Ginestar K, Botton V, Delisle C, Balbaud-Célérier F. 2020. Corrosion of T91 and pure iron in flowing and static Pb-Bi alloy between 450 °C and 540 °C: experiments, modelling and mechanism. *Corros. Sci.* 176:108897
80. Birks N, Meier GH, Pettit FS. 2006. *Introduction to the high temperature oxidation of metals*, Vol. 9780521480. Cambridge University Press. 1–338 pp. 2nd ed.
81. Yeliseyeva O, Tsisar V. 2008. Kinetic features of iron oxidation in liquid lead saturated with oxygen below and above the chaudron point (570 °C). *Oxid. Met.* 70(3–4):213–27
82. Kurata Y, Futakawa M, Saito S. 2005. Comparison of the corrosion behavior of austenitic and ferritic/martensitic steels exposed to static liquid Pb–Bi at 450 and 550 °C. *J. Nucl. Mater.* 343(1–3):333–40
83. Aerts A, Gladinez K, Prieto BG, Lim J, Marino A, Rosseel K. 2020. The LBE Coolant Chemistry R&D Programme for the MYRRHA ADS: Chemistry and Control of Oxygen, Corrosion and Spallation Products
84. Li N. 2002. Active control of oxygen in molten lead–bismuth eutectic systems to prevent steel corrosion and coolant contamination. *J. Nucl. Mater.* 300(1):73–81
85. Une K, Hirai M, Nogita KAA, Hosokawa T, Suzawa Y, et al. 2000. Rim structure formation

and high burnup fuel behavior of large-grained UO2 fuels. *J. Nucl. Mater.* 278(1):54–63
86. Scott P. 1994. A review of irradiation assisted stress corrosion cracking
87. Andresen PL, Was GS. 2019. Irradiation Assisted Stress Corrosion Cracking. In *Comprehensive Nuclear Materials*, pp. 190–217. Elsevier
88. Chopra OK, Rao AS. 2011. A review of irradiation effects on LWR core internal materials - IASCC susceptibility and crack growth rates of austenitic stainless steels. *J. Nucl. Mater.* 409(3):235–56
89. Garner FA. 2020. Radiation-Induced Damage in Austenitic Structural Steels Used in Nuclear Reactors. In *Comprehensive Nuclear Materials - 2nd Edition*, ed RJM Konings. Elsevier
90. Bruemmer SM, Simonen EP, Scott PM, Andresen PL, Was GS, Nelson JL. 1999. Radiation-induced material changes and susceptibility to intergranular failure of light-water-reactor core internals
91. Garner FA, Porollo SI, Vorobjev AN, Konobeev V, Dvoriashin AM. 1999. Void Swelling at Low Displacement Rates in Annealed X18H10T Stainless Steel at 30-56 DPA and 280-332 °C
92. Betova I, Bojinov M, Kinnunen P, - al, Fushimi K, et al. 1980. Self-diffusion in austenitic Fe-Cr-Ni alloys. *J. Phys. F Met. Phys.* 10(3):383
93. Esmailzadeh B, Kumar A, Garner FA. 1985. The influence of silicon on void nucleation in irradiated alloys. *J. Nucl. Mater.* 133–134(C):590–93
94. Okamoto PR, Rehn LE. 1979. Radiation-induced segregation in binary and ternary alloys. *J. Nucl. Mater.* 83(1):2–23
95. Allen TR, Was GS. 2007. Radiation-Enhanced Diffusion and Radiation-Induced Segregation. In *Radiation Effects in Solids*, pp. 123–51. Springer Netherlands
96. Mansur LK, Grossbeck ML. 1988. Mechanical property changes induced in structural alloys by neutron irradiations with different helium to displacement ratios. *J. Nucl. Mater.* 155–157(PART 1):130–47
97. Joseph JM, Choi BS, Yakabuskie P, Wren JC. 2008. A combined experimental and model analysis on the effect of pH and O2(aq) on γ-radiolytically produced H2 and H2O2. *Radiat. Phys. Chem.* 77(9):1009–20
98. Zinkle SJ, Maziasz PJ, Stoller RE. 1993. Dose dependence of the microstructural evolution in neutron-irradiated austenitic stainless steel. *J. Nucl. Mater.* 206(2–3):266–86
99. Johnston WG, Rosolowski JH, Turkalo AM, Lauritzen T. 1974. An experimental survey of swelling in commercial Fe-Cr-Ni alloys bombarded with 5 MeV Ni Ions. *J. Nucl. Mater.* 54(1):24–40
100. Garner FA, Kumar AS. 1987. The Influence of Both Major and Minor Element Composition on Void Swelling in Austenitic Steels
101. Garner FA, Gelles D. 1990. Neutron-Induced Swelling of Commercial Alloys at Very High Exposures
102. Coghlan WA, Garner FA. 1987. Effect of nickel content on the minimum critical void radius in ternary austenitic alloys
103. Yvon P, Carré F. 2009. Structural materials challenges for advanced reactor systems. *J. Nucl. Mater.* 385(2):217–22
104. Zinkle SJ, Was GS. 2013. Materials challenges in nuclear energy. *Acta Mater.* 61(3):735–58
105. Anderoglu O, Byun TS, Toloczko M, Maloy SA. 2013. Mechanical performance of ferritic

martensitic steels for high dose applications in advanced nuclear reactors. *Metall. Mater. Trans. A Phys. Metall. Mater. Sci.* 44(SUPPL. 1):70–83
106. Alamo A, Bertin JL, Shamardin VK, Wident P. 2007. Mechanical properties of 9Cr martensitic steels and ODS-FeCr alloys after neutron irradiation at 325 °C up to 42 dpa. *J. Nucl. Mater.* 367–370(SPEC. ISS.):54–59
107. Kohyama A, Hishinuma A, Gelles DS, Klueh RL, Dietz W, Ehrlich K. 1996. Low-activation ferritic and martensitic steels for fusion application. *J. Nucl. Mater.* 233–237(PART 1):138–47
108. Tan L, Kim BK, Yang Y, Field KG, Gray S, Li M. 2017. Microstructural evolution of neutron-irradiated T91 and NF616 to ~4.3 dpa at 469 °C. *J. Nucl. Mater.* 493:12–20
109. Proriol Serre I, Vogt JB. 2020. Liquid metal embrittlement sensitivity of the T91 steel in lead, in bismuth and in lead-bismuth eutectic. *J. Nucl. Mater.* 531:152021
110. Li N, He X, Rusanov A, Demishonkov AP. 2002. Corrosion Test of US Steels in Lead-Bismuth Eutectic (LBE) and Kinetic Modeling of Corrosion in LBE systems, Report to Los Alamos National Laboratory
111. Hosemann P, Thau HT, Johnson AL, Maloy SA, Li N. 2008. Corrosion of ODS steels in lead–bismuth eutectic. *J. Nucl. Mater.* 373(1–3):246–53
112. Maeda S. 2011. Status of the development of fast breeder reactor fuels in FaCT project
113. Cox B. 2005. Some thoughts on the mechanisms of in-reactor corrosion of zirconium alloys. *J. Nucl. Mater.* 336(2–3):331–68
114. Eichenberg JD, Lieberman RM, Mrazik FP. 1960. Irradiation of UO2 Fuel Rods - The XII Experiment. *WAPD-208*, April
115. Dalgaard SB. 1962. Corrosion and hydriding behaviour of some Zr 2.5 wt% Nb alloys in water, steam and various gases at high temperature. Chalk River, Ontario, Canada
116. Johnson, Jr A. 1977. Behavior of spent nuclear fuel in water pool storage. Richland, WA (United States)
117. Burns W, Maffei H. 1962. Neutron Irradiation and Cold Work Effects on Zircaloy-2 Corrosion and Hydrogen Pickup. In *Corrosion of Zirconium Alloys*, pp. 101–17. West Conshohocken, PA: ASTM International
118. Asher RC, Davies D, Kirstein TBA, McCullen PAJ, White JF. 1970. The effects of radiation on the corrosion of some Zr alloys. *Corros. Sci.* 10(10):695–707
119. Jenks GH. 1961. *Review and correlation of in-pile zircaloy-2 corrosion data and a model for the effect of irradiation*. Oak Ridge National Laboratory
120. Was GS, Andresen PL. 2012. *Irradiation assisted corrosion and stress corrosion cracking (IAC/IASCC) in nuclear reactor systems and components*. Elsevier Ltd. 131–185 pp.
121. Bradhurst DH, Shirvington PJ, Heuer PM. 1973. The effects of radiation and oxygen on the aqueous oxidation of zirconium and its alloys at 290 °C. *J. Nucl. Mater.* 46(1):53–76
122. Lysell G, Nystrand A-C, Ullberg M. 2005. Shadow Corrosion Mechanism of Zircaloy
123. Was GS, Busby JT, Allen T, Kenik EA, Jensson A, et al. 2002. Emulation of neutron irradiation effects with protons: Validation of principle. *J. Nucl. Mater.* 300(2–3):198–216
124. Hillner E, Franklin DG, Smee JD. 2000. Long-term corrosion of Zircaloy before and after irradiation. *J. Nucl. Mater.* 278(2):334–45
125. Marlowe MO. 1985. Nuclear fuel cladding localized corrosion
126. Kondou K, Hasegawa A, Abe K. 2004. Study on irradiation induced corrosion behavior in austenitic stainless steel using hydrogen-ion bombardment
127. Johnson ABJ, Irvin JE. 1967. Radiation-enhanced oxidation of Zircaloy-2 in pH-10 LiOH

and pH-10 NH4OH. Pacific Northwest Laboratory, Richland, WA (United States)
128. Kammenzind BF, Gruber JA, Bajaj R, Smee JD. 2018. Neutron irradiation effects on the corrosion of zircaloy-4 in a pressurized water reactor environment
129. Cheng B, Adamson RB. 1987. Mechanistic studies of Zircaloy nodular corrosion
130. Etoh Y, Shimada S. 1992. Irradiation-Induced Dissolution of Precipitates in Zircaloy-2. *J. Nucl. Sci. Technol.* 29(4):353–66
131. Kruger RM, Adamson RB. 1993. Precipitate behavior in zirconium-based alloys in BWRs. *J. Nucl. Mater.* 205:242–50
132. Howlader MMR, Kinoshita C, Shiiyama K, Kutsuwada M, Inagaki M. 1999. In situ measurement of electrical conductivity of Zircaloy oxides and their formation mechanism under electron irradiation. *J. Nucl. Mater.* 265(1–2):100–107
133. Cox B, Sheikh HI. 1997. Redistribution of the alloying elements during Zircaloy-2 oxidation. *J. Nucl. Mater.* 249(1):17–32
134. Kritsky VG, Petrik NG, Berezina IG, Doilnitsina Vnipiet V V. 1993. Effect of Water Chemistry and Fuel Operation Parameters on Zr + 1% Nb Cladding Corrosion
135. Christensen H. 1981. Effect of water radiolysis on corrosion in nuclear reactors. *Radiat. Phys. Chem.* 18(1–2):147–58
136. Was GS, Andresen PL. 2007. Stress corrosion cracking behavior of alloys in aggressive nuclear reactor core environments
137. Raiman SS, Wang P, Was GS. 2017. Irradiation Accelerated Corrosion of Stainless Steel and Ferritic-Martensitic Steel in Simulated Primary Water
138. Raiman SS, Bartels DM, Was GS. 2017. Radiolysis driven changes to oxide stability during irradiation-corrosion of 316L stainless steel in high temperature water. *J. Nucl. Mater.* 493:40–52
139. Raiman SS, Was GS. 2017. Accelerated corrosion and oxide dissolution in 316L stainless steel irradiated in situ in high temperature water. *J. Nucl. Mater.* 493:207–18
140. Haubenreich PN, Engel JR. 1970. Experience with the Molten-Salt Reactor Experiment. *Nucl. Appl. Technol.* 8(2):118–36
141. Hammer-Rotzler B, Neuhausen J, Boutellier V, Wohlmuther M, Zanini L, et al. 2016. Distribution and surface enrichment of radionuclides in lead-bismuth eutectic from spallation targets. *Eur. Phys. J. Plus 2016 1317*. 131(7):1–18
142. Zhou W, Yang Y, Zheng G, Woller KB, Stahle PW, et al. 2020. Proton irradiation-decelerated intergranular corrosion of Ni-Cr alloys in molten salt. *Nat. Commun.* 11(1):1–7
143. Ezell NDB, Raiman SS, Kurley JM, McDuffee J. 2020. Neutron Irradiation of Alloy N and 316L Stainless Steel in Contact with a Molten Chloride Salt. *Nucl. Eng. Technol.*
144. Wang S, Zhang S, Xie J, Feng X, Song M, et al. 2022. Clarifying the mitigation effect of proton irradiation on the intergranular oxidation of 316L stainless steel in high temperature water. *Acta Mater.* 241:118408
145. Glasbrenner H, Brütsch R, Dai Y, Gröschel F, Martin M. 2006. Post-irradiation examination on LiSoR 3 experiment. *J. Nucl. Mater.* 356(1–3):247–55
146. Glasbrenner H, Gröschel F. 2007. Liquid metal compatibility under irradiation: The LiSoR 5 experiment. *J. Nucl. Mater.* 367-370 B(SPEC. ISS.):1590–95
147. Glasbrenner H, Dai Y, Gröschel F. 2005. LiSoR irradiation experiments and preliminary post-irradiation examinations. *J. Nucl. Mater.* 343(1–3):267–74
148. Frazer D, Qvist S, Parker S, Krumwiede DL, Caro M, et al. 2016. Degradation of HT9 under simultaneous ion beam irradiation and liquid metal corrosion. *J. Nucl. Mater.* 479:382–89

149. Chen Q, Chen Y, Zhang F, Yang J, Zhu C, et al. 2023. In-situ proton irradiation/lead-bismuth eutectic corrosion synergistic effect on corrosion behaviour of 11Cr1W1Si ferritic/martensitic steel. *J. Nucl. Mater.* 573:154097
150. Yao C, Wang Z, Zhang H, Chang H, Sheng Y, et al. 2019. HLMIF, a facility for investigating the synergistic effect of ion-irradiation and LBE corrosion. *J. Nucl. Mater.* 523:260–67
151. Yao C, Zhang H, Chang H, sheng Y, Shen T, et al. 2022. Structure of surface oxides on martensitic steel under simultaneous ion irradiation and molten LBE corrosion. *Corros. Sci.* 195:109953
152. Gavrilov S, Lambrecht M, Stergar E, Eremin S, Zhemkov I, et al. 2016. Deliverable D3.9a -- PIE of LEXUR II LBE capsules
153. Was GS. 2015. Challenges to the use of ion irradiation for emulating reactor irradiation. *J. Mater. Res.* 30(9):1158–82
154. Zheng G, Carpenter D, Hu L-W, Sridharan K. 2016. High Temperature Corrosion of Structural Alloys in Molten Li $_2$ BeF $_4$ (FLiBe) Salt. In *Advances in Materials Science for Environmental and Energy Technologies V: Ceramic Transactions*. 260:93–101. Hoboken, NJ, USA: John Wiley & Sons, Inc.
155. Wang P, Nowotka K, Was GS. 2022. Reproducing shadow corrosion on Zircaloy-2 using in-situ proton irradiation. *J. Nucl. Mater.* 558:153406
156. Hosemann P, Greco RR, Usov I, Wang Y, Maloy SA, Li N. 2008. The design, setup and operational testing of the irradiation and corrosion experiment (ICE). *J. Nucl. Mater.* 376(3):392–95
157. Qvist S, Bolind AM, Hosemann P, Wang Y, Tesmer J, et al. 2013. Capability demonstration of simultaneous proton beam irradiation during exposure to molten lead-bismuth eutectic for HT9 steel. *Nucl. Instruments Methods Phys. Res. Sect. A Accel. Spectrometers, Detect. Assoc. Equip.* 698:98–105
158. Dai Y, Wohlmuther M, Boutellier V, Hahl S, Lagotzki A, et al. 2016. Non-destructive testing of the MEGAPIE target. *J. Nucl. Mater.* 468:221–27
159. Saito S, Suzuki K, Hatakeyama Y, Suzuki M, Dai Y. 2020. Experimental validation of tensile properties measured with thick samples taken from MEGAPIE target. *J. Nucl. Mater.* 534:152146
160. Fazio C, Van den Bosch, Joris Muñoz FJM, Henry J, Roelofs F, Turroni P, et al. 2011. Technology and Components of Accelerator-driven Systems
161. Fazio C, Briceno DG, Rieth M, Gessi A, Henry J, Malerba L. 2011. Innovative materials for Gen IV systems and transmutation facilities: The cross-cutting research project GETMAT
162. Bauer GS, Salvatores M, Heusener G. 2001. MEGAPIE, a 1 MW pilot experiment for a liquid metal spallation target. *J. Nucl. Mater.* 296(1–3):17–33
163. Wagner W, Dai Y, Glasbrenner H, Aebersold HU. 2007. Materials irradiation facilities at the high-power Swiss proton accelerator complex. *J. Nucl. Mater.* 361(2-3 SPEC. ISS.):274–81
164. Kirchner T, Bortoli Y, Cadiou A, Foucher Y, Stutzmann JS, et al. 2003. LiSoR, a liquid metal loop for material investigation under irradiation. *J. Nucl. Mater.* 318(SUPPL):70–83
165. Lillard RS, Paciotti M, Tcharnotskaia V. 2004. The influence of proton irradiation on the corrosion of HT-9 during immersion in lead bismuth eutectic. *J. Nucl. Mater.* 335(3):487–92

166. Bates JF, Powell RW. 1981. Irradiation-induced swelling in commercial alloys. *J. Nucl. Mater.* 102(1–2):200–213
167. Sencer BH, Garner FA. 2000. Compositional and temperature dependence of void swelling in model Fe–Cr base alloys irradiated in the EBR-II fast reactor. *J. Nucl. Mater.* 283–287(PART I):164–68
168. Garner FA, Toloczko MB, Sencer BH. 2000. Comparison of swelling and irradiation creep behavior of fcc-austenitic and bcc-ferritic/martensitic alloys at high neutron exposure. *J. Nucl. Mater.* 276(1–3):123–42
169. Simons RL, Brager HR, Matsumoto WY. 1986. Design of a single variable helium effects experiment for irradiation in FFTF using alloys enriched in nickel-59. *J. Nucl. Mater.* 141–143(PART 2):1057–60
170. Ziegler JF, Ziegler MD, Biersack JP. 2010. SRIM - The stopping and range of ions in matter (2010). *Nucl. Instruments Methods Phys. Res. Sect. B Beam Interact. with Mater. Atoms.* 268(11–12):1818–23
171. Konobeyev AY, Fischer U, Korovin YA, Simakov SP. 2017. Evaluation of effective threshold displacement energies and other data required for the calculation of advanced atomic displacement cross-sections. *Nucl. Energy Technol.* 3(3):169–75
172. Stoller RE, Toloczko MB, Was GS, Certain AG, Dwaraknath S, Garner FA. 2013. On the use of SRIM for computing radiation damage exposure. *Nucl. Instruments Methods Phys. Res. Sect. B Beam Interact. with Mater. Atoms*. 310:75–80
173. Micro to Nano. 2022. *FlowView Aquirius liquid sample chamber for SEM*. https://www.microtonano.com/Flowview-Aqaurius-liquid-sample-chamber-for-SEM.php
174. Larson Electronic Glass. 2022. *Sapphire Viewports*. https://www.larsonelectronicglass.com/sapphire-viewports-p-136-l-en.html
175. Goodfellow. 2022. *Products*. https://www.goodfellow.com/us/en-us
176. Sooby ES. 2014. *Experimental and Computational Investigations of Candidate Fuel Salt Melt Properties and Corrosion and Irradiation Damage in Nickel for a Molten Chloride Fission System*. Texas A&M
177. National Electrostatics Corp. 2022. *Source of Negative Ions by Cesium Sputtering (SNICS)*. https://www.pelletron.com/products/snics/
178. Schmidt F, Chancey M, Kim H, Wang Y, Hosemann P. 2021. Continuous Monitoring of Pure Fe Corrosion in Lead-Bismuth Eutectic Under Irradiation with Proton-Induced X-ray Emission Spectroscopy. *JOM*. 73(12):4041–50
179. Folkmann F, Gaarde C, Huus T, Kemp K. 1974. Proton induced X-ray emission as a tool for trace element analysis. *Nucl. Instruments Methods*. 116(3):487–99
180. Johansson SAE, Johansson TB. 1976. Analytical application of particle induced X-ray emission. *Nucl. Instruments Methods*. 137(3):473–516
181. Maenhaut W. 2019. X-Ray Fluorescence and Emission | Particle-Induced X-Ray Emission. In *Encyclopedia of Analytical Science*, pp. 432–42. Elsevier
182. Mesjasz-Przybylowicz J, Przybylowicz WJ. 2002. Micro-PIXE in plant sciences: Present status and perspectives. *Nucl. Instruments Methods Phys. Res. Sect. B Beam Interact. with Mater. Atoms*. 189(1–4):470–81
183. Campbell JL, Higuchi D, Maxwell JA, Teesdale WJ. 1993. Quantitative PIXE microanalysis of thick specimens. *Nucl. Instruments Methods Phys. Res. Sect. B Beam Interact. with Mater. Atoms*. 77(1–4):95–109
184. Campbell J, Perujo A, Teesdale W, Maxwell J. 1987. Analysis of Thick Targets by Proton-

Induced X-Ray Emission. *Scanning Microsc.* 1(4):
185. Amptek. 2022. *FAST SDD® Ultra High Performance Silicon Drift Detector*. https://www.amptek.com/products/x-ray-detectors/fastsdd-x-ray-detectors-for-xrf-eds/fastsdd-silicon-drift-detector
186. Amptek. 2022. Understanding Acquisition Time, Live Time, and all that
187. Demortier G, Mathot S, Van Oystaeyen B. 1990. Complementarity of RBS, PIGE and PIXE for the determination of surface layers of thicknesses up to 30 microns. *Nucl. Instruments Methods Phys. Res. Sect. B Beam Interact. with Mater. Atoms*. 49(1–4):46–51
188. Choi HW, Kim YS, Kim GD, Woo HJ, Kim JK, Lee GH. 1998. Analysis of chlorine in used oils by external beam PIXE-PIGE. *Nucl. Instruments Methods Phys. Res. Sect. B Beam Interact. with Mater. Atoms*. 136–138:1018–22
189. Räisänen J. 2009. Particle Induced Gamma Emission Data. In *Handbook of Moder Ion Beam Materials Analysis*, ed YQ Wang, M Nastasi. 7(2):177–223. Materials Research Society
190. Nuclear Data Service. 2022. *IBANDL*. https://www-nds.iaea.org/exfor/ibandl.htm
191. Amptek. 2020. PX5 User Manual and Operating Instructions
192. Kim H, Chancey MR, Chung T, Brackenbury I, Liedke MO, et al. 2022. Interface effect of Fe and Fe2O3on the distributions of ion induced defects. *J. Appl. Phys.* 132(10):105901
193. Yang Y, Zhou W, Yin S, Wang SY, Yu Q, et al. 2022. One Dimensional Wormhole Corrosion in Metals. *arXiv*
194. Hombourger B, Křepel J, Pautz A. 2019. Breed-and-burn fuel cycle in molten salt reactors. *EPJ Nucl. Sci. Technol.* 5:15
195. Andreades C, Cisneros AT, Choi JK, Chong AYK, Fratoni M, et al. 2016. Design summary of the Mark-I pebble-bed, fluoride salt-cooled, high-temperature reactor commercial power plant. *Nucl. Technol.* 195(3):223–38
196. Serp J, Allibert M, Beneš O, Delpech S, Feynberg O, et al. 2014. The molten salt reactor (MSR) in generation IV: Overview and perspectives. *Prog. Nucl. Energy*. 77:308–19
197. Tzvetkoff T, Kolchakov J. 2004. Mechanism of growth, composition and structure of oxide films formed on ferrous alloys in molten salt electrolytes - A review. *Mater. Chem. Phys.* 87(1):201–11
198. Kurata Y, Futakawa M, Saito S. 2008. Corrosion behavior of steels in liquid lead–bismuth with low oxygen concentrations. *J. Nucl. Mater.* 373(1–3):164–78
199. Aerts A, Gavrilov S, Manfredi G, Marino A, Rosseel K, Lim J. 2016. Oxygen-iron interaction in liquid lead-bismuth eutectic alloy. *Phys. Chem. Chem. Phys*. 18:19526
200. Yano KH, Kohnert AA, Kaspar TC, Taylor SD, Spurgeon SR, et al. 2022. Dose rate dependent cation & anion radiation enhanced diffusion in hematite. *J. Mater. Chem. A.* 10(45):24167–77
201. Wang P, Was GS. 2015. Oxidation of Zircaloy-4 during in situ proton irradiation and corrosion in PWR primary water. *J. Mater. Res*. 30(9):1335–48
202. Bartels D. 2018. Assessment of Corrosion Resistance of Candidate Alloys for Accident Tolerant Fuel Cladding under Reactor Conditions -- Final Report
203. Wang P, Was GS. 2019. In-situ proton irradiation-corrosion study of ATF candidate alloys in simulated PWR primary water
204. Allen TR, Cole JI, Kenik EA, Tsai H, Ukai S, et al. 1999. Using fast reactor component evaluation for pressurized water reactor life extension. *JOM*. 51(10):27–30
205. Dai Y, Glasbrenner H, Boutellier V, Bruetsch R, Jia X, Groeschel F. 2004. Preliminary

results of post-irradiation examinations on LiSoR-2 test section. *J. Nucl. Mater.* 335(2 SPEC. ISS.):232–38
206. Bakai AS. 2008. Combined Effect of Molten Fluoride Salt and Irradiation on Ni-based Alloys
207. Mendelev MI, Mishin Y. 2009. Molecular dynamics study of self-diffusion in bcc Fe. *Phys. Rev. B - Condens. Matter Mater. Phys.* 80(14):144111
208. Starikov S, Mrovec M, Drautz R. 2020. Study of grain boundary self-diffusion in iron with different atomistic models. *Acta Mater.* 188:560–69
209. Parkinson GS. 2016. Iron oxide surfaces. *Surf. Sci. Rep.* 71(1):272–365
210. García J, Subías G. 2004. The Verwey transition—a new perspective. *J. Phys. Condens. Matter*. 16(7):R145
211. Atkinson A, O'Dwyer ML, Taylor RI. 1983. 55Fe diffusion in magnetite crystals at 500° C and its relevance to oxidation of iron. *J. Mater. Sci.* 18(8):2371–79
212. Dieckmann R, Schmalzried H. 1977. Defects and Cation Diffusion in Magnetite (I). *Berichte der Bunsengesellschaft für Phys. Chemie*. 81(3):344–47
213. Lewis G V., Catlow CRA, Cormack AN. 1985. Defect structure and migration in Fe3O4. *J. Phys. Chem. Solids*. 46(11):1227–33
214. Crouch AG, Robertson J. 1990. Creep and oxygen diffusion in magnetite. *Acta Metall. Mater.* 38(12):2567–72
215. Owusu-Mensah M, Cooper J, Morales AL, Yano K, Taylor SD, et al. 2022. Surprisingly high irradiation-induced defect mobility in Fe3O4 as revealed through in situ transmission electron microscopy. *Mater. Charact.* 187:111863
216. Meillon S, Dunstetter F, Pascard H, Rodriguez-Carvajal J. 1997. Fast Neutron Irradiated Magnetite and Haematite Investigated by Neutron Diffraction. *J PHYS WFRANCE*. 7:
217. Meillon S, Studer F, Hervieu M, Pascard H. 1996. Changes in magnetic properties of magnetite Fe3O4 ceramics induced by high energy heavy ion irradiation. *Nucl. Instruments Methods Phys. Res. Sect. B Beam Interact. with Mater. Atoms*. 107(1–4):363–67
218. Yastrebinskii RN, Bondarenko GG, Pavlenko VI. 2016. Radiation resistance of structural radiation-protective composite material based on magnetite matrix. *Inorg. Mater. Appl. Res.* 7(5):23–29
219. Yano KH, Kohnert AA, Banerjee A, Edwards DJ, Holby EF, et al. 2021. Radiation-Enhanced Anion Transport in Hematite. *Chem. Mater.* 33(7):2307–18
220. Gleiter H. 1969. The Mechanism of Grain Boundary Migration. *Acta Metall.* 17(5):565–73
221. Barr CM, El-Atwani O, Kaoumi D, Hattar K. 2019. Interplay Between Grain Boundaries and Radiation Damage. *JOM*. 71(4):1233–44
222. OSHA. 2021. *Lead*. https://www.cdc.gov/niosh/topics/lead/limits.html
223. Thompson AC, Attwood DT, Gullikson EM, Howells MR, Kortright JB, et al. 2001. *X-ray Data Booklet. Vol. 8. No. 4*. Berkeley, CA: Lawrence Berkeley National Laboratory, University of California
224. Wang YQ, Nastasi M. 2009. *Handbook of Modern Ion Beam Materials Analysis*. Warrendale, PA: Materials Research Society. 2nd ed.
225. NIST. 2022. *X-Ray Mass Attenuation Coefficients*. https://physics.nist.gov/PhysRefData/XrayMassCoef/tab3.html
226. Ghoneim MM, Munz D. 1997. Fracture toughness of MANET II steel. *Int. J. Press. Vessel. Pip.* 74(2):89–96

8. Appendix

8.1. Pb saturation concentrations in air with LBE temperature

The saturation vapor pressure of pure Pb, pure Bi, and LBE are relatively well understood (see equations 2.16, 2.17, and 2.18 in (21)). Figure 46 shows the saturation vapor pressure for the three metals. The concentration of Pb in the air above liquid LBE can be estimated either by calculating the fraction of Pb present in the LBE in the gas phase or by calculating the partial pressure of Pb in LBE, p_{Pb}, with Raoult's law:

$$p_{Pb} = \chi_{Pb}\, p^0_{Pb}\,,$$

where χ_{Pb} is the mole fraction of Pb in LBE (0.45) and p^0_{Pb} is the vapor pressure of pure Pb. The sum of the partial pressure of Pb and Bi should be equal to the vapor pressure of LBE if it can be considered an ideal mixture. Figure 46 shows that applying Raoult's law leads to a small overestimate of the LBE vapor pressure, which reflects the high vapor pressure of Bi.

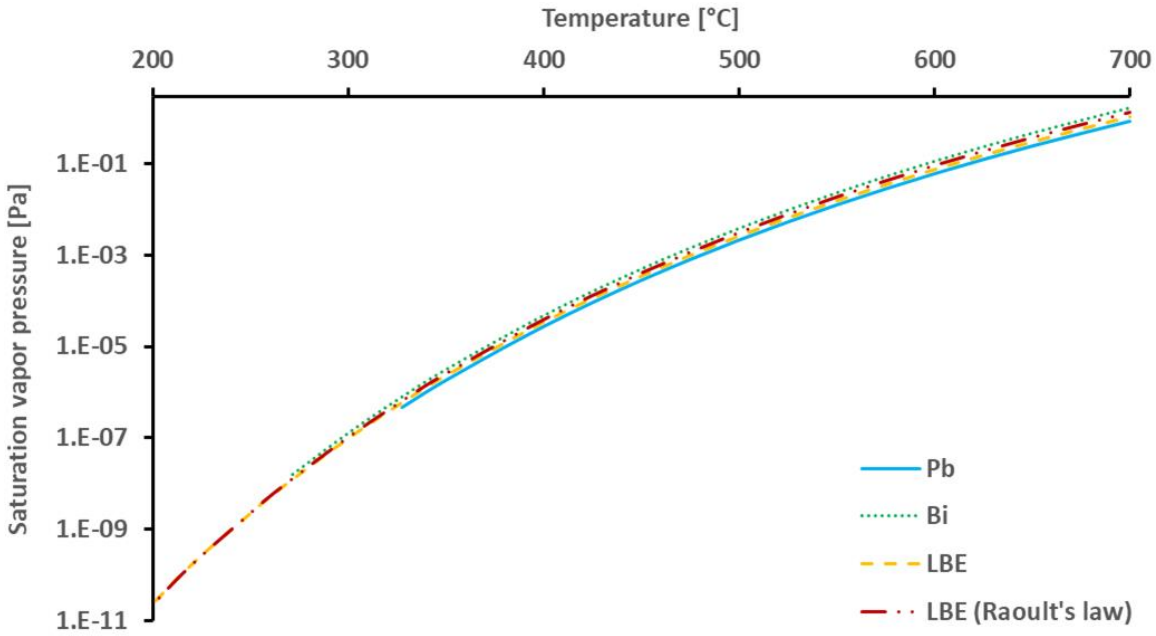

Figure 46 – Semi log plot of the saturation vapor pressure of pure Pb, Bi, and LBE with temperature based on equations in (21). The vapor pressure of LBE more closely follows that of pure Pb than pure Bi.

The Pb concentration, $c_{Pb,air}$, in µg/m^3 can be obtained with the help of the ideal gas law ($pV = nRT$), where V is the gas volume in m^3, n is the number of atoms in mol, R is the gas constant (8.314 m^3 Pa/(K mol)), and T is the temperature in K:

$$c_{Pb,air} = w_{Pb,LBE}\, M_{LBE}\, \frac{p_{LBE}}{RT}\,.$$

$w_{Pb,LBE}$ is the mass fraction of Pb in LBE (0.445) and M_{LBE} is the molar mass of LBE (208 g/mol). The concentration of Pb can also be obtained from the partial pressure of Pb based on Raoult's law in an analogous manner (with a molar mass of Pb of 207.2 g/mol). Both estimates

and the OSHA (Occupational Safety and Health Administration) action limit (AL, 30 µg/m^3, see (222)) and permissible exposure limit (PEL, 50 µg/m^3) for Pb in air are shown in Figure 47. Since these limits are time weight averages, a worker would have to breathe in air saturated with vapor from LBE at 500 °C for 8 hours to exceed the AL.

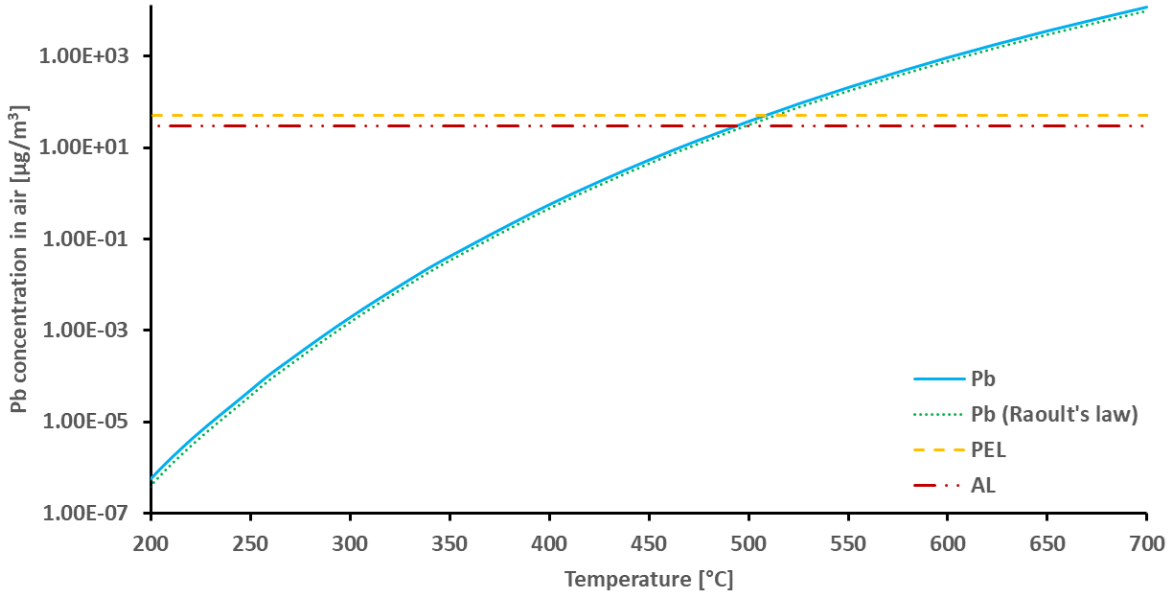

Figure 47 – Semi log plot of calculated Pb concentrations in air with LBE temperature. For comparison, the OSHA AL and the PEL are shown.

8.2. Metals solubilities in Pb and Pb-Bi eutectic

Table 9 – Solubilities of elements based on recommendations in Table 3.5.1 in (21).

	Pb				LBE			
Element	**A**	**B**	**T [K]**	**Reference**	**A**	**B**	**T**	**Reference**
Fe	2.11	5225	600-1173	Gosse, 2014	1.85	4164	823-1053	Handbook based on Weeks, 1969
					2.00	4399	399-1173	Gosse, 2014
Cr	3.62	6648	601-1773	Gosse, 2014	1.12	3056	399-1173	Gosse, 2014
	3.7	6720	1173-1473	Venkatraman, 1988	1.07	3022	643-813	Courouau, 2004
	3.74	6750	1181-1483	Tecdoc, 2002, Alden, 1958	-0.02	2280	673-773	Tecdoc, 2002, Matrynov, 1998
Ni	1.36	1395	598-917	Gosse, 2014	4.32	2933	528-742	Gosse, 2014
					5.2	3500	603-712	Martinelli, 2010
					1.7	1009	712-1173	Martinelli, 2010
					1.74	1006	742-1173	Gosse, 2014

8.3. Compositions of relevant structural materials

Table 10 – Nominal compositions of steels mentioned throughout the text (in wt%) with Fe as balance based on (45).

Type	Alloy	Cr	Ni	C	Mo	Mn	Si	Other
Austenitic	AISI 304	18.5	9.35	0.07	0.02	1.55	0.48	
	AISI 304L	18.3	9.26	0.03	0.02	1.37	0.62	
	AISI 316	17.3	13.7	0.05	2.26	1.64	0.56	
	DIN 1.4970 (15-15Ti)	14.9	15.2	0.10	1.24	1.75	0.40	Ti = 0.48
Ferritic	EM10	8.76	0.18	0.105	1.05	0.48	0.37	N = 0.024
	HT-9	12.0	0.47	0.020	1.03	0.50	0.41	W = 0.5 V = 0.32
	MANET II*	10.37	0.65	0.10	0.58	0.76	0.18	V = 0.21 Nb = 0.16
	T-91 (9Cr-1Mo)	8.61	0.09	0.081	0.89	0.37	0.11	Nb = 0.07 V = 0.21

* From (226)

8.4. X-ray energies of relevant elements

Table 11 – X-ray energies (in keV) for elements discussed in the context of PIXE in this work from (223).

Z	Symbol	$K_{\alpha 1}$	$K_{\alpha 2}$	$K_{\beta 1}$	$L_{\alpha 1}$	$L_{\alpha 2}$	$L_{\beta 1}$	$L_{\beta 2}$	$L_{\gamma 1}$	$M_{\alpha 1}$
3	Li	0.054								
4	Be	0.109								
8	O	0.525								
9	F	0.677								
11	Na	1.041	1.041	1.071						
12	Mg	1.254	1.254	1.302						
13	Al	1.487	1.486	1.557						
17	Cl	2.622	2.621	2.816						
19	K	3.314	3.311	3.590						
22	Ti	4.511	4.505	4.932	0.452	0.452	0.458			
24	Cr	5.415	5.406	5.947	0.573	0.573	0.583			
26	Fe	6.404	6.391	7.058	0.705	0.705	0.719			
28	Ni	7.478	7.461	8.265	0.852	0.852	0.869			
29	Cu	8.048	8.028	8.905	0.930	0.930	0.950			
82	Pb	74.969	72.804	84.936	10.552	10.450	12.614	12.623	14.764	2.346
83	Bi	77.108	74.815	87.343	10.839	10.731	13.024	12.980	15.248	2.423

8.5. Total x-ray count dependence on Fe foil stack thickness (calibration curve)

Figure 48 shows how little the total number of counts in each individual 5 s spectrum depends on the beam current. The current for the calibration curve measurements in Exp. 3 shown here is almost constant at ~1 μA, while the sum of all counts drops drastically as the Fe foil stack gets thicker. This change is primarily due to the differences in attenuation for Fe and Pb/Bi x-rays.

This also indicates that it is not straightforward to use the number of counts as a proxy for the proton fluence and thereby the dpa delivered to the sample. This approach is useful for samples that do not change during an irradiation, and it is more accurate than intermittent current measurements with the Faraday cup but is much more difficult to apply for a sample whose composition changes dramatically over time, as is the case with ICE III samples.

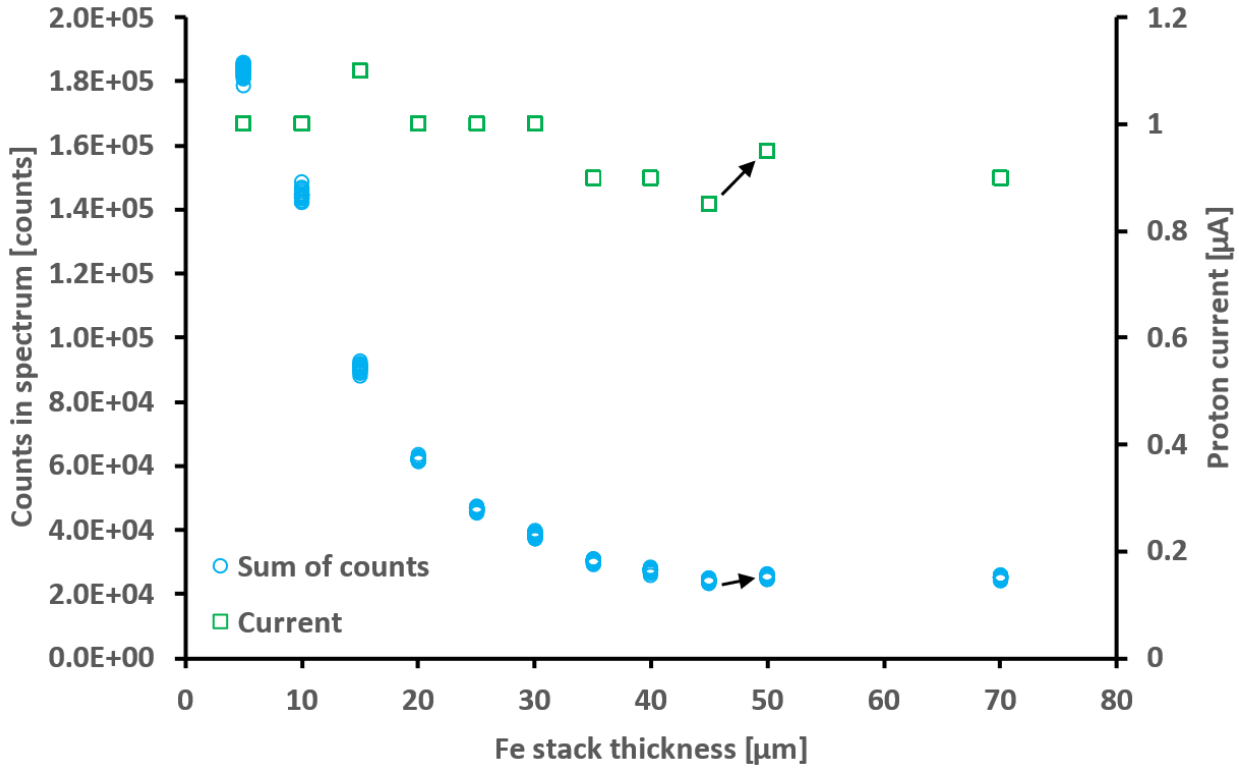

Figure 48 – Sum of all counts (blue circles) in individual spectra for the calibration curve in Exp. 3. Black arrows mark a visible slight increase in total counts due to a large increase in proton current (green squares).

8.6. Detector settings

Table 12 – All SDD settings (in order of appearance in .mca file) for various experiments described in this work.

Setting	Exp. 1	Exp. 2, 3	Salt tablet
Clock [MHz]	20	80	80
Peaking time [µs]	4	0.800	0.400
Fine gain	0.9305	1.02 – 1.03	0.9608
Total gain	33.000	14.9 – 15.0	13.999
Reset lockout [µs]	819	102	102
Flat top width [µs]		0.200	
Fast channel peaking time [ns]	400	800	400
Pile-up rejection		On	
RTD		Off	
MCA source		Norm	
MCA channels	1024	2048	2048
Spectrum offset		Off	
Analog input		Positive	
Input offset		Default	
Analog gain index	17	13	13
Non-trapezoidal shaping		0	
Peak detect mode		Norm	
Slow threshold [%]	1.562	2.502	8.996
LLD threshold		Off	
Fast threshold [channels]	31.62	27.00	15.00
DAC output		Shaped	
DAC offset		50	
RTD sensitivity		0	
RTD threshold		0.00	
BLR mode		1	
BLR down correction		3	
BLR up correction		0	
AUX_OUT selection		SCA8	
Preset time [s]	Off	5.0	Off
Preset real time		Off	
Preset counts		Off	
Preset counts low threshold		1	
Preset counts high threshold	8191	1023	8191
High voltage [V]		-135	
Temperature [K]	255	265	280
Pole-zero	Off	Off	Off
Preamp voltage [V]		5	
Scope trigger edge		FA	
Scope trigger position		12	
Digital scope gain		1	
MCS low threshold		1	
MCS high threshold		8191	

MCS timebase		0.01	
AUX output selection		ICR	
Test pulser		Off	
GP counter edge		RI	
GP counter input		AUX1	
GP counter uses MCA_EN		On	
GP counter uses GATE		On	
GP counter cleared with MCA counters		On	
MCA/MCS enable	On	Off	On
Speaker		Off	
Connector 1		DAC	
Connector 2		AUXIN2	

8.7. Count rate calculations for x-ray detector setup

8.7.1. X-ray source estimate: 4 MeV, 3 µA

An intended proton beam current of up to 3 µA measured in the end station Faraday cup corresponds to a proton flux ϕ_{H^+} of

$$\phi_{H^+} = 3 * 10^{-6} \frac{C}{s} * \frac{1\ H^+}{1.602 * 10^{-19} C} = \ 1.87 * 10^{13}\ \ H^+/s\ .$$

The Fe K x-ray production rate Y_K can be estimated as follows:

$$Y_K = \phi_{H^+} * N_{Fe} * \sigma_{Fe}(E) * \omega_{Fe,K}\ ,$$

with the areal number density of Fe atoms N_{Fe}, the ionization cross section σ_{Fe}, and the K-shell x-ray yield $\omega_{Fe,K}$. N_{Fe} can be calculated as

$$N_{Fe} = \frac{N_{Av} * \rho_{Fe} * t_{sample}}{M_{Fe}} = \ 4.25 * 10^{20}\ atoms/cm^2\ ,$$

where N_{Av} is the Avogadro number (6.022×10^{23} atoms/mol), ρ_{Fe} is the density (7.874 g/cm^3 at room temperature), t_{sample} is the thickness of the sample (50 µm), and M_{Fe} is the atomic mass of Fe (55.845 g/mol).

The proton-energy-dependent ionization cross section of Fe σ_{Fe} is 720.8 b for 4 MeV protons and the K-shell x-ray yield $\omega_{Fe,K}$ is 0.3546 (224). With this, Y_K is roughly 2.03×10^{12} x-rays per second for a 3 µA current of 4 MeV protons incident on pure Fe. Note that we do not consider two important factors in this rough estimate: 1) the energy loss of the protons as they travel through the sample, which would decrease the ionization cross section for the deeper parts of the sample, and 2) the attenuation of x-rays from deeper areas of the sample. Both factors mean that the number of x-rays produced is overestimated here.

8.7.2. Geometric efficiency

The number calculated above is the number of Fe K x-rays emitted in all directions. The detector has a 5x5 mm^2-sized area about 30 cm away from the sample surface, and therefore, the geometric efficiency ϵ_{geom} is approximately

$$\frac{0.25\ cm^2}{4\pi(30\ cm)^2} = 2.21 * 10^{-5}\ .$$

8.7.3. X-ray source estimate: 1.5 MeV, 3.3 µA

The same calculation as in the previous section, but for 3.3 µA of 1.5 MeV protons gives a proton current ϕ_{H^+} of

$$\phi_{H^+} = 3.3 * 10^{-6} \frac{C}{s} * \frac{1\ H^+}{1.602 * 10^{-19} C} = \ 2.06 * 10^{13}\ \ H^+/s\ ,$$

an areal number density N_{Fe} of

$$N_{Fe} = \frac{N_{Av} * \rho_{Fe} * t_{sample}}{M_{Fe}} = 1.02 * 10^{20}\ atoms/cm^2\ ,$$

due to the smaller proton range of 12 µm according to SRIM (170), and finally an x-ray yield Y_K of

$$Y_K = \phi_{H^+} * N_{Fe} * \sigma_{Fe}(E) * \omega_{Fe,K} = 9.56 * 10^{10}\ photons/s\ ,$$

with a σ_{Fe} of 128.3 b for 1.5 MeV protons and an $\omega_{Fe,K}$ of 0.3546 (224).

8.7.4. X-ray attenuation

The thickness of the added Al is determined by the desired reduction in current according to the Beer-Lambert law:

$$\frac{I}{I_0} = \exp\left(-\left(\frac{\mu}{\rho}\right) * \rho * t\right)\ ,$$

where I is the resulting and I_0 the original current, $\frac{\mu}{\rho}$ is the mass attenuation coefficient, ρ is the density, and t is the thickness of the absorber. Household Al foil is ~16 µm thick, so a stack of 15 foils is about 244 µm thick. The mass attenuation coefficient for 6 keV photons in Al is 115.3 cm^2/g (225) and the density of Al at room temperature is 2.7 g/cm^3. Therefore, 244 µm of Al would allow the transmission of only 5.69×10^{-4} of the original x-rays (ϵ_{Al}).

A similar calculation for the Be window on the detector shows that it has a very small impact on the x-ray attenuation. With a mass attenuation coefficient (at 6 keV) of 2.527 cm^2/g, a density of 1.85 g/cm^3 (at room temperature), and a thickness of 12 µm, it allows the transmission of 0.994 of all incoming x-rays (ϵ_{Be}).

8.8. Dead time dependence on count rate

Data acquisition in the DPP is paused when data is transferred, when the preamplifier resets, and when the GATE input is used and is off (186). Data transfer times vary and depend on the number of channels are used (between 113 microseconds to 2.5 ms for FPGA (field-programmable gate array) to microcontroller and between 2 to 20 ms for DPP to computer). The duration of the preamplifier reset is determined by the reset lockout parameter in the DPPMCA software. Therefore, the only variable during a long-term irradiation is the frequency of preamplifier resets, which depends on the number of input counts. This relationship is reflected in the relation between dead time and output counts (counts in spectrum), which is shown in Figure 49. The dead time is also directly dependent on proton beam current, as long as nothing changes in the detector (e.g., detector temperature) and the current does not increase so drastically that pile up becomes an issue.

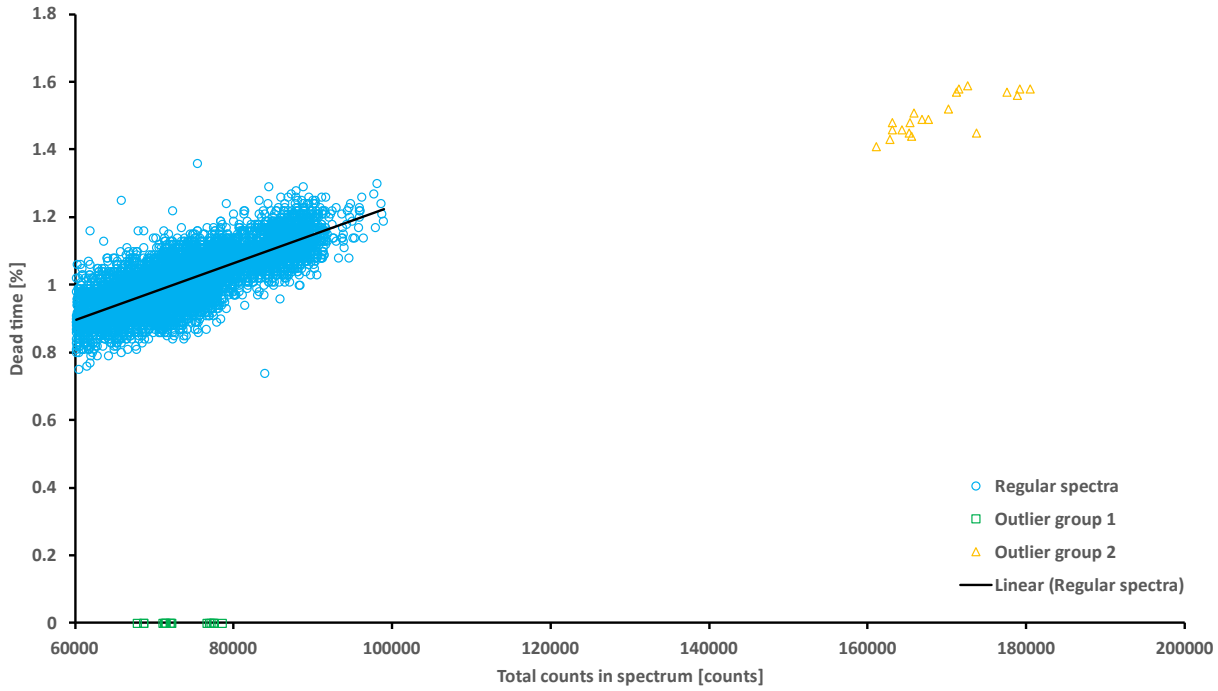

Figure 49 – Dead time vs. total number of counts in spectrum for Exp. 2. The dead time increases linearly with the output counts recorded in valid spectra (blue circles), i.e., those containing at least 60,000 counts, with few exceptions where no dead time was computed by the software (green squares) or where the total counts in the spectrum are unusually high (yellow triangles).